COMPARATIVE STUDY OF DILUTE NITRIDE AND BISMIDE SUB-JUNCTIONS FOR TANDEM SOLAR CELLS

Richard Matsatsi Ketlhwaafetse

A thesis submitted for the degree of Doctor of Philosophy (Ph.D.) in Applied Physics

School of Computer Science and Electronic Engineering

University of Essex

January 2016

Abstract

The theoretical models show that tandem solar cells can reach efficiency of more than 50 %. To achieve efficiencies closer to the projected outputs in a quad tandem solar cell, a 1.0 eV sub-junction with good optical and electrical properties is sought. The observed bandgap reduction when small amounts of Nitrogen or Bismuth is incorporated into GaAs makes these alloys (dilute nitrides and bismides) possible candidates for the tandem solar cells.

In this work, the performance of dilute nitride and bismide solar cells of different designs which include p-i-n bulk and p-i-n multiple quantum wells (MQWs), and n-i-p-i structures are studied comparatively. Performance in this context refers to: the magnitude and quality of the dark current generated by the devices, the spectral response of the solar cells especially in the dilute nitride and bismide absorption regions, and efficiency responsivity to temperature and to elevated radiation. To achieve the latter objectives, dark and under the AM1.5G and spectral response measurements were performed on the solar cells. The results reveal that, in the dilute bulk or MQWs p-i-n and n-i-p-i solar the total dark current is nearly the dark current generated by dilute nitride or bismide material alone. The applicability of Sah-Noyce-Shockley model to bulk p-i-n dilute nitride solar cells dark current is demonstrated. The dilute nitride solar cells exhibit temperature coefficients of efficiency that are lower than that of the conventional GaAs p-n junction solar cell. MQWs solar cells show lowest sensitivity to temperature changes.

The dilute nitride and bismide materials show similar diode characteristics with dark currents that are dominated by non-radiative recombination mechanisms.

Acknowledgements

Firstly my thanks go to God Almighty who gave me time to do the work, “It is not of him who wills nor of him who runs but of God who shows mercy”. I thank my supervisor Professor Naci Balkan for patiently guiding and supporting me throughout the project. I thank all the members of Essex University Optoelectronic research group who we battled it out together, especially Adrian Boland who helped me a lot in nanofabrication techniques.

I am so much thankful to all the members of Mountain of Fire and Miracles Cambridge (UK) and Goodnews Fire Ministries (Botswana) who continued praying with and for me throughout my study. My special thanks to Mrs F.T. Mokane in Training Department University of Botswana who always gave me words of encouragements. Lastly but not least, I thank my family members who encouraged me all the time. All those who supported me in one way or the other and I did not mention, greater is your reward and is with the Lord.

List of symbols

RT	Room Temperature
MQW s	Multiple Quantum Wells
VBM	Valence Band Maxima
CBM	Conduction Band Maxima
CBA	Conduction Band Anti Crossing
VBAC	Valence Band Anti Crossing
SCR	Space Charge Region
EHPs	Electron hole pairs
MBE	Molecular Beam Epitaxy
QE	Quantum Efficiency
SEM	Scanning Electron Microscope
XRD	X-Ray Diffraction
KIT	Kyoto Institute of Technology
TUT	Tempera University of Technology
PL	Photoluminescence
FF	Fill factor
HH	Heavy Hole
LH	Light Hole
AR	Anti-reflection coating
SI	Semi-insulating
ε_0	Permittivity of free space = 8.85 x 10^{-12} F/m
h	Planck's constant = 6.63 x 10^{34} m^2 kg/s
$\hbar$	Planck's constant/2π = 1.055 x 10^{34} m^2 kg/s
q	Electronic charge = 1.6 x 10^{-19} C

m_0	Electronic rest mass = 9.109x 10^{-31} kg
α	Absorption coefficient
α'	Fitting parameter in BAC model accounting for the nitrogen concentration effect on the conduction band
A	Area
AM	Air mass index
β_x	Photon flux density at depth x
C_{NM}	Fitting parameter in the BAC model to describe the interaction between the localised n-level and host semiconductor matrix
χ	Electron affinity
χ	Fitting parameter in the BAC model accounting for nitrogen concentration effect on the valence band
D_n	Diffusion coefficient of minority electrons
D_p	Diffusion coefficient of minority holes
E	Energy
E_a	Effective band gap of quantum well
E_c	Conduction band level
E_F	Fermi level
E_g	Band gap
E_M	GaInAs conduction band states
E_N	Localised acceptor level
E_V	Valence band level
E_w	Well material band gap
G_n	Minority electron generation rate
G_p	Minority hole generation rate

γ	Fitting parameter for Nitrogen effect on localised acceptor level E_N
η	Efficiency
J	Current density
J_{photo}	Photogenerated current density
J_{photod}	Photogenerated current density in the depletion region
J_{photoe}	Photogenerated current density in the emitter
J_{photob}	Photogenerated current density in the base
J_s	Reverse saturation current density
J_{sc}	Short circuit current density
J_0	Saturation current coefficient
k	Crystal wave vector
λ	Wavelength of radiation
L	Quantum well width
L_n	Minority electron diffusion length
L_p	Minority hole diffusion length
μ_n	Minority electron mobility
μ_p	Minority hole mobility
μ_h	Hall mobility
m_e^*	Electron effective mass in a crystal
m_h^*	Hole effective mass in a crystal
n/p	Carrier density
N_a	Acceptor concentration
N_d	Donor concentration
D_C	Conduction band density of states

D_V	Valence band density of states
n_i	Intrinsic carrier density
n_p	Photogenerated electrons in p-type material
n_{p0}	Equilibrium electron population in the p-type material.

Table of Contents

1 Introduction

1.1 The Solar Energy

The sun releases a vast amount of energy eqivalent to 1000 000 TW into the solar system [1]. The temperature at the surface of the sun is approximately 6000 K. At a point just outside the earth's atmosphere the solar flux is observed to be 1353 W/m^2. Almost all renewable energy sources with exception to radioactive and nuclear energy sources, derive their energy from the sun. Figure 1.1 shows the image of the sun from the Solar and Heliospheric Observatory (SOHO).

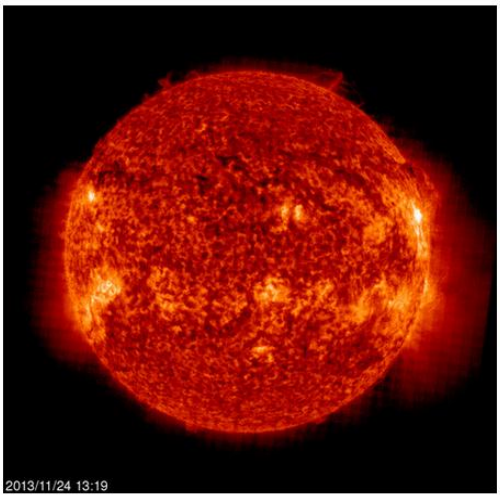

Figure 1.1: The image of the sun from SOHO [2]

Despite the vast amount of radiant energy from the sun, the fossil fuels and nuclear power which are depleting sources still remain the main sources of primary energy in the world at 78 % of the total energy demand. The renewable energy sources have a disproportionately low contribution of 22 % to the total world energy use. Photovoltaic still take a miniscule fraction of the renewable energy source equivalent to only 0.01 % of total world energy use [3]. With the projected world population of 12 billion by 2050, the energy consumption is

estimated to be 28 TW, which is double the current demand of 14 TW and the CO_2 emission is projected be more than twice the pre-historic level [1]. With current trend of energy consumption, in less than 350 years all the depleting sources will run out.

Photovoltaic has a great potential to become the most potent energy source for the future generation. Besides being virtually inexhaustible like all renewable energy, it does not have any combustible by-products sources and its CO_2 'footprints' is very low. The only CO_2 emission is during the manufacture, and is still between 5-13 % [4] of the contribution by the fossil fuels. However, there are still challenges facing photovoltaic, the major ones being the low efficiency and high installation costs. There are two ways of curbing the above problems. One alternative is to reduce the cost of production by going for relatively cheaper materials like amorphous, polycrystalline and thin films at the expense of efficiency, or going for higher efficiency at the expense of material cost. This thesis focuses on the latter by focusing on the increase of efficiency by use of novel III-V material systems and designs.

To date most of the record efficiency cells has been tandem solar cell designs based around GaAs. $Ga_{0.44}In_{0.56}P$/GaAs/Ge cells have reached efficiencies of 40.1% for the AM1.5D spectrum concentrated to 240 suns [5]. The addition of Indium to the GaAs increases the efficiency of the $Ga_{0.44}In_{0.56}P$/GaAs/Ge solar cell and an efficiency of 40.7 % has been achieved with $Ga_{0.44}In_{0.56}P/Ga_{0.92}In_{0.08}As$/Ge solar cells [6]. Further improvement of efficiency of $Ga_{0.44}In_{0.56}P/Ga_{0.92}In_{0.08}As$/Ge cells is limited by the amount of Indium that can be added, due to its effect of increasing lattice constant. The addition of small amounts of nitrogen to GaAs causes a large reduction in band gap which can be modelled using the band anti-crossing approach [7]. The addition of nitrogen also reduces the lattice constant of the alloy. This effect combined with the addition of Indium allow both the band gap and lattice constant of the quaternary $Ga_{1-x}In_xN_yAs_{1-y}$ to be chosen independently of one and other [8]. In 1998 the National Renewable Energy Laboratory (NREL) suggested that Ga$InP/$

$GaAs/Ge$ tandem solar cells could be made more efficient by adding another junction with a band gap of 1eV between the GaAs and Ge junctions. A logical choice for this junction appears to be the compound $Ga_{0.97}In_{0.03}N_{0.02}As_{0.98}$ as it has a band gap of 1eV and is also lattice matched to GaAs [9]. However the addition of nitrogen to GaAs causes dislocations and imperfections which reduce the minority carrier mobility and lifetime.

1.2 Thesis Objectives

Multi-junction solar cells, in particular tandem solar cells with projected efficiencies of more than 50 % are potential candidates for '4^{th} generation photovoltaic devices'. In order to achieve such projected efficiencies a near 1.0 eV sub-junction with good optical and electrical properties is sought. The observed unexpected band-gap reduction when small amount of Nitrogen or Bismuth is incorporated into GaAs makes these alloys (dilute nitrides and bismides) possible candidates for 1.0 eV sub junction in tandem solar cells. The aim of this project is to study the performance of dilute nitride and bismide solar cells designed for the fourth tandem solar cell sub-junction (1.0 eV junction). The minority carrier lifetimes observed in dilute nitrides and bismides, are often less than 1 ns [10 and 11], which is 500 times less than typical GaAs minority carrier lifetime [12]. The short minority carrier lifetimes result in very short diffusion lengths that make it a challenge to design the dilute nitride and bismide solar cells with conventional design that works well for the GaAs solar cells. Therefore a number of non-conventional designs which include; the p-i-n bulk, p-i-n MQWs and n-i-p-i, are commonly used for dilute nitride and bismide solar cells.

The first objective of this project is to study and compare the performance of different designs used. The second objective is to probe any material related effects on performance between dilute bismides and dilute nitrides. Some of the parameters that are used to compare the performance of the device studied include; magnitude and quality of the dark current generated, temperature coefficient of efficiency, open circuit voltage, short circuit current density, average recombination lifetimes and response to radiation intensity.

1.3 Thesis outline

Chapter 2 is literature review on the key topics that this work will be based on. The solar spectrum and the concept of Air Mass Index are briefly described. A recap of the band energy model for solids, Fermi Dirac statistic and the formation of p-n junction is given. Solar cell is introduced as a p-n junction and its key performance parameters are discussed. Optical and electrical processes with emphasis on absorption coefficient and minority carrier transport are discussed. Efficiency limits of single junction and the concept of multi-junction are briefly discussed.

The physics of dilute nitrides and bismides is introduced with emphasis on the band-gap determination in the alloys using the Conduction Band Anti Crossing Model (CBAC) and Valence Band Anti Crossing Model (VBAC) respectively. Various designs commonly used in materials with short minority carrier lifetimes like dilute nitrides and bismides and their limitations are discussed. Lastly a road map of 1.0 eV junction for tandem solar cells up to its present status is briefly presented.

Chapter 3 is a summary of the experimental and theoretical techniques deployed in this work. Growth techniques of the alloys studied in this work with emphasis on Molecular Beam Epitaxy (MBE) which was the major growth technique for most of the devices as well as description of experimental set ups and apparatus are presented. The experimental techniques described include dark, light I-V characterisation, spectral response of short circuit current, photoluminescence, steady state and transient photoconductivity.

Chapter 4 is the discussion of the results of dilutes nitride solar cells of various designs. The structures of the solar cells are presented. Room and low temperature dark and AM1.5G J-V characterisation results are discussed under each design. The temperature coefficients of the efficiency devices are deduced from the normalised maximum power against voltage plots.

The average recombination lifetimes are deduced from the Sah-Noyce-Shockley and Shockley diode models. The performance of the solar cell at varying irradiance levels is discussed with emphasis on maximum power (or efficiency) and Fill Factor against applied voltage. The trapping effects of each design are deduced from the slopes of the hyperbolic logarithmic plots of dark current density versus inverse of temperature.

Chapter 5 is the results of photoconductivity measurements on bulk $GaAs_{1-x}Bi_x$ layers followed by the results of valence band anti-crossing model (VBAC) model for calculating the $GaAs_{1-x}Bi_x$ alloy compositions that would give suitable band gaps for tandem solar cells. The last section of the chapter is characterisation of $GaAs_{1-x}Bi_x$ p-i-n solar cell.

Chapter 6 is the summary of the work as well as future work and recommendations.

References

[1] W. Walukiewicz, "*Adavanced concepts and materials for efficient solar energy conversion"*, presentation at CLEO: Applications and Technology, Baltimore, (2011).

[2] Christina Honsberg. 2013. *PVEducation*. [ONLINE] Available at: http://pveducation.org/pvcdrom/properties-of-sunlight/the-sun. [Accessed on 01 July 2014].

[3] M. Zeman, "**Introduction to photovoltaic Solar Energy**", Solar Cells, collegematerial, (2003), http://aerostudents.com/files/solarCells/solarCellsTheoryFullVersion.pdf

[4] H. Mackel; "**Capturing the spectra of Solar Cells**", PhD. Thesis, Australian National University, (2004).

[5] M. A. Green et al., *"Progress in Photovoltaics", Research and Applications*, Vol. 16, Issue 5, pp. 435-440, (2008).

[6] R.R. King, C.C. Law, K.M. Edmondson, C.M. Fetzer, G.S. Kinsey, H. Yoon, R.A. Sherif and N.H. Karam, **"***40% efficient metamorphic GaInP/GaInAs/Ge Multi-junction Solar Cells*", Journal of Applied Physics, Vol. 90, pp. 183516-183516, Issue 18, (2007).

[7] A. Lindsay and E.P. O'Reilly, "*Theory of enhanced band-gap non-parabolicity in GaNAs and related alloys"*, Solid State Commun., Vol. 112, Issue 8, pp. 443-447 (1999).

[8] M. Kondow, T. Kitatani, S. Nakatsuka, M. Larson, K. Nakahara, Y. Yazawa, and M. Okai, **"***GaInNAs: A novel material for long wavelength semiconductor lasers,*" IEEE Journal of Selected Topics in Quantum Electronics, Vol. 3, pp. 719, (1997).

[9] D. J. Friedman, J.F. Geisz, S.R. Kurtz, J.M. Olson, **"***1-eV solar cells with GaInNAs active layer*", Journal of Crystal Growth, Vol. 195, Issue: 1-4 pp.: 409-415, (1998).

[10] J. F. Geisz and D. J. Friedman, "*111-N-V semiconductors for solar photovoltaic applications*", Semiconductor Sci. Technol., Vol. 17, No. 8, (2002).

[11] S. Mazzucato, B Royall, R Ketlhwaafetse, N Balkan, J Salmi, M Guina, A Smith and R Gwilliam, **"***Dilute nitride and GaAs n-i-p-i solar cells***,"** Nanoscale research letters, Vol. 7, No. 1, pp. 1-5, (2012).

[12] A.J Ptak et al., **"***Defects in GaInNAs: What we've Learned so Far"***,** Presented at the National Centre for Photovoltaics and Solar Program Review Meeting, (2003).

2 Background

2.1 The Solar Spectrum

The spectrum of the sun can be modelled by that of a black body at temperature of 6000 K. The spectrum of a black body at temperature (T) is given by

$$I(v,T) = \frac{2hv^3}{3C^2}\frac{1}{e^{\frac{hv}{k_B T}-1}} \tag{2.1}$$

where h is Planck's constant, v is the frequency of the photons, c is the speed of light, k_B is Boltzmann's constant and T is the temperature of the black body.

The spectrum of the sun at the surface of the earth (terrestrial) is different from the one measured outside the earth's atmosphere (extra-terrestrial), due to attenuation, absorption and scattering as the radiation passes through the atmosphere. The different spectra at the earth surface further differ depending on the path the sun rays take through the atmosphere to reach the earth surface. The ratio between the lengths of the path of the light through the atmosphere to the shortest distance through the atmosphere (the normal to the earth's surface) as shown in figure 2.1 is known as the Air Mass (AM) index, as shown in equation 2.2.

$$AM = \frac{1}{\cos(\theta)} \tag{2.2}$$

where θ is the angle of the sun measured from the normal to the earth surface.

The AM0, AM1.5G, and AM1.5D spectrums are defined by American Society for Testing and Materials. The AM0 is the spectrum measured just outside the earth's atmosphere and has an irradiance of 1353 W/m^2. The AM1.5 spectrum is measured

at the earth surface for radiation incident at 48.2 ° from the zenith, and at this angle the atmosphere should attenuate the radiant power to about 900 W/m^2. For convenience

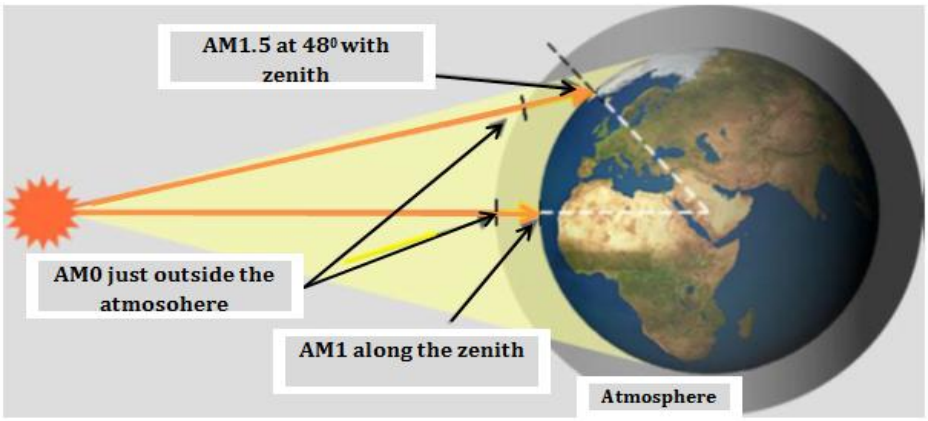

Figure 2.1: The diagram of the earth showing respective air mass index concept.

the standard terrestrial spectrum (AM1.5) is normalised so that the integrated irradiance is 1000 W/m^2. The AM1.5 is further classed as AM1.5 G or AM1.5 D, in which the suffix G and D means global and direct respectively. The AM1.5 G spectrum is the one in which both the direct radiation that reaches the earth surface as well as the scattered radiation are considered. The AM1.5 D spectrum only considers the direct radiation that reaches the earth surface without being scattered.

The atmospheric effects on the spectrum are evident, as shown in figure 2.2. Water, oxygen and carbon dioxide cause absorption that is wavelength selective, and these result the in the gaps observed in the spectrum reaching the surface of the earth. Photons with wavelength near 900, 1100, and 1400 nm are absorbed by water vapour in the atmosphere. Ozone absorbs radiation with wavelength below 300 nm; this reduces the amount of ultraviolet that reaches the earth surface.

When designing and or testing solar cell devices it is important to consider the spectrum under which it operates. This not only does help for comparison purposes but helps in optimising the design to get maximum efficiency and devices that can tolerate the conditions under which they operate.

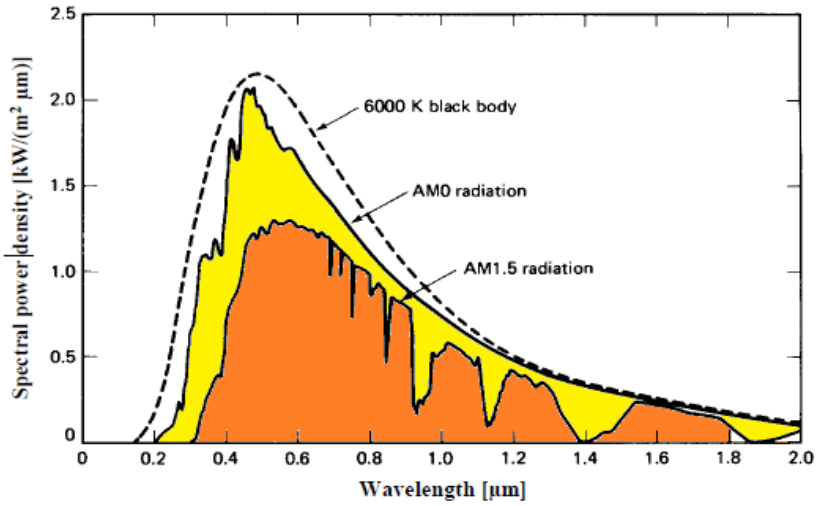

Figure 2.2: Spectral irradiance of a blackbody at 6000 K, AM0 and AM1.5 spectra.

2.2 Introduction to semiconductors

When a solid forms, the discrete energy levels of the atoms or molecules tends to form clusters of energy states (energy bands). The shape of energy bands and the space between them differ depending on the lattice structure and composition of the solid. The space between the upper, nearly empty band (conduction band) and the lower, nearly full band (valence band), is the principal energy gap or simply band gap (E_g) of the material. The bandgap determines the electrical properties of the solid. Solids classified as metals have their conduction band overlapping with the valence band and there are plenty of free carriers for conduction even at room temperature. Insulators have wide band gap and huge amounts of energy would be required to promote electrons into the conduction band. However, semiconductors have a moderate band-gap of approximately 0.24 eV-6.2 eV [1]. In semiconductors at 0 K the conduction band is completely empty and the valence band completely filled up and at T > 0 a finite number of electrons occupy the conduction band due to thermal excitation.

Details of energy band structures can be shown by energy (*E*) versus crystal momentum (*k*) resulting in what is popularly known as (*E-k* diagrams). Simplified *E-k* diagram for a direct band gap material and indirect band gap materials are shown in figure 2.3. Band structures of dilute nitride and bismides shall be re-visited in more details in chapter 5, under the Band Anti Crossing (BAC) model.

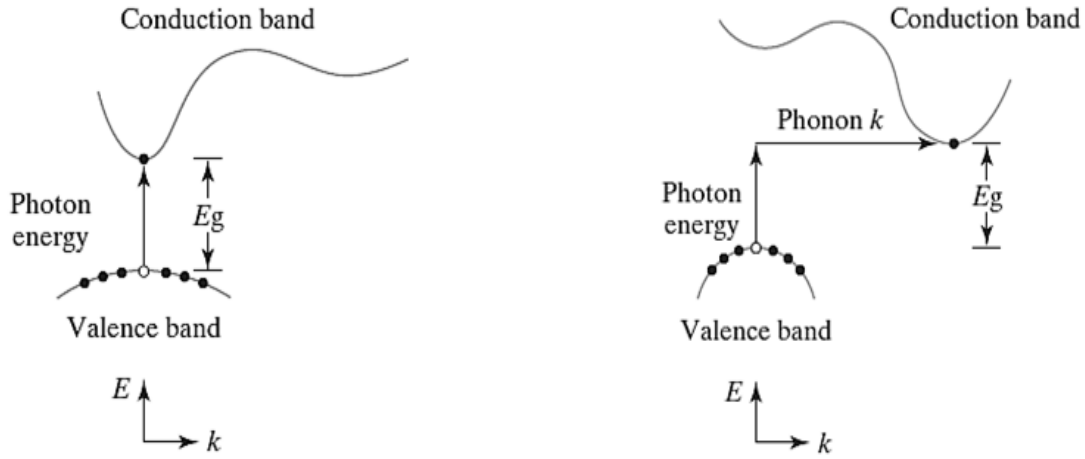

Figure 2.3: E-k diagrams for: (a) direct band-gap and (b) indirect band-gap materials [2].

The occupancy of the conduction is governed by the Fermi-Dirac probability function given by equation 2.3,

$$F(E) = \frac{1}{1+\exp\left(\frac{E-E_f}{kT}\right)} \tag{2.3}$$

where k is the Boltzmann constant and T is the absolute temperature and E is the Fermi energy level. $F(E)$ describes the probability of electrons in the conduction band and similarly $1 - F(E)$ describes the probability of holes in the valence band. The density of such states in the conduction band is given by

$$D_c(E) = \frac{M_C}{\pi^2}\frac{\sqrt{2}(m_e^*)^{2/3}(E-E_C)^{1/2}}{\hbar^3},\ E \geq E_c \tag{2.4}$$

where M_C is the number of equivalent minima in the conduction band, m_e^* is the density of state effective mass for the conduction band and $\hbar$ is Planck's constant.

A similar expression can be written for the density of states in the valence band. The product of density of states $D_c(E)$ and the probability of occupancy $F(E)$ gives the carrier distribution in the conduction band and a similarly that of $D_v(E)$ and $1-F(E)$ for the valence band, Figure (2.4).

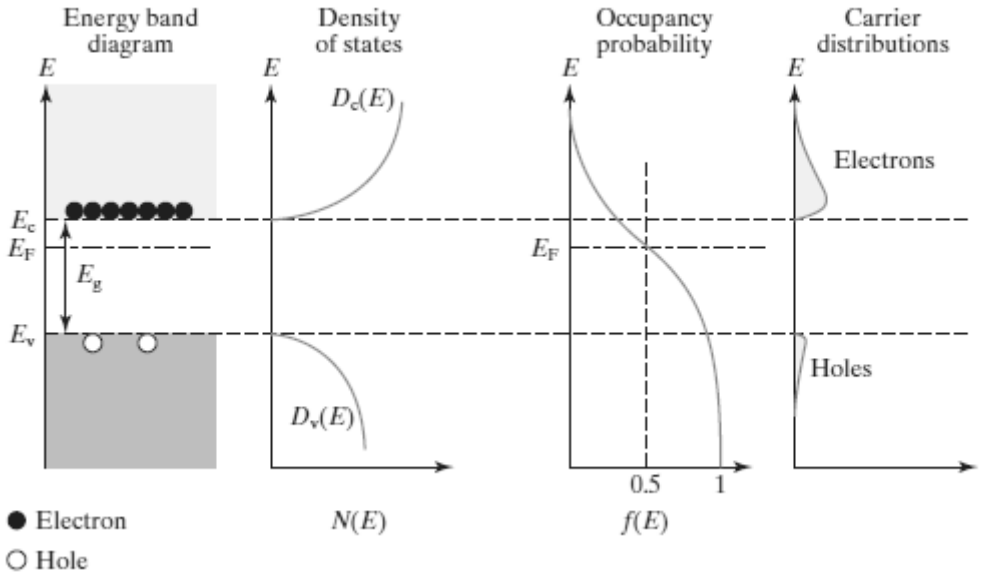

Figure 2.4: Schematic energy band diagram, density of states, Fermi-Dirac distribution, and carrier distribution versus energy in an n-type semiconductor [2].

The effective densities of states in the conduction and valence band are given by;

$$D_c = 2\left(\frac{2\pi m_e^* kT}{h^2}\right)^{3/2} \text{ and } D_v = 2\left(\frac{2\pi m_h^* kT}{h^2}\right)^{3/2} \tag{2.5}$$

where m_e^* and m_h^* are the density of state effective masses for the conduction and valence band respectively.

2.3 Formation of the PN junction

When an n-type and p-type materials are brought together (through various growth processes), carriers diffuse across the junction leaving behind a layer of fixed charge (SCR), on either side of the junction. On the n side the SCR is positive due to the ionised donors and on the p side the SCR is negative due to the ionised acceptors, this result in an electrostatic field which opposes further diffusion. Equilibrium is established when the diffusion of majority carriers across the junction is balanced by the drift of minority carriers back to their majority side of the junction [3]. The Fermi levels needs to be continuous throughout the structure and as a result there is bending of the energy band profile of the p-n junction, figure 2.5.

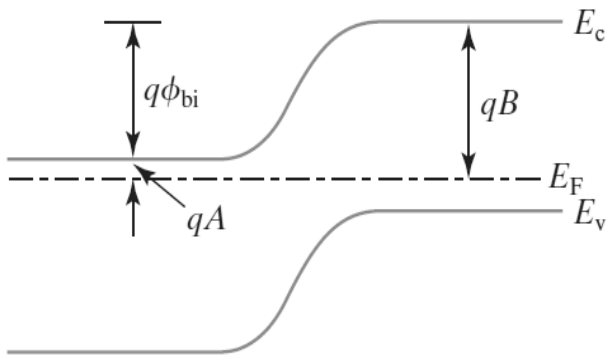

Figure 2.5: Band profile of a p-n junction.

The contact voltage ($V_{bi} = q\phi_{bi}$) established is given by

$$q\phi_{bi} = qB - qA \tag{2.6}$$

where (qA) is the difference between the Fermi energy level and conduction band edge on the n side and (qB) is the difference between the Fermi energy level and the conduction band edge on the p side (fig. 2.5). The contact voltage is commonly

determined from the doping concentrations on the n and p side of the junction using the relation

$$V_{bi}=\frac{kT}{q} ln\left(\frac{N_a N_d}{n_i^2}\right) \tag{2.7}$$

where n_i , N_d and N_a are the intrinsic carrier, donor and acceptor concentration respectively.

The thickness of the SCR that forms is determined from Poisson's equation given by

$$W_d = \sqrt{\frac{2\varepsilon_s V_{bi}}{q}\left(\frac{1}{N_a}-\frac{1}{N_d}\right)} \tag{2.8}$$

where ε_s and V_{bi} are the semiconductor permittivity and the built-in potential respectively.

2.4 Solar cell I-V characteristics

2.4.1 Dark I-V characteristics

The dark current consists of the diffusion current from the base and emitter regions and the generation-recombination current in the space-charge-region (SCR). In an ideal diode the SCR component of the dark current is negligible and the total dark current density can fit into the ideal Shockley diode equations 2.9 and 2.10.

$$J = J_0\left(\exp\left(\frac{qV}{kT}\right)-1\right) \tag{2.9}$$

where

$$J_0 = \left[q\frac{D_n n_i^2}{L_n N_a} + q\frac{D_p n_i^2}{L_p N_d}\right] \tag{2.10}$$

and L_n , L_p, D_n, D_p, N_a, N_d and n_i, electron diffusion length, hole diffusion length, electron diffusion coefficient, hole diffusion coefficient, acceptor concentration, donor and intrinsic carrier concentration respectively.

This is not always the case as the SCR generation-recombination current may be comparable or even dominate the diffusion current. This can happen when the material out of which the junction has been grown has high density of defects, typical of dilute nitrides and bismides. The second factor is the design used, especially the enhanced depletion layers like in the p-i-n design often used for material with short minority carriers like dilute nitrides and bismides. In that case a two or more diodes are used to model the behaviour of the dark current. The two diode model shown in (2.11) is often used.

$$J = J_{01}\left(\exp\left(\frac{qV}{kT}\right) - 1\right) + J_{02}\left(\exp\left(\frac{qV}{2kT}\right) - 1\right) \tag{2.11}$$

where $J_{01}$is the diode saturation current density that results from the thermal generation of minority carriers in the base and emitter regions and J_{02} is the junction leakage current density which represents the carrier generation-recombination in the space charge region.
In the case of dominant trap that lies at energy E_t from the conduction band the SCR generation-recombination current can be estimated using the classic Sah-Noyce-Shockley Shockley model given by

$$J_{rg} = \frac{qn_iW_d}{\sqrt{\tau_{n0}\tau_{p0}}}\frac{2\sinh(qV/2kT)}{q\,(V_{bi} - V)/kT}f(b) \tag{2.12}$$

where

$$b = \exp\left(-\frac{eV}{2kT}\right)\cosh[(E_t - E_i)/kT + \frac{1}{2}\ln(\tau_{no}\tau_{p0})] \tag{2.13}$$

and $n_i, W_d, \tau_{n0}, \tau_{p0}, V_{bi}, E_t,$ and E_i are intrinsic carrier density, depletion width thickness, electron capture lifetime, hole capture lifetime, built in voltage, trap energy level and intrinsic Fermi level respectively.

A simplified and generalised expression of the dark current which permits variable ideality factor as shown in equation 2.14 is useful in dark current analysis.

$$J = J_{0,effective}\left(\exp\left(\frac{qV}{mkT}\right) - 1\right) \tag{2.14}$$

where $J_{0,effective}$ the effective reverse saturation current and (*m)* is a variable ideality factor. The ideality factor *(m)*, reveals the nature of dominant recombination in the device, typically 1 for diffusion current and >1 for SCR recombination current. Dark currents are important as they place a limit on the maximum output voltage a cell can produce under specified illumination as shown in the expression in equation 2.15.

$$V_{oc} = \frac{kT}{q} ln\left(\frac{J_{sc}}{J_0} + 1\right) \tag{2.15}$$

2.4.2 Light I-V characteristics

The current in an ideal illuminated photovoltaic cell can be modelled by the superposition principle (equation (2.16)) of the dark currents and the photo generated current, fairly accurately for many photovoltaic materials, with the assumption that the dark current under the illumination condition will not differ from its dark condition value [3].

$$J = J_{sc} - J_o\left(e^{\frac{qV}{kT}} - 1\right) \tag{2.16}$$

where the first term (J_{sc}) is the short circuit current density (which is a total of the dark current and the photogenerated current), and the second term ($J_o\left(e^{\frac{qV}{kT}} - 1\right)$) is the dark current density.

The circuit model for a p-n junction solar cell is current source in parallel with diode, as shown in figure 2.6.

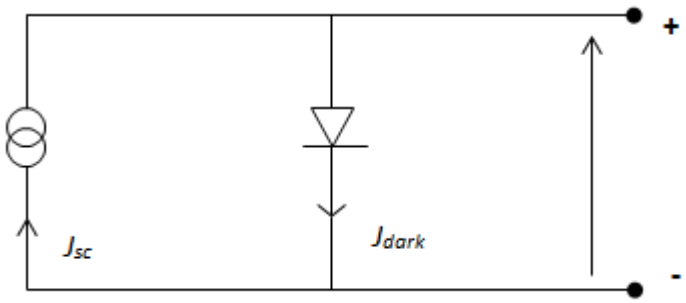

Figure 2.6: The circuit model for a p-n junction solar cell

In reality the p-n junction solar cell departs from the model described in previous section due to the internal resistance of the device. A more refined representation model include these parasitic resistance as a series and parallel resistances to the ideal circuit model as shown in figure 2.7.

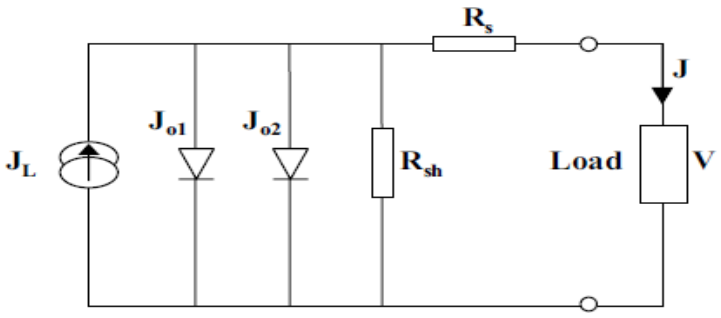

Figure 2.7: An equivalent circuit of a p-n junction solar cell

From figure 2.7 circuit diagram the two diode model equation will be;

$$J = J_L - J_{01}\left[exp\frac{q(V+JR_s)}{kT} - 1\right] + J_{02}\left[exp\frac{q(V+JR_s)}{n_2kT} - 1\right] - \frac{(V+JR_s)}{R_{sh}}, \qquad (2.17)$$

where $J_L, R_s \; and \; R_{sh}$ are the photogenerated current densities, series and shunt resistance respectively.

The key performance parameters of a solar cell include the short circuit current density, J_{sc}, the open voltage V_{oc}, the fill factor FF, from which the efficiency η of the cell is determined.

The theoretical maximum efficiency of a solar cell is the power density delivered at operating point as a fraction of the incident light power density, P_S.

$$\eta = \frac{J_m \ V_m}{P_s} \tag{2.18}$$

where J_m and V_m are the points at maximum power delivered by the cell. In practice the maximum short circuit current and maximum voltage are reduced by the parasitic resistances of the cell and the recombination of carriers. The parasitic resistance are the series resistance (R_s) path of carriers to the external circuit and the parallel resistance (R_p) path offered by the cell.

The practical efficiency measured from the J-V plots is thus given by

$$\eta = \frac{J_m \ V_m FF}{P_s} \tag{2.19}$$

where *FF* is the fill factor. The J-V characteristics of a solar cell under illumination are shown in figure 2.8.

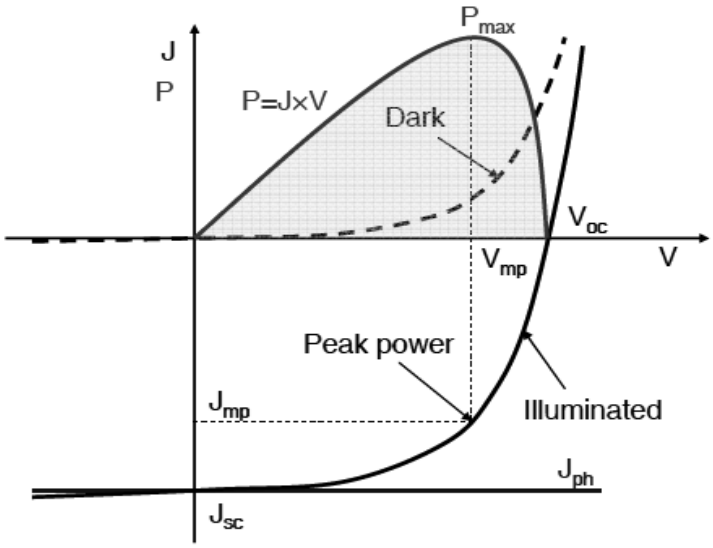

Figure 2.8: The IV characteristics of a solar cell under illumination [4].

2.5 Photovoltaic principle

In a doped semiconductor material the majority carrier far outnumbers the minority carriers and the effects of the latter are often negligible. However it is the dynamics of minority carriers that determines the operation of devices such as photodiodes (photo detectors) and solar cells. Minority carriers generated on any part of the p-n junction device usually remain for a short time (minority carrier lifetime) before recombining with majority carriers. In a solar cell minority carriers needs to be quickly separated before recombining. In fact the ability of the p-n junction space charge region to drift the minority electrons into the n- region and the holes into the p region, contrary to the diffusion gradient, is what underlies the principle of photovoltaics.

A p-n junctions designed to be specifically photosensitive are called photodiodes [5]. Usually they are constructed such that they have thin emitter region, mostly transparent to incident light and wider depletion region as an active region for the device. Photodiodes can operate in a photoconductive region or photovoltaic region (figure 2.9). A solar cell is a special type of

photodiode, operated in the photovoltaic region, with a maximised photo-voltage often by making the junction area very wide for absorbing more incident photons.

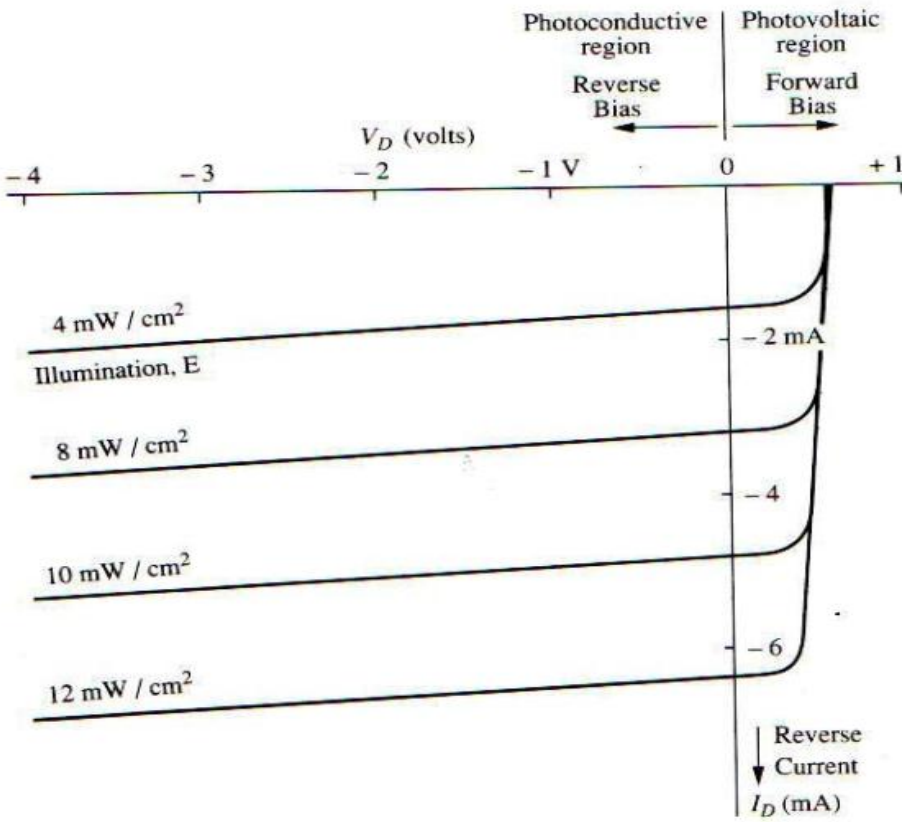

Figure 2.9 Photodiode I-V characteristics [5].

A solar operates by absorbing incident photons (formation of excitons), in the process generating hole-electron pairs (excitons separation) and subsequently collection of carriers to the external contacts (minority carrier transport). The efficiency of any solar cell devices is based on the efficiency of the latter processes [6]. Incidentally, the key properties for any semiconductor material for making solar cells are the absorption coefficient of the material which determines the spatial generation of minority carriers in the material, the recombination process which determines solar cell performance parameters to be discussed in following sections, and the minority carrier lifetimes, which directly affects key parameters

such as diffusion length and ultimately minority carrier collection from the device. These parameters shall be introduced in the following sections and later used in chapter five in modelling of short circuit current in p-n junctions.

2.5.1 Optical absorption

Optical excitation is the principal generation processes of minority carriers in solar cells. A semiconductor will absorb a photon of energy (hv) greater or equal to the band-gap (E_g) for direct bandgap materials. The photons with $hv < E_g$ are transmitted through without absorption. Figure 2.10 shows a typical absorption coefficient as a function of photon energy for GaAs material. The absorption coefficient spectrum shows three regions of absorption. At energies well below the bandgap absorption is dominated by free carrier absorption [7]. Free carrier absorption occurs particularly in highly doped semiconductors, and it is directly proportional to free carrier concentration. [7]. At energies near the bandgap the absorption coefficient increases exponentially. The exponential absorption is a manifestation of the effect of structural and thermal disorder on the electronic properties of semiconductors [8]. In this region, referred to as the Urbach region, the absorption is described by the relation (2.20).

$$\alpha(hv) = a_0 \left(\frac{hv - E_g}{E_0} \right) \tag{2.20}$$

where $\alpha(hv)$ is the absorption coefficient as a function of photon energy hv, a_0 is a constant, and E_0 is the characteristic energy of Urbach edge (Urbach parameter).

The absorption coefficient $\alpha(hv)$ for photons with energy (hv) greater than the band-gap (E_g), the absorption coefficient (for direct bandgap materials like GaAs) can be described by parabolic approximation given by;

$$\alpha(hv) = a_0\left(hv - E_g\right)^{1/2} \tag{2.21}$$

In addition the total amount of absorbed light depends on the thickness of the material used. How much material is needed depends on the absorption coefficient (α) of the material. The absorption coefficient is the inverse penetration depth measured in cm^{-1}.

Equation 2.27, describes the amount of light absorbed in a layer of a semiconductor.

$$I(x) = I_0(1 - \exp(\alpha x)) \tag{2.22}$$

where $I(x)$ is light intensity as a function of depth x and I_0 is the initial intensity.

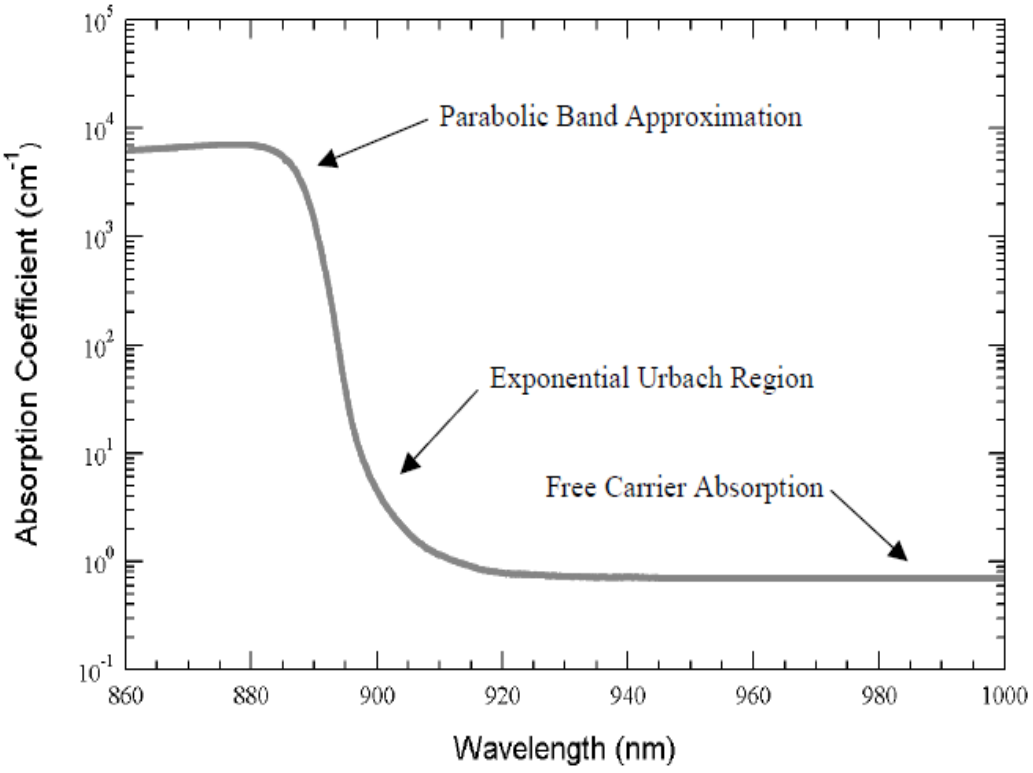

Figure 2.10: Optical absorption spectrum of GaAs [9]

The generation of photons is described by a similar equation to the optical absorption equation (2.22), with the assumption that one photon generates one EHP, taking into account the loss due to reflection (R) as shown in equation (2.33).

$$G(E) = \alpha(E)\beta_o(E)\big(1 - R(E)\big)e^{(-\alpha(E)x)} \tag{2.23}$$

where $G(E)$ is generation rate, β_o and E are the photo-flux density and energy of the photons absorbed at x respectively.

The amount of light absorbed by a slab of GaAs is shown in figure 2.11. This shows that just 3 μm of GaAs (direct-band gap material) absorbs nearly all the incident light with more than 50% absorbed within the 1st micrometre. On the other hand Si (an indirect band-gap material) will need more thickness for absorbing the same amount of light; as a result GaAs solar cells are thinner and lighter compared to Si solar cells.

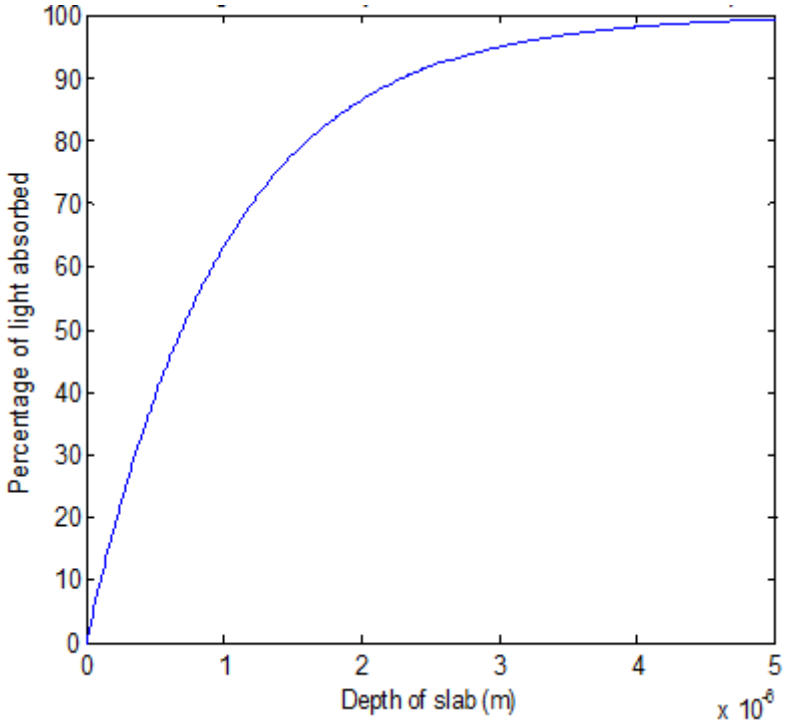

Figure 2.11: Amount of light absorbed by a slab of GaAs as a function of depth.

To minimise reflection losses, the surface is often coated with anti-reflection coating or various techniques such a surface texturing are used. The absorption coefficients of some common materials are shown in figure 2.12. The difference between the direct band-gap materials (InP, GaAs, GaN) from the indirect band-gap materials (Ge, Si) is the sharp rise (virtually vertical line) at band-gap edge of the direct bandgap materials as opposed to some degree of sloping at the absorption edge of the indirect band-gap materials.

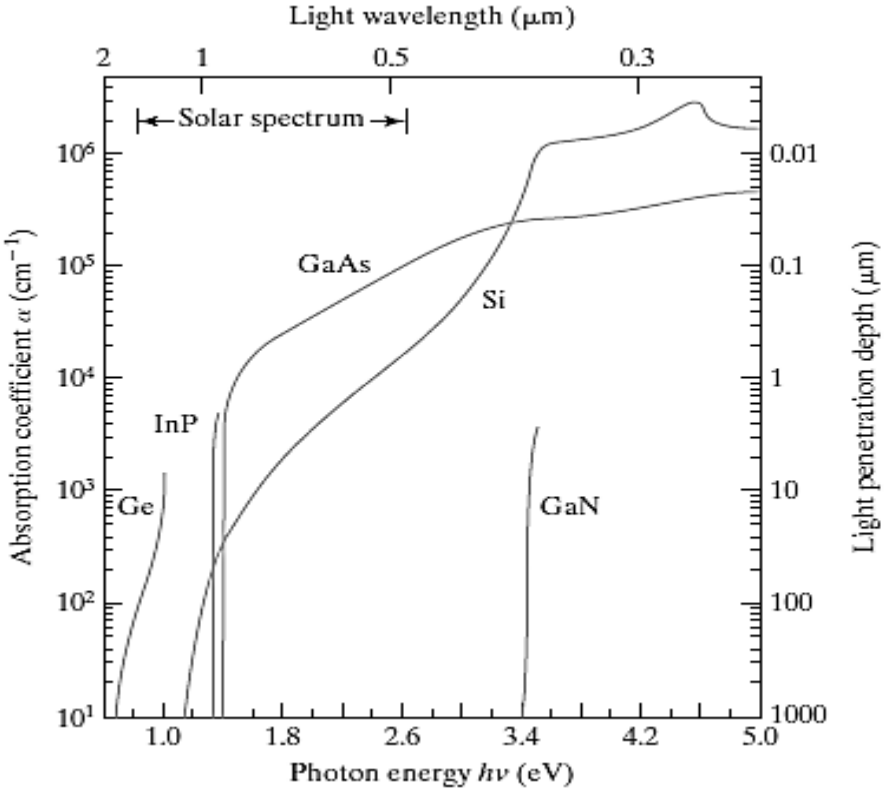

Figure 2.12: Absorption coefficients of common III-V semiconductors for different photon energies [2].

2.5.2 Recombination processes

The minority carries generated anywhere in a solar cell device are either collected to the external circuit or recombine in the device. Recombination can be; directly across the band gap (Radiative), assisted by energy transfer between carriers (Auger), or occur at the surface

or grain boundary (Surface recombination), depending on the condition of the semiconductor material used. Figure 2.13, shows major recombination processes in a semiconductor.

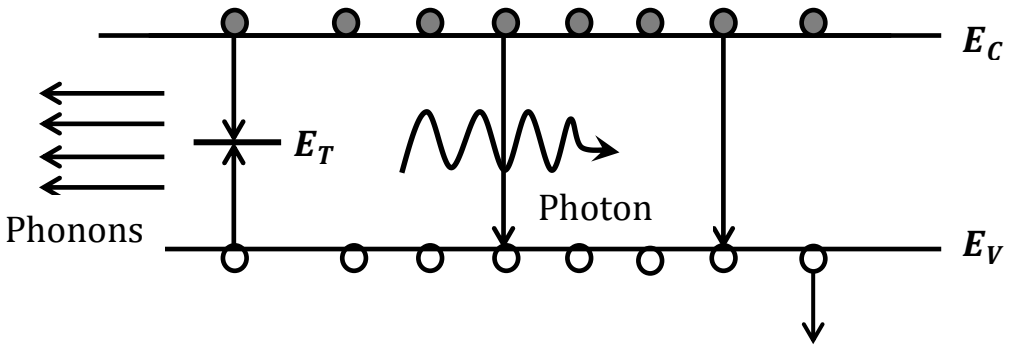

Figure 2.13: Recombination processes in a semiconductor

The net carrier recombination lifetime in the bulk (τ_b) materials can be expressed as

$$\frac{1}{\tau_b} = \frac{1}{\tau_{rad}} + \frac{1}{\tau_{Auger}} + \frac{1}{\tau_{SRH}} \tag{2.24}$$

where τ_{rad}, τ_{Auger} and τ_{SRH} are the radiative, Auger and Shockely Read Hall recombination lifetimes respectively. In defect related recombination carriers are trapped in deep states (recombination centres) and annihilate, subsequently releasing phonons into the lattice and the process is commonly modelled by the Shockley, Read and Hall (SRH) model. The SRH generation-recombination lifetime (τ_{SRH}) is described by (equation 2.25),

$$\tau_{SRH} = \frac{\tau_p(n_0+n_1+\Delta n)+\tau_n(p_0+p_1+\Delta p)}{p_0+n_0+\Delta n}, \tag{2.25}$$

where $\tau_p, \tau_n, n_0, p_0, n_1, p_1, \Delta n$ and Δp are the hole recombination lifetime, electron recombination lifetime, equilibrium electron density, equilibrium hole density, electrons density when trap energy level is equal to Fermi energy level, holes density when trap energy level is equal to Fermi energy level, excess electron density and excess hole density respectively.

The band to band recombination or radiative recombination is when a hole or electron directly transits from valence or conduction band and recombines with opposite carrier often followed by emission of a photon. The recombination lifetime is given by

$$\tau_{rad} = \frac{1}{B(p_0 + n_0 + \Delta n)} \tag{2.26}$$

where *B* is radiative recombination coefficient and all symbols have their usual meaning. The Auger recombination is when two electrons in the conduction band (or holes in the valence band) collide, one will then combine with a hole in the valence band (or electron in the conduction band) [10]. The life time of Auger recombination process is given by

$$\tau_{Auger} = \frac{1}{C_p(p_0^2 + 2p_0\Delta n + \Delta n^2)} \tag{2.27}$$

where C_p is Auger recombination coefficient for holes and all symbols have their usual meaning. At the front or the back surfaces the recombination occurs through the surface defects. For a solar cell with width (W) having identical surfaces (back and front) the surface recombination lifetime is estimated by equation 2.28.

$$\tau_s = \frac{W^2}{\pi D^2} \tag{2.28}$$

where D is the coefficient of diffusivity. Surface recombination can be detrimental to cell performance especially for materials with high absorption coefficient like GaAs where more carriers are generated very close to the surface. The common solution is to use a thin layer (window) of a high band-gap like AlGaAs or GaInP in GaAs cells, to passivate recombination at the surface of the emitter. The window material absorbs very little light and what it losses due to SRV is not significant. Back surface passivation is occasionally used when the back recombination is expected to be important.

2.5.3 Minority carrier transport

When a piece of doped semiconductor material is excited by a monochromatic light of photon flux density ϕ, wavelength λ, and absorption coefficient α, the generated carriers will start diffusing along the length of the semiconductor. For steady state condition and low excitation conditions, the minority transport is governed by the continuity equation (equation 2.29).

$$D_p \frac{d^2 p_n}{dx^2} + \frac{\Delta n(x)}{\tau} + G(x) = 0 \tag{2.29}$$

where D_p is the minority carrier diffusion coefficient, L is the minority carrier diffusion length, τ is the effective minority carrier lifetime and $G(x)$ is the generation rate. The equation can be applied to p-n junction solar cell under specified boundary conditions and abrupt junction model.

The minority carrier can diffuse for an average one diffusion length (L), before recombining to reach the equilibrium value. The diffusion length of a material is determined by the effective minority carrier lifetime which in turn is dependent upon semiconductor type and crystal quality. The carrier lifetime decrease with increasing doping level. However a direct dependence of lifetime on doping for a specific material cannot be derived as the lifetime is dependent on other material history, like growth rate, post growth treatments like annealing conditions, surface passivation [11]. Minority lifetime carriers for Si and GaAs can be in the orders of 100 microseconds and 10 picoseconds respectively [11]. The diffusion length is related to the minority carrier lifetime through the equation 2.30

$$L = \sqrt{D\tau} \tag{2.30}$$

where L, D and τ are the minority carriers; diffusion length, diffusion coefficient and lifetime respectively.

2.6 Single band solar cell efficiency limit

From the Carnot theorem, the efficiency to transfer energy from a high-temperature reservoir at temperature T_H to a lower temperature reservoir at temperature T_C is described by; $(T_H - T_C)/T_H$. The transfer of heat energy from the sun at T_H~ 6000 K (temperature at surface of the sun) to a solar cell device at temperature $T_C \sim 300\ K$(room temperature) has a Carnot efficiency of ~95 %. This provides an upper bond for all conversion processes [12].

A semiconductor only absorbs photons that are nearly equal to (for indirect band-gap semiconductors) or greater than their band-gap energy. Therefore the photons of lower energy (longer wavelength) of the solar spectrum are mainly transmitted through and lost (figure 2.14). Under the assumptions of detailed balance, the optimum band-gap of a single junction solar cell in AM1.5D spectrum at all concentrations is 1.1 eV [13], which correspond to Silicon(Si) material band-gap. However the highest efficiency (27.8 %) material for one junction device is GaAs despite its non-optimal band-gap of 1.4 eV [13], mainly due to its high absorption coefficient and its direct band-gap. Silicon however account for 90% of the semiconductor devices in use today owing to its abundance and advancement in technology.

For a single junction, the efficiency depends on the band-gap of the material as shown in figure 2.15. This non-linear relation with the increasing band-gap is due to the trade of between current and voltage output. High band gaps results in higher voltage output but lower current output and vice versa for current output.

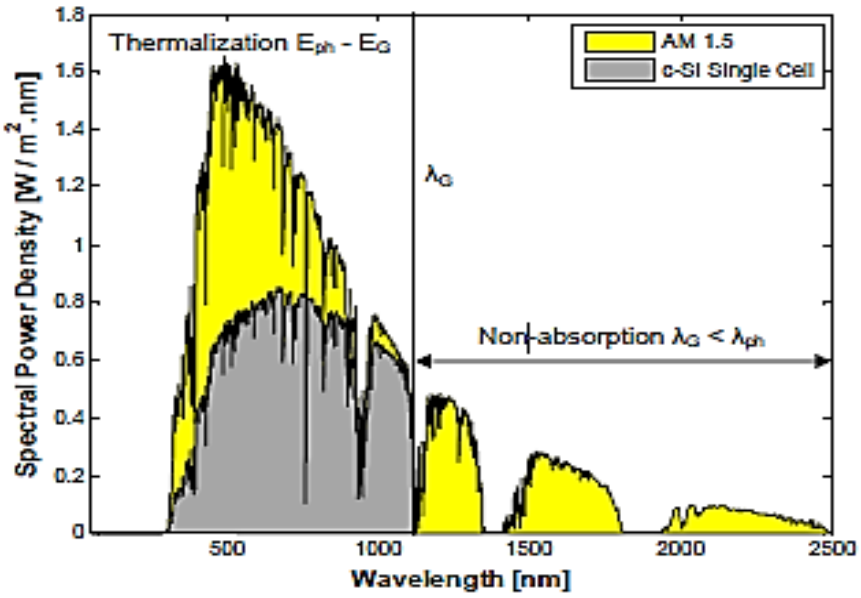

Figure 2.14: Losses in a single junction due to spectral mismatch [4]

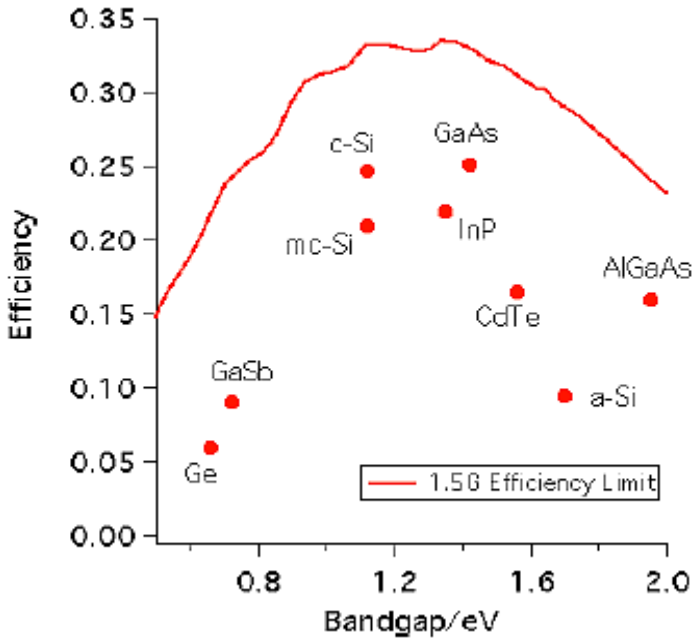

Figure 2.15: Efficiency versus band-gap of a semiconductor for AM1.5G spectrum [14]

2.7 Multi-junction Solar Cells

The efficiency limit of a single junction solar cell can be exceeded by use of multiple junctions. Each junction is tuned to absorb a certain band of the solar spectrum (Figure 2.16). This reduces thermal relaxation and below band-gap photon losses. The choice of band-gap of each material is critical in determining the maximum efficiency possible. Theoretically it is possible to spectrally split the light and illuminate each sub-junction with light of appropriate wavelength range as shown in figure 2.17b. A robust way is building the p-n junction in tandem (figure 2.17 (a)). The tandem structure is in which the p-n junctions are connected in series often using tunnel diodes or other physical means.

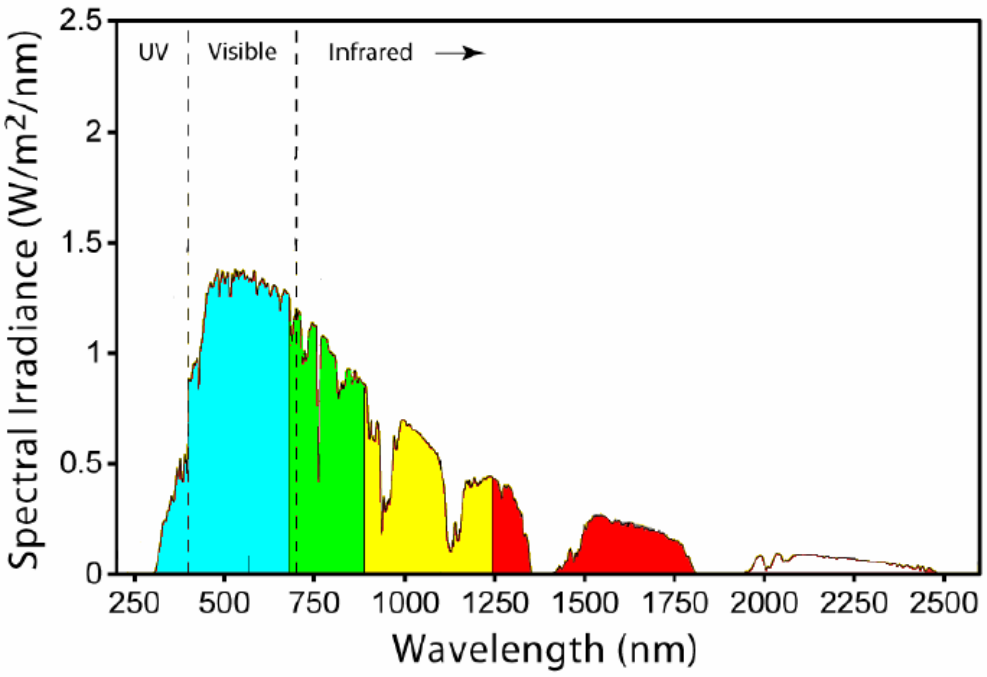

Figure 2.16: The AM1.5G Solar spectrum versus wavelength.

Theoretically as the number of sub-junction used in the multi-junction solar cell is increased thermalisation losses reduce. Thermalisation losses occur when the absorbed photon energy is greater than the band gap of the semiconductor material. The excess energy will be lost through the emission of phonons as the carriers relax to the edge of the conduction and

valence band. However material choice or bandgap engineering, and growth of such devices become more challenging. Nonetheless theoretical efficiencies of 4 junction devices and above, is estimated at more than 50 % [15, 16 and 17], under concentrated spectrum. Practical efficiencies of more than 40 % has been demonstrated with GaInP/GaAs/Ge based devices and such triple junction devices are the most common power generators in space [18].

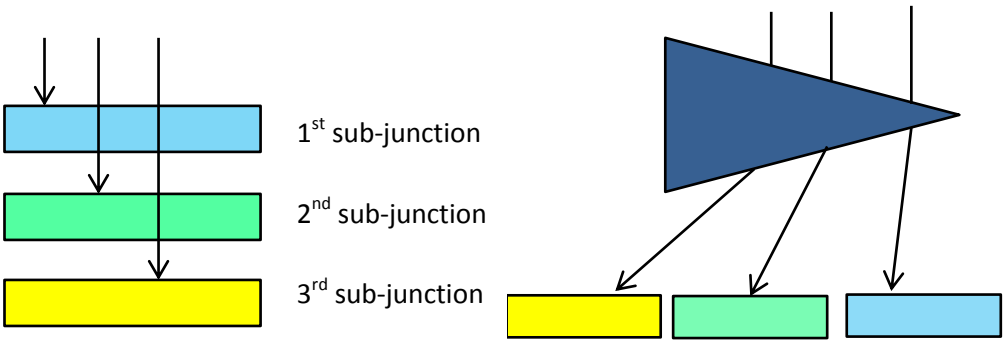

(a) (b)

Figure 2.17: Possible absorption configurations in multi-junction structures; (a) Tandem, (b) spatial

The resulting band gap of a tandem structure is shown in figure 2.18, and the Fermi remaining constant across the entire device length.

The successful application of tandem structures in various devices is due to the capability of epitaxial technology like the Molecular Beam Epitaxy (MBE), to grow of latticed matched dissimilar semiconductors junctions (hetero-structures) with virtually no defects [19]. In order to grow a semiconductor on top of another without defects, their lattice constants have to match.

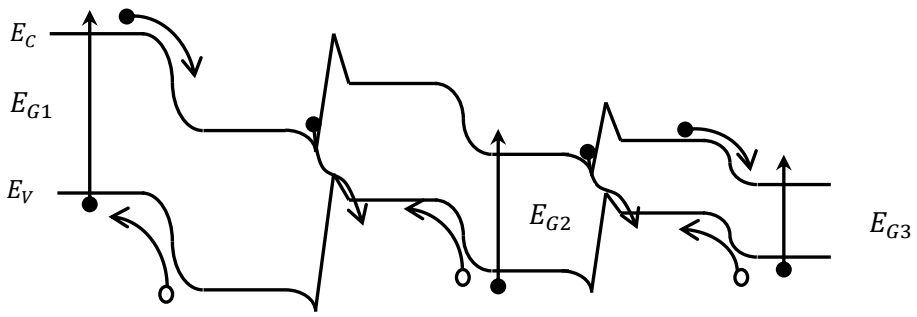

Figure 2.18: Band-gap alignment of a tandem a solar cell.

Silicon at near 1.0 eV is at the optimum position on the solar spectrum and would be the ideal choice in multi-junction solar cells; however III/V materials are more attractive for multi-junction devices due to the wide band gap choice they offer still lattice matching GaAs substrates. One of the limitations of the tandem solar cell is that, the current is limited by the lowest current produced by any of junctions. Current matching is required for the structure and one technique that has been extensively used for that is the use of Quantum Wells (QW) in the intrinsic region of the P-I-N structure.

2.8 Dilute Nitrides Physics

Dilute Nitrides have emerged from the conventional III-V semiconductors such as GaAs or InP by the insertion of nitrogen into the V group sub-lattice, which results in an anomalous band-gap reduction and a profound effect on electronic properties of the material [13]. This band-gap reduction gives flexibility in designing lower band-gap optoelectronic devices. The band-gap reduction when small fractions of nitrogen were added to the III-V materials could not be modelled by the Virtual Crystal Approximation and other phenomenal models [10]. The reduction in the band-gap was explained well by the band anti-crossing interaction between the conduction band edge and a band of higher lying localized nitrogen states [21]. Since then the Band Anti-Crossing Model developed by Shan et al [20] has been used extensively applied in the study of the dilute nitrides.

When Nitrogen is added to GaAs it creates an isolated state just above the conduction minima of the conduction band [22]. This isolated energy E_N^0 state is commonly taken as ~1.7 eV measured from the valence band of GaAs. For percentages of Nitrogen less than 5% the interaction of the isolated energy states result in a localised resonance level which is lower in energy. This localized energy level is given by

$$E_N = E_N^0 - \gamma y \tag{2.31}$$

The interaction between the highly localized N states E_N with the conduction band is calculated using perturbation theory as shown in equation 2.32.

$$\begin{vmatrix} E(k) - E_M(k) & V_{MN} \\ V_{MN} & E(k) - E_N \end{vmatrix} = 0 \tag{2.32}$$

where, $E_M\ (k)$ is the energy of the conduction band states of the host alloy, which is GaInAs in the case of GaInNAs. This is parabolic with k as shown in equation (2.33),

$$E_M(k) = E_M(0) + \frac{\hbar^2 k^2}{2m^*} \tag{2.33}$$

where $E_M(0)$ is the band-gap of $Ga_{1-x}In_xAs$ which varies with Indium composition x and V_{MN} is matrix element describing the interaction between the conduction band and the nitrogen isolated states. This results in a two solution dispersion relation equation (2.34) suggesting the band splitting;

$$E_{\pm}(k) = \frac{E_N + E_M(k) \pm \sqrt{(E_N - E_M(k))^2 + 4V_{MN}^2}}{2} \tag{2.34}$$

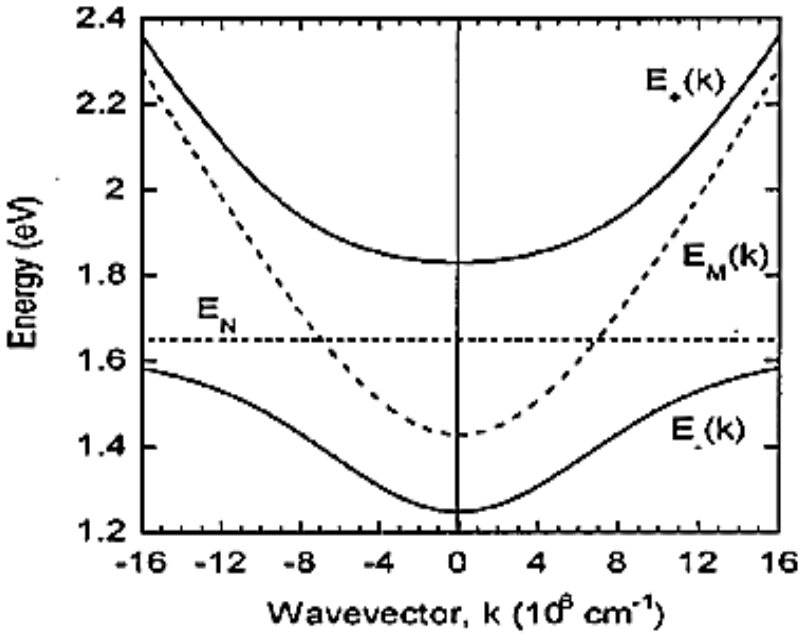

Figure 2.19: Band Anti-Crossing for Dilute Nitrides [23].

Some quaternary dilute nitride alloys which are of more interest owing to their ability to lattice match GaAs lattice over a wide range of band-gaps include the GaInNAs and GaInPAs systems as shown in figure 2.20. GaInNAs alloy allows independent control over the In: Ga and N: As ratios. Increasing the In: Ga ratio causes a reduction of band-gap and an increase in lattice parameter, while increasing the N: As ratio also causes band-gap reduction, but a decrease in the lattice parameter. Therefore GaInNAs, gives the flexibility of tailoring both band-gap and lattice parameter [10]. The lattice matching of GaInNAs to GaAs is possible at the Indium proportion of $Ga_{1-3x}In_{3x}N_xAs_{1-x}$ [24]. As stated in the introduction the alloy reduces band-gap with increase in nitrogen. This enables the design of lower band-gap solar cells targeted at harvesting low photon energy portion of the solar spectrum.

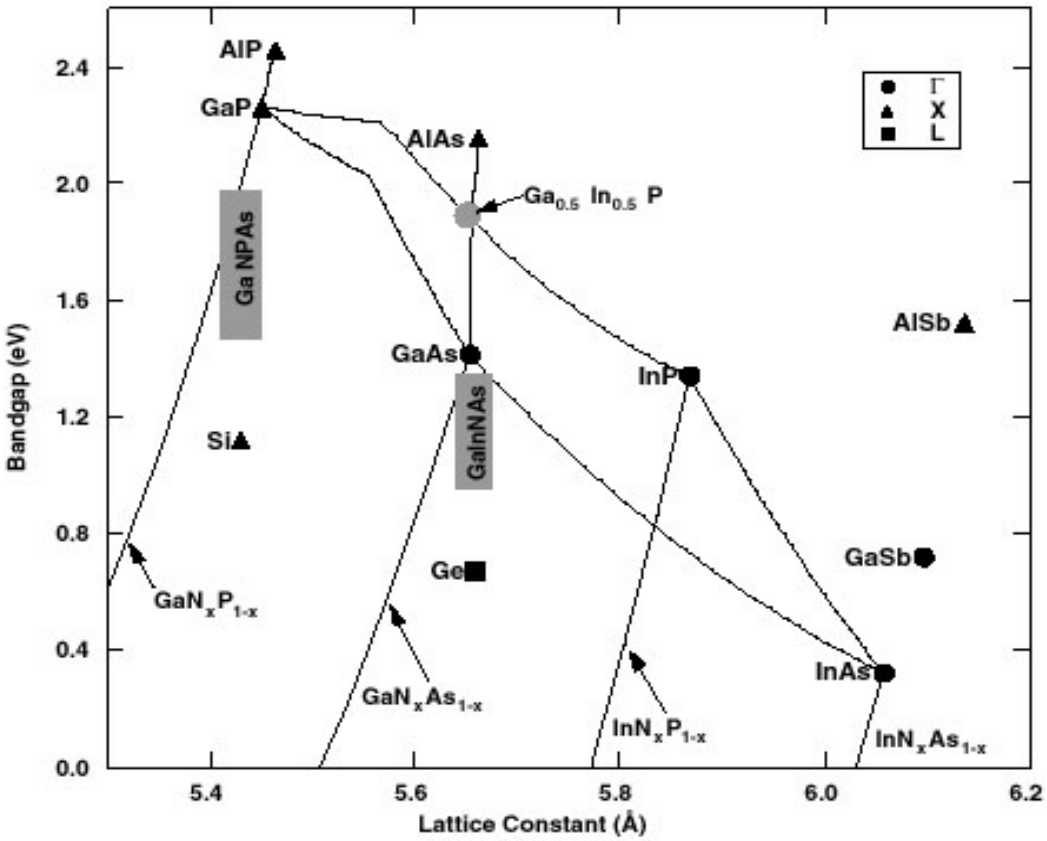

Figure 2.20: The relationship between bandgap and lattice constant for alloys in the GaInNAs and GaInPAs systems [25].

2.9 Dilute Bismides Physics

Bismuth containing semiconductors had been grown as early as 1980s. Growth of InSbBi by Molecular Beam Epitaxy (MBE) was reported by two groups in 1995, the Kyoto Institute of Technology (KIT) being one of them. The KIT proposed the growth of GaInAsBi as a promising compound for a more temperature insensitive lasers. The KIT has since then grown and studied the properties of Bismuth containing semiconductors like, GaAsBi, InAsBi, GaNAsBi and GaInAsBi. Photoluminescence results have shown that the band gap for GaAsBi is temperature insensitive. Growth of Bi containing semiconductors is not favourable with Metal Organic Vapour Epitaxy (MOVPE). Because of the requirement of

low temperature growth for incorporation of Bismuth, the co-existing metal organics in MOVPE are not completely decomposed and they tend to contaminate the epilayer [26].

With MBE GaAsBi, InAsBi, GaNAsBi and GaInAsBi compounds had been grown successfully, but not without challenges. Growth of GaAs/GaAsBi quantum wells with smooth interface has been demonstrated despite problems of Bismuth segregation [26]. GaAsBi based alloys' response has been extended to longer wavelength growth of InGaAsBi and GaNAsBi. The growth conditions are exactly the same as those of InSbBi; Low temperature growth typically less than 400 °C, with As (Sb) flux adjustment in limited range [26]. The low temperature growth and low V/III ratios are required to keep Bismuth from segregating to the surface of the epilayer, as it has a tendency to do so [55].

2.9.1 Valence Band-Anti-Crossing (VBAC) Model

Valence Band Anti Crossing (VBAC) model, Figure 2.21, applied to bismides had been able to account for the large band-gap reduction and huge spin orbit splitting that could not be readily be explained by VCA models and other phenomenal models [10]. This is a modified model from the dilute nitrite BAC matrix to VBAC matrix to calculate valence band interaction with the Bi 6 p-like localised states. For GaAs to GaBi a reduction of -1.45 eV and a spin orbit splitting of 2.15 eV are expected [56]. For GaAs base alloy $GaBi_xAs_{1-x,}$ the Bismuth localised states (defects states) are at 0.35eV.

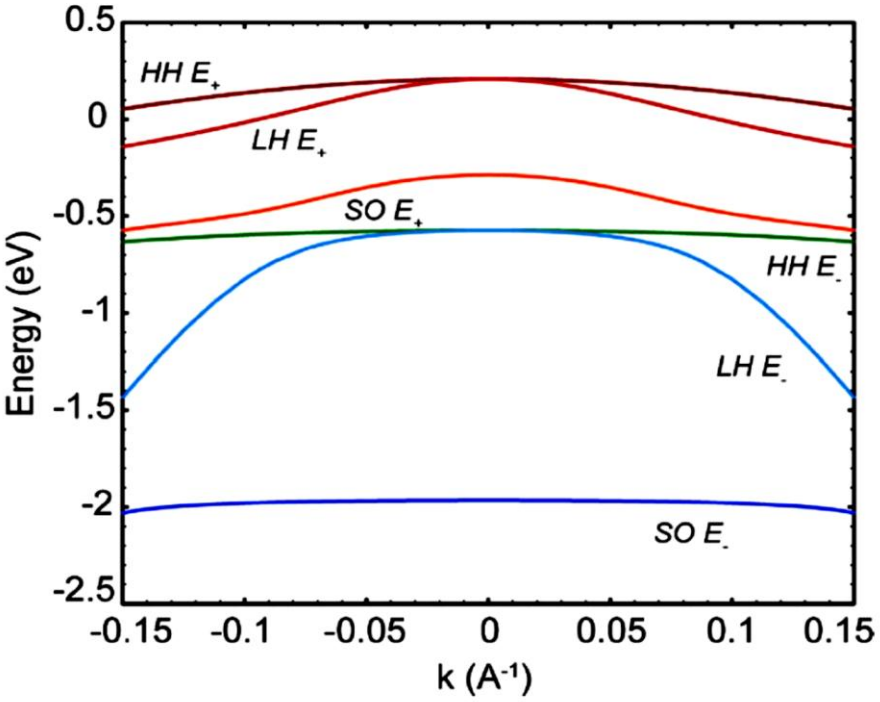

Figure 2.21: Valance Band Anti-Crossing (VBAC) for $GaBi_{0.01}AS_{0.99}$ [27].

The bang-gap reduction in Bismides has been reported within the range 60-90 meV/% of Bi [28 and 29]**.** Figure 2.22 shows effect of Bismuth concentration on band-gap and spin orbit splitting in the GaAsBi alloy.

The Bismides exhibit a huge Spin Orbit splitting is observed, and that is strongly compositional dependent. This can make Bismuth containing semiconductors important in spintronics**.**

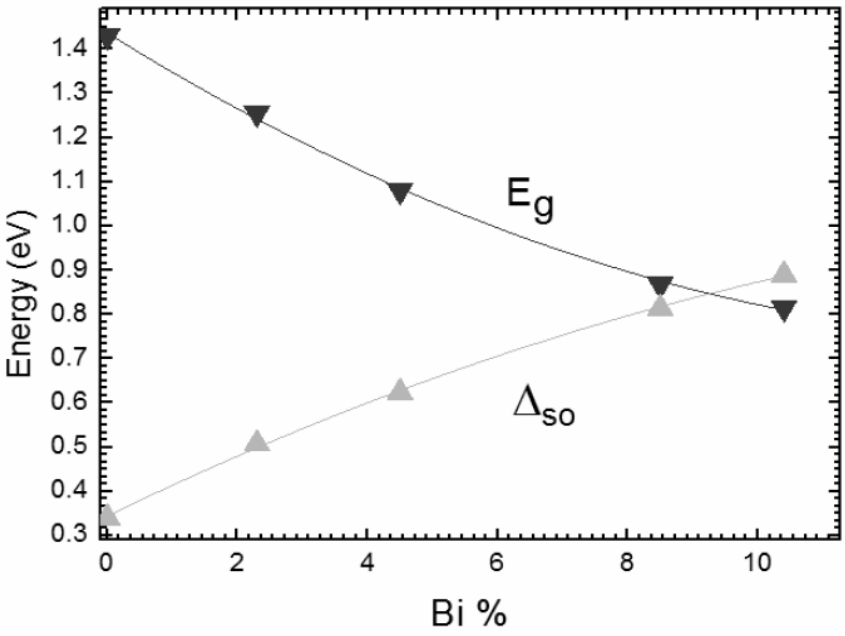

Figure 2.22: Effect of Bismuth concentrations on band-gap and spin orbit splitting in the GaAsBi alloy [28].

2.9.2 Bismuth potential in photovoltaics

For any new alloy to be considered for application in photovoltaic, its absorption and carrier transport, especially minority carrier transport has to be studied [25]. If the diffusion length of minority carrier is short the material does not effectively collect photo-generated carriers. Optical absorption is also very important and besides other factors, it depends on the effective mass of carriers in the semiconductor.

Minority carrier lifetimes of less than 2 ns, for GaAsBi bulk material with less than 3% Bismuth concentration, measured by Time Resolved Photoluminescence (TRPL) have been reported by Mazzucato et al.[30].

Mobility in bismides has been reported by Kini et al. [31] in n type GaAsBi alloys with bismuth concentration of less than 1.6 %, to be nearly the same (~2100 cm^2 Vs) as that of GaAs alloy (2322 cm^2 Vs).

The effective mass of electrons in GaAsBi is often assumed to be equal to that of GaAs since the addition of small amount of Bismides leaves the conduction band unchanged. The hole effective mass of GaAsBi is not well known, but expected to be greater than that of GaAs because of the apparent broadening of the Valance Band for holes predicted by the VBAC given by

$$m^*(E) = m^*(GaAsBi)\left[1 + \left(\frac{V_{MN}}{E_N - E}\right)^2\right] \tag{2.35}$$

Some researchers have assumed the values of 0.55 and 0.10 for heavy holes and light holes respectively.

There is an unexpected carrier effective mass on $GaBi_xAs_{1-x}$ for x < 8 %, however a huge decrease in carrier effective mass that sets in for x > 8 % [26]. This significant carrier effective mass reduction can be favourable for photovoltaic devices where charge has to be rapidly collected to outside circuit**.**

2.9.3 Comparison with Dilute Nitrides

Unlike the dilute nitrides the dilute bismides are expected to perform better in photovoltaic, because of negligible electron offset (figure 2.23) which results in negligible effects on electron mobility. In the Bismuth containing dilute nitride like GaAsNBi, an equivalent band gap reduction can be achieved with a significantly less N compared to that of GaInNAs. Thus, it should be possible to obtain GaAsNBi based 1.0 eV band-gap material with a relatively longer carrier diffusion length due to relatively lower N composition which otherwise is detrimental to the electron mobility. This would improve performance of dilute nitride and bismide solar cells which is adversely affected by the low carrier diffusion lengths. Another advantage of incorporating N and Bi in GaAsNBi is reduction of strain.

This is expected as the small N and big Bi radii will compensate each other's effect on the epilayer.

Owing to huge Spin Orbit splitting and separation $GaBi_xAs_{1-x}$ can find application in the intermediate band gap solar cells, if the interaction between impurities and host material states can form a band gap in between them. The advantage of intermediate band-gap solar cell is that of having only one PN junction. This makes fabrication easier and no defects that otherwise plague the multi-junction structures.

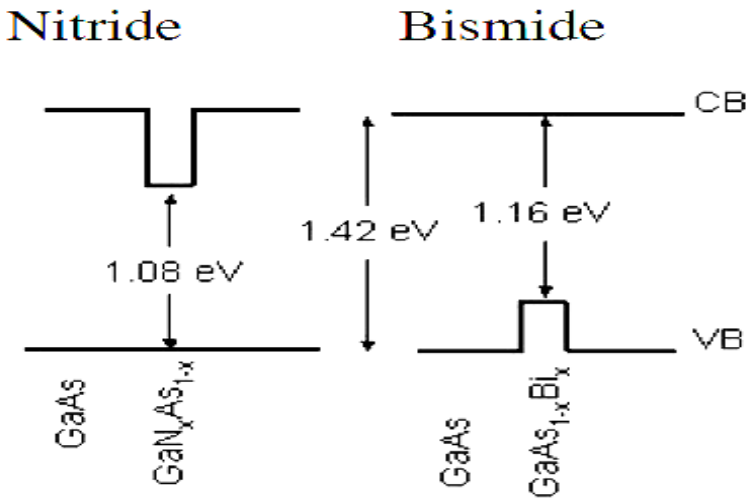

Figure 2.23: Schematic band alignment of GaAs/GaNAs and GaAs/GaAsBi for 3% composition of N and Bi [32].

The $GaAsBiN$ alloy for the composition $Ga(N_{0.33}Bi_{0.67})_zAs_{1-Z}$ [32], lattice matches to GaAs, however the incorporation of Nitrogen still poses challenge to many growers. When growing GaAsBi on GaAs substrates care must be taken not exceed the critical thickness which will result in relaxation of the epilayer.

2.10 Common designs for dilute nitride and bismide solar cells

2.10.1 P-I-N structure

A p-i-n structure is a p-n junction in which a nominally un-doped (intrinsic) layer has been grown between the p and n layer. The inbuilt potential of the p-i-n junction is the same as that of a p-n junction with the same doping concentration. The un-doped region serves to extend the space charge region (SCR), therefore the electric field region is extended, though it becomes weaker.

The importance of the SCR is that the quantum efficiency is high, often taken as 100 % [25] due to drift dependent collection of carriers. This design is important for materials of short diffusion lengths [3], like the dilute nitrides. Figure 2.24 shows the band structure for a p-i-n junction

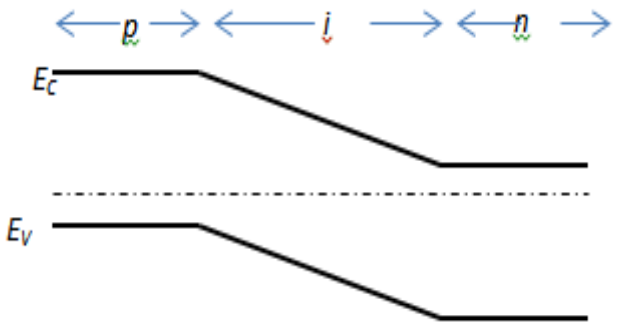

Figure 2.24: Band structure of a p-i-n homojunction.

The major problem with the p-i-n structure is the background doping. The background doping imposes a limit on the thickness of the intrinsic layer that can be grown before the electric field gets cancelled out. J. Connolly in his Ph.D. work [33] demonstrated the method of

determining the maximum tolerable background doping for a p-i-n structure as shown in equation (2.36)

$$N_{BG}^{n} = \frac{N_A}{2}\left[\sqrt{1 + \frac{8\epsilon(-V_{bi} - V_{sh})}{q x_i^2 N_A}} - 1\right] \tag{2.36}$$

Where N_A is the acceptor concentration, ϵ is the semiconductor permittivity, V_{bi} is the built-in potential and V_{sh} is the measured voltage at the shoulder (where the J-V graph shows sudden reduction of photocurrent) and x_i is the thickness of the intrinsic region.

This sudden reduction in photocurrent as the voltage increases is when the electric field is cancelled by the intrinsic region field.

Secondly a non-depleted region with relatively low doping compared to the n and p, serves to increase the cells resistance and degrade its performance which is detrimental in concentrator cells where the cell produces higher densities of photogenerated currents.

The third limitation of the p-i-n structure is the inherent recombination in the SCR which is directly proportional to the intrinsic layer thickness. The increased recombination increases the dark current density and consequently lowers the V_{oc} [34].

With the MBE growth techniques enabling growth of lower background doping ($<10^{15}$ cm^3), GaInNAs depletion regions as wide as 3 µm were achieved, resulting in improvement of Quantum Efficiency up to 90 % [34 and 35].

2.10.2 Quantum well solar cells

In its simplest form quantum well solar cell consists of a p-i-n solar cell with multi-quantum wells (MQW) system added to the intrinsic (i) region, as shown in figure 2.25. The I-V characteristics of the MQW solar cells are more or less the same as that of the conventional solar cells. Superposition of dark current has been verified for both. MQW solar cells are observed to have lower diode ideality factor than conventional single cells counterparts. This lower ideality factor has been attributed by some researchers to bias dependent escape and recombination mechanisms in quantum wells. [36].

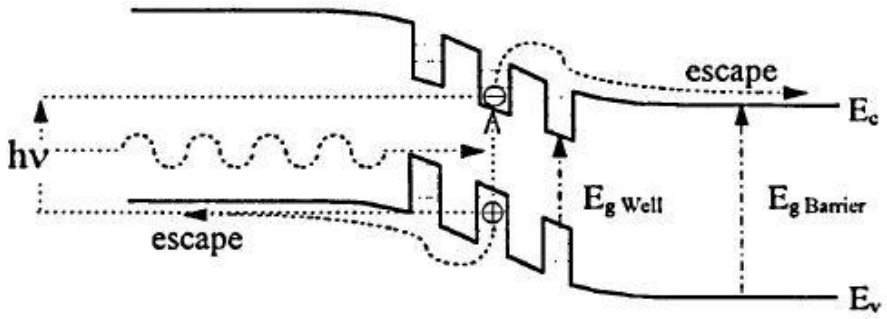

Figure 2.25: Multiple Quantum well solar cell band-gap structure [36].

Theoretically MQWs p-i-n structures should enable harvesting lower energy photons in the spectrum without paying the full price of voltage loss [37]. An ideal theory of operation of MQW solar cell has been developed by Anderson [38]. Anderson model compares the p-i-n MQWs solar cells to the standard p-n junction and it shows possibility of efficiency enhancement. The J_{sc} and V_{oc} of the standard p-n junction (baseline) and the p-i-n MQWs from the N. Anderson model are shown in equations 2.37 and 2.38,

$$J_{scB} = -qWG_B|_{opt} \tag{2.37}$$

and

$$V_{ocB} = \frac{kT}{q} ln\left(\frac{|J_{scB}| + J_o(1+\beta)}{J_o(1+\beta)}\right) \tag{2.38}$$

where $W, G_B|_{opt}$, V_{ocB}, J_{scB} and β are the intrinsic region width, the average optical generation rate in the intrinsic region, the open circuit voltage, the short circuit current generated by the baseline and β is the ratio of the current required to feed radiative recombination in the intrinsic region at equilibrium to the usual reverse drift current resulting from minority carrier extraction. The Anderson model shows that for a p-i-n with MQWs the short circuit and the open circuit voltage are given by

$$J_{scQW} = -qW[f_w G_w|_{opt} + (1-f_w)G_B|_{opt}] \tag{2.39}$$

$$V_{ocQW} = \frac{kT}{q} ln\left(\frac{|J_{scQW}| + J_o(1+r_R\beta)}{J_o(1+r_R\beta)}\right) \tag{2.40}$$

where f_w, r_R , $G_w|_{opt}$ is the fraction of the intrinsic region replaced by quantum wells, radiative enhancement ratio and optical generation in QWs. The radiative enhancement ratio has a strong dependence on the conduction and or valence band offset ΔE. Comparing the equation for baseline cell open circuit voltage (V_{ocB}) with that of the MQWs cell open circuit voltage (V_{ocQW}), it can be seen that the factor r_R in the latter will result in a reduced open circuit voltage. The inclusion of QWs is expected to increase the short circuit current J_{scQW} compared to the baseline short circuit J_{scB} as QW tends to absorb lower energy photons in the spectrum.

Browne et al [13] has demonstrated an InGaAs/GaAs QW p-i-n solar cell and later an InGaP/GaAs based quantum well tandem solar cells which has achieved efficiency of 30.6% under 54 suns AM1.5g. Even though the open circuit voltage was reduced the as predicted by the Anderson model discussed above, the increase in short circuit was still sufficient to

increase power appreciably above that of a conventional solar cell. The output voltage of the QWSC is found to be dominated by the wider band-gap barrier material, the recombination in the wells and in the barrier-well interfaces.

Introduction of quantum wells into the intrinsic region has been shown to invariably lower the open circuit voltage [36], but the efficiency may still increase if the baseline cell's band gap is greater than or equal to its optimum value for the illuminating spectrum [38], Richard Corkish and Martin A Green [37], further investigated the performance of AlGaAs QWs and their finding showed that the earlier models had overestimated the expected efficiency increase, however QWs will still result on incresed efficiency.

The effect of depth of QWs has been investigated by a number of researchers, with findings that the deep wells results in the degradation of the quantum well solar cell performance, and the added advantage of many confined energy states in deeper wells does not always account for the loss in voltage due to recombination in the wells. [36, 39 and 40] The effect of depth on carrier escape from QWs was found to be larger than that of the carrier effective mass [41], as shown in equation 2.46, which has an exponential dependence on depth of the well (ΔE) as opposed to carrier effective mass direct proportinality dependence.

$$\frac{1}{\tau_{thermal}} = \frac{1}{Lw}\sqrt{\frac{k_B T}{2\pi m_w}}\, exp\left(-\frac{\Delta E}{k_B T}\right) \tag{2.41}$$

where L_w is the quantum well width, m_w is the carrier mass (in this case, the electron) and ΔE is the energy difference of barrier and the energy level.

The thinner quantum wells allow more wells to be included, while the wider wells results in fewer interfaces and hence fewer recombination regions [42]. This clearly shows that an optimum width for high performance needs to be carefully designed. Simulation results

showed that short circuit current increases with increasing well width [36]. The escape rate of carriers is strongly dependent on the electric field, suggesting modulation doped structures could enhance carrier escape from quantum wells [42]. This agrees with [43] experimental results in superlattices solar cells, which showed a degraded, QE at both high forward and reverse bias. The time required for carrier escape from quantum wells increases as the applied electric field decreases across the quantum well [44].

2.10.3 N-I-P-I Structure

The n-i-p-i structure consists of a number of layers whose doping alternates between n-type, intrinsic, p-type and intrinsic [45, 46, 47 and 48]. This layer configuration gives rise to sinusoidal-like band alignment as shown in figure 2.26.

The thickness of the layers of the n-i-p-i structure are kept within the diffusion length of the bulk material, therefore photo-generated electron-hole pairs generated anywhere in the device will be rapidly separated to adjacent layer before any significant recombination takes place. The separated carriers then diffuse along the parallel layers towards the lateral selective contacts, to be collected in the external circuit.

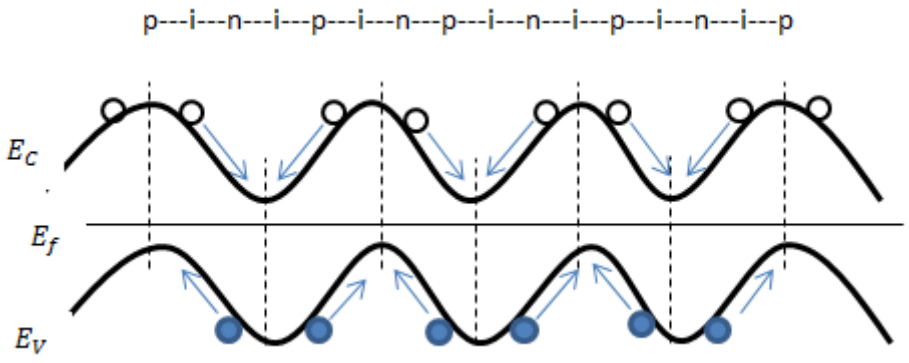

Figure 2.26: Band diagram of the n-i-p-i, structure.

A properly designed n-i-p-i can be almost insensitive to short diffusion lengths, which is very important in addressing the inherent problem of short diffusion lengths in the dilute nitrides and bismides. Some limitations of the n-i-p-i structures is the low minority carrier diffusion in the transverse region hence poor carrier collection. If the repeating layers of the n-i-p-i becomes too thin unwanted carrier confinement and subsequently increased recombination results. However the n-i-p-i structure has an advantage of real space gap between electrons and holes which greatly reduces the recombination rate. Lastly the inherent problem of the n-i-p-i that is deterring its application to many devices is the inherent dark current due to repeated SCRs. The dark J-V characteristic for n-i-p-i structure is modelled by equation 2.42,

$$J = \sum_{k=1}^{N_L} J_{0,qnr}\left(\exp\left(\frac{qV}{kT}\right) - 1\right) - \sum_{m=1}^{N_J} J_{0,qnr}\left(\exp\left(\frac{qV}{kT}\right) - 1\right) \tag{2.42}$$

where $N_L$the number of layers is, N_J is the number of homojunctions ($N_L - 2$).

2.11 Review of 1.0 eV junction

The interest in dilute nitride alloys for photovoltaics applications was motivated by the discovery by Weyers et al [49] of the anomalous large band-gap bowing in GaNAs.
Initial interest was for the development of long wavelength lasers operating at 1.3 μm window. The dilute nitride showed a better electron confinement in quantum wells compared to the InP quantum wells. The dilute nitride based lasers were expected to address the problem of strong temperature dependence exhibited by InP based lasers due to poor electron confinement [50]. It was soon realised that this material can be a good candidate for the

highly sought 1.0 eV junction for high efficiency multi-junction solar cells. The first dilute nitride solar cell fabricated had very low short circuit current density (~2.0 $mAcm^{-2}$) and a an open circuit voltage that ranged between 0.35 and 0.44 V. This poor performance was attributed to short diffusion lengths [17 and 25]. It was quickly discovered that addition of N to GaAs to form the dilute nitride alloy has a dramatic effect not only on the band gap, but also on the minority-carrier diffusion lengths L_e and L_h for electrons and holes, respectively. Although the diffusion lengths could not be directly determined, the observation from the results is that the GaInNAs diffusion lengths are much lower than that of GaAs For GaAs, L_e for electrons can easily be 10 μm or more, whereas for GaInNAs, L falls into the 0.1 to 1μm range, at the best. These minority diffusion lengths are 50-100 times lower than in comparable GaAs [15].

The short diffusion lengths exhibited by dilute nitrides poses a challenge for developing a GaInNAs sub-cell for the multi-junction, in particular the GaInP/GaAs/Ge triple junction (3J) which is currently in production but cannot make efficient use of all the light that reaches the Ge junction. With the poor minority carrier properties reported immediately by a number of researchers, the inclusion of GaInNAs as a sub-cell in multi-junction was becoming elusive. Especially that for the structure to be current matched it requires near unity quantum efficiency from the GaInNAs over its bandwidth. This subsequently triggered a number of ideas and research work. A p-i-n structure was the first to be tried to aid the carrier collection by the drift in the depletion region. Theoretical results were enticing as they predicted that the wider the depletion region the higher would be the quantum efficiency [17]. However as soon as the p-i-n structures were grown problems were observed. Achieving a low background doping that would allow the increased depletion region (intrinsic region) was very difficult to achieve especially with the Metal Organic-Vapour Phase Epitaxy growth (MOVPE), which

resulted in high background doping up to $1x10^{17}$ cm^3 [17, 34 and 51] mainly attributed to carbon contaminants during growth, which only resulted in a depletion region of ~0.2 µm, yielding internal quantum efficiency as low as 20 %. Ultimately with the use of MBE growth techniques a light doped background enabling depletion regions as wide as 3 µm were achieved, resulting in improvement of Quantum efficiency to around 70 % [34, 35]. However the longer the depletion, the poorer the V_{oc}, this is due to the increased recombination and its associated dark current [34]. Lately it was discovered that increasing the depletion region far beyond the very short minority diffusion length, suddenly drastically lower the performance contrary to the models predictions [51].

Recent analysis of the GaInNAs materials and its solar cells revealed that the poor efficiency, due to low diffusion lengths that are attributed to a shallow electron trap and a deep recombination centre [15].

David B. Jackrel et al [52] carried out a study that was focused on two techniques aimed at improving the quality of dilute nitride films grown by molecular beam epitaxy. In his experiment, dilute nitride, GaInNAsSb, films were grown with and without biased deflection plates, and with and without antimony, and solar cells were fabricated from these materials. The biased deflection plates improved every aspect of GaInNAs solar cell performance. It is possible that the use of deflection plates reduced the dark current density in the GaInNAs films, which would partially explain the improvement in solar cell characteristics. The use of antimony in the GaInNAsSb solar cells improved the collection efficiency, but degraded the open circuit voltage and fill factor. Nevertheless, the GaInNAsSb devices are the first dilute nitride solar cells to generate enough short-circuit current to current-match to the upper sub-cells in a state-of-the-art three-junction solar cell.

Another technique is to increase the number of junctions to reduce the requirement of current on the GaInNAs sub-cell for current matching. An AlGaInP/GaInP/AlGaInAs/GaInAs/Ge quintuple-junction (5J) solar cell has been demonstrated by Fraunhofer ISE. A V_{oc} of 5.2 V nearly double that of a typical triple junction (3J) solar cell, has been achieved with the 5J solar cell. However the accompanying current reduction observed in the 5J solar cell offset any efficiency increase over the current triple junction (3J) solar cells [57]. The project for such increased junctions is illustrated by models in the figure 2.27.

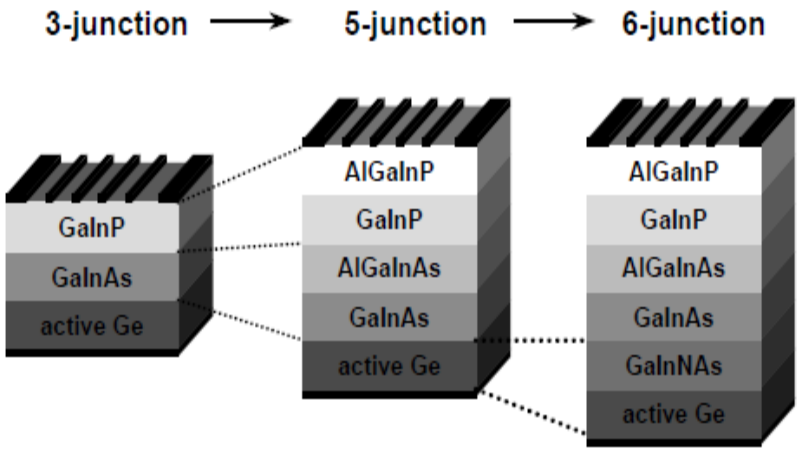

Figure 2.27: The models of quintuple and sextuple junction solar cells proposed by the Fraunhofer Institute [57].

Recently, metamorphic tandem solar cells in which certain degrees of lattice mismatch is allowed, is under study. The metamorphic tandem solar cell has a reached an efficiency of 40.7 %, breaking the record that had been held by monolithic tandem solar cells for the AM1.5D spectrum concentrated to 240 suns [18]. Work is continuing to investigate the effect of threading dislocations in metamorphic solar cell for possible improvement of the efficiency. Besides going metamorphic, a number of designs like the multiple quantum wells and n-i-p-i had been tested for possible application in dilute nitride tandem solar cell sub-junctions. Yunpeng Wand et al [43] demonstrated a superlattice (SL) structure with 3.1 nm

thick barriers and more than 100 strain balanced QWs that enabled tunnelling across the QWs. The design enhanced current of the p-i-n structure from 22.6 A/cm^2 to 25.6 A/cm^2 and mostly importantly reduced typical voltage loss due to recombination in QWs to just 0.03V. The overall efficiency of the GaAs p-i-n was enhanced. Later Yunpeng Wang et al [53] designed and demonstrated a Multi Stepped Superlattice which enhanced current and open circuit voltage of their previous SL by 2.0 mAcm^2 and 0.2 V respectively. Gopti Vijaya et al [54] designed a cascaded quantum well solar cell to overcome the long carrier escape time and recombination in deep wells. This new cascaded quantum well design uses thermally assisted resonant tunnelling process to accelerate the carrier escape process to less than 30 picoseconds. Another method of carefully positioning the quantum wells away from regions of high recombination centres has been deployed. An investigation of the effect of shifting the well within the intrinsic region has been achieved by comparison of the theoretical and experimental dark currents from single wells grown at $1/4$, $1/3$ and $3/4$ positions within the intrinsic region [36]. Recent interest has developed in a new material system based on GaAsBi (dilute bismides) and is currently being studied and tested for potential application in photovoltaics and most importantly the highly sought near 1.0 eV sub-junction for tandem solar cells.

2.12 Conclusion

Dilute nitrides and bismides are still invaluable, owing to the flexibility of tuning their band-gap over a wide range while lattice matchicig GaAs. However short diffusion lengths observed in dilute nitride and bismide materials make it a challenge to design solar cells with conventional design that works well for the GaAs. For multi-junction solar cells solar cells to give performance closer to projected outputs, a 1.0 eV sub-junction with good optical and electrical properties is needed. However the quality of the current dilute nitrides and bismides

are not good enough to enhance efficiency of multi-junction solar cells. While the material quality of the dilute nitride and bismide is under study, photovoltaic specialist are also working on novel designs that can curb the effects of the poor electrical and optical properties of this materials.

_____

References

[1] B. Royal, "*GaInNAs/GaAs multiple quantum well solar cells*", PhD. Thesis, University of Essex, 2011

[2] C. Hu, "*Modern semiconductor devices for integrated circuits*", Vol. 1, Upper Saddle River, NJ: Prentice Hall, 2010, pp. 121.

[3] J. Nelson, "**The physic of solar cells**", Imperial College Press, 2003, pp. 146

[4] M. Zeman, "**Introduction to photovoltaic Solar Energy**", Solar Cells, collegematerial, 2003, http://aerostudents.com/files/solarCells/solarCellsTheoryFullVersion.pdf

[5] R.R. Ludeman, **"Introduction to electronic devices and circuits**", Sunders College publishing, 1990, pp. 761

[6] W. Walukiewicz, "*Adavanced concepts and materials for efficient solar energy conversion"*, presentation at CLEO: Applications and Technology, 2011 (Baltimore)

[7] E. F. Schubert, "**Light-emitting Diodes, 2nd Edition, Cambridge University Press**, 2006

[8] M. Beaudoin, A.J.G. DeVries, S. R. Johnson, H. Laman, and T. Tiedje, "Optical absorption edge of semi-insulating GaAs and InP at temperatures", Appl. Phys. Lett., Vol 70, pp. 3540 (1997).

[9] E. Strohm, **"Optical and Electrical Properties of Dilute $GaIn_xAs_{1-y}$ alloys", Msc thesis,** University of British Columbia, 2002.

[10] R. J. Potter "**Optical Processes in Dilute Nitrites**", PhD. Thesis, University of Essex, 2003

[11] H. J. Hovel, "**Solar Cells", Semiconductors and Semimetals, Vol. 11,** Wilardson Beer, 1975.

[12] R. A. Serway and J. Jewett, "**Physics for Scientist and Engineers with Modern Physics**", 6th Edition, David Harris, 2004

[13] B. Browne, N. Ekins-Daukes, A. Ioannides, J. Connolly, I.M. Ballard1, I. Barnham, K. Tibbits T, M. Pate, M. Green, J. Roberts, G. Hill, C. Calder, R. Airey, G. Smekens, J. V. Begin, "*Tandem quantum well solar cells*", Proc. 33rd IEEE Photovoltaic Specialists Conference, (2012)

[14] Mathew Guenette, "The efficiency of photovoltaic solar cells at low temperatures", Honours thesis, Emperial College of London, 2006

[15] A.J Ptak et al., "*Defects in GaInNAs: What We've Learned so Far*"**,** Presented at the National Centre for Photovoltaics and Solar Program Review Meeting, 2003.

[16] S. R. Kurtz, D. Myers, W. E. McMahon, J. F. Geisz, M. Steiner, *"A comparison of theoretical efficiencies of multi-junction concentrator solar cells",* Prog. Photovolt: Res. Appl., Vol. 16, pp. 537-546, (2008)

[17] D. J. Friedman, J. F. Geisz, S. R. Kurtz, and J. M. Olson, *"1-eV GaInNAs Solar Cells for Ultrahigh-Efficiency Multi-junction Devices",* Presented at the 2nd World Conference and Exhibition on Photovoltaic Solar Energy Conversion; 6-10 July 1998, (Vienna).

[18] R. R. King, D.C. Law, K. M. Edmondson, C.M. Fetzer, G.S. Kinsey, H. Yoon, R. A. Sherif, N. H. Karam, *"40% efficient Metamorphic GaInP/GaInAs/Ge multi-junction solar cells",* Applied Physics Letters Vol. 90, pp. 183516, 2006

[19] **S.M.** Sze, K. NG. Kwok, **"Physics of Semiconductor Devices", 3rd Edition,** Wiley Interscience, 2006

[20] W. Shan, W. Walukiewicz, J.W. Ager III, E.E. Haller, J.F. Geisz, D.J. Friedman, J.M. Olson, S.R. Kurtz, "Band anticrossing in GaInNAs alloys", Physics Review Letters. Vol. **82**, pp.1221, (1999).

[21] I. A. Buyanora, W. C. Chen, eds. "**Physics and Applications of Dilute Nitrides**", CRC Press Vol. 21, pp. 396-420, 2004

[22] C. A. Broderrick, M Usman, S J Sweeney and E. P. O'Reilly, *"Band engineering in dilute nitride and bismide semiconductor lasers"*, Semiconductor Sci. Technology, Vol. 27, No. 9, 2012.

[23] C. Skierbiszewski et al., *"Large, nitrogen-induced increase of the electron effective mas in* $In_yGa_{1-y}N_xAs_{1-x}$," Applied Physics Letters, Vol. 76, No. 1724, 2000

[24] D.J. Friedman et al., *"Hydrazine N source for growth of GaInNAs for solar cells",* Photovoltaics for 21st Century: Proceedings of the international Symposium, Vol. 99, No. 11, The Electromechanical Society, 1999.

[25] J. F. Geisz and D. J. Friedman, "111-N-V semiconductors for solar photovoltaic applications" Semiconductor Sci, Technol. Vol. 17, No 8, 2002

[26] Yoshimoto, M. and K Oe; *"Present status and future prospects of Bi-containing semiconductors"***.** Presentation made the 1st International Conference on Bismuth-Containing Semiconductor Compouns: Theory Simulation and Experiment, 14-16 July 2010, (Michigan)

[27] K. Alberi, J. Wu, W. Walukiewicz, K. M. Yu, O. D. Dubon, S. P. Watkins, C. X. Wang, X. Liu, Y. J. Cho, and J. Furdyna, *"Valence-band anti-crossing in mismatched II-V semiconductor alloys"* Physical Review B, Vol. 75, Issue 4, (2007)

[28] S. J. Sweeney, Z. Batool, K. Hild, S. R. Jin and T.J.C. Hosea**,** *"The potential role of Bismide in future photonic devices"* **,** Transparent Optical Network (ICTON) 13th International Conference on. IEEE, (2011)

[29] F. R. Daniel, F. Bastiman, C. J. Hunter, D. L. Sales, A. M. Sanchez, J. P. R. David and D. Gonzalez, *"Bismuth incorporation and role of ordering in GaAsBi/GaAs structures",* Nanoscale Research Letters, Vol. 9, No. 1, (2014)

[30] S. Mazzucato, H. Lehec, H. Carrere, H. Makhloufi, A. Arnoult, C. Fontaine, T. Amand and X. Marie**,** *"Low temperature photoluminescence study of exciton recombination in bulk GaAsBi",* Nanoscale Research Letters, Vol. 9, No. 19, (2014)

[31] R. N. Kini, A. Mascarenhas, R. France, and A. J. Ptak, *"Low temperature photoluminescence from dilute bismides"* J. Appl. Phys. Vol. 104, 113534 (2008); doi: 10.1063/1.3041479

[32] C. J. Hunter, F. Bastiman, A. R. Mohmad, R. Richards, J. S. Ng, S. J. Sweeney and J. P.R. David, *"Optical and electrical properties of* $GaAs_{1-x}Bi_x/GaAs$ *diodes"* Presented at the 3rd International Workhop on Bismuth Containing Semiconductors, July 2012, (Victoria)

[33] J. Connolly, "Modelling and Optimising $GaAs/Al_xGa_{1-x}As$ multiple Quantum Well Solar Cells", PhD. Thesis, Imperial College of London, 1997

[34] A.J Ptak, D. J. Friedman, J. F. Geisz, S. R. Kurtz**,** *"Enhanced Depletion Width GaInNAs Solar Cells Grown by Molecular Beam Epitaxy***"** 31st IEEE Photovoltaic Conference, February 2005.

[35] N. Miyashita, Y. Shimizu, N. Kobayashi, Y. Okada and M. Yamaguchi, *"Fabrication of GaInNAs-based Solar Cells for application to Multi-junction Tandem Solar Cells"***,** Photovoltaic Energy Conversion, IEEE 4th on. Vol. 1, IEEE, (2006)

[36] Guido Haarpaintner , **"Electrical Properties of multiple quanrum wells", PhD thesis, Imperial College of London "**, 1995

[37] R Corkish and M. A Green, **"***Recombinations of carriers in quantum well solar cells*" in Proc. 23rd IEEE Photovoltaics Spec. Conf., New York, pp. 675-689, 1993

[38] N. G. Anderson, '*Ideal Theory of quantum well solar cells'*, J. Appl. Phys., Vol. 78, pp. 1850,1995.

[39] B. Royall, N. Balkan, S. Mazzucato, H Khalil, M. Hugues, and J.S. Roberts, *"Comparative study of GaAs and GaInNAs/GaAs multi-quantum well Solar Cells*" Phys. Status Solidi B Vol. 248, No 5, pp. 1191, (2011)

[40] Chin-yi Tsai, Chin-Yao Tsai: *"Effects of carrier escape and capture on quantum well solar cells, a theoretical investigation".* IET Optoelectron. Vol. 3, pp. 300-304, (2009)

[41] O. Kengradomying, S. Jiang, Q. Wang, N. Vogiatzis, and J.M Rorison**, "***Modelling escape and capture processes in GaInNAs quantum well solar cells***"**, Physic Status Solidi C, Vol. No. 4, pp. 585-588, (2013)

[42] S. M. Ramey and R. Khoie, *"Modelling of multilple quantum wells solar cells including capture, escape and recombination of photoexited carriers in quantum wells",* IEEE Trans. Electron Devices, Vol. 50, pp. 1179-1188, (2003)

[43] Yunpeng Wang, Yu Wen, Masakazu Sugiyama, and Yoshiaki Nakano, **"***A supperlattice Solar Cell With Enhanced Short-Circuit Current and Minimized Drop in Open-Circuit Voltage"***,** IEEE Journal of Photovoltaics, Vol. 2, No. 3, pp. 387-392, (2012)

[44] K.W Gossen**, "***Semiconductor device having shallow QW region",* U.S. Patent No. 5,210, 428, (1993)

[45] M Wagner, J. P. Leburton: *"Superlattices and multilayer structures for high efficiency solar cells"*. In *NASA, Lewis Research Center Space Photovoltaic Res and Technol.* pp. 103-109, (1985)

[46] C.D. Cress, S.J. Polly, S.M. Hubbard, R.P. Raffaelle, R.J. Walters*: "Demonstration of a n-i-p-i-diode photovoltaic", Prog. Photovolt Res Appl*. 2011, 19: 552

[47] M.A. Scolum, D.V. Forbes, J.S. Mc-Natt, S.M. Hubbard: *"Epitaxial regrowth contacts for the n-i-p-i photovoltaic device", IEEE Proc.* 2011, 978: 1914

[48] S Mazzucato, B Royall, R Ketlhwaafetse, N Balkan, J Salmi, M Guina, A Smith and R Gwilliam, *"Dilute nitride and GaAs nipi solar cells",* Nanoscale research letters, 2012, **7**:631

[49] M Weyers, M. Sato and H. Ando, "Red shift of photoluminescence and absorption in dilute GaAsN alloy layers", Japan. Journal of Applied Physics., Vol. 31, pp. L853 (1992.)

[50] Seoung-Hwan Park, "Optimization of the Structural Parameters in GaInNAs/GaAs Quantum-Well Lasers", Journal of the Korean Physical Society, Vol. 48, No. 3, pp. 480-483, (2006)

[51] D. J. Friedman, A. J. Ptak, S. R. Kurtz, J. F. Geisz, *"Analysis Of Depletion-Region Collection In GaInNAs Solar Cells"* 31st IEEE Photovoltaic Conference, February 2005

[52] David B. Jackrel, Seth R. Bank, Homan B. Yuen, Mark A. Wistey, and James S. Harris, Jr., "Dilute nitride GaInNAs and GaInNAsSb solar cells by molecular beam epitaxy," Journal of Applied Physics, Vol. 101, Issue 11, pp. 114916, (2007)

[53] Yunpeng Wang, Hassanet Sodabanlul, Shoa Jun Mal, Hirosama Fujiil, Kentaroh Watababel, Masakazu Sugiyama and Yoshiaki Nakano, "*A multi-step superlattice solar cell with enhanced sub-band absorption and open circuit voltage*". Photovoltaic Specialists Conference (PVSC), 2012 38th IEEE.

[54] Gopti Vijaya, Akhil Mehrotra, Andenet Alemu and Alexandre Freudlich**,** *"Multi-junction solar cell with Dilute Nitride Cascaded Quantum Wells Design"* Photovoltaic Specialist Conference (PVSC), 2012 38th IEEE.

[55] A. Ptak, "*Incoporation and properties of GaAsBi grown by molecular-beam epitaxy",* Presentation made the 1st International Conference on Bismuth-Containing Semiconductor Compouns: Theory Simulation and Experiment, 14-16 July 2010, (Michigan)

[56] G. Pettinar, A. Polimeni, J. H. Blokland, R. Trotta, P.C.M. Christianen, m. Capizzi, J.C. Maan, X. Lu, E.C. Young, and T. Tiedje*, "Unusual compositional dependence of the exciton reduced mass in GaAs1-xBix (x=0-10%)*", Presentation made the 1st International

Conference on Bismuth-Containing Semiconductor Compouns: Theory Simulation and Experiment, 14-16 July 2010, (Michigan)

[57] M. Meusel, F. Dimroth, C. Bauri, G. Siefer, A.W. Bett, K. Volz-Koch, W. Stolz, G. Stobl, C. Signorini, G. Hey**,** *"European roadmap for the development of III-V multi-junction space solar cells"***,** Presented at the 19th European Photovoltaic Solar Energy Conference, 7-11 June 2004, (Paris)

3 Experimental Techniques

3.1 Device growth

Most of the devices studied in this work were grown by epitaxial technology with majority of the devices grown by Molecular Beam Epitaxy (MBE) and a few by Metal-Organic Vapour Phase Epitaxy (MOVPE). Epitaxial growth is the deposition of uniform layers of materials on a substrate [1]. MBE is an ultra-high vacuum (UHV) ($<10^{-10}$ Torr) deposition process, in which constituents elements of semiconductors are deposited in the form of 'molecular beams' onto heated crystalline substrates. The UHV increases the mean-free path of the free atoms enabling a beam like motion of the atoms with infrequent collisions. To achieve UHV condition, a high capacity cryopump and liquid nitrogen cooled cryo-shrouds are used. The cryo-shrouds between the effusion cells eliminate thermal cross-talk between cells and also serve as impurity trap. The MBE growth technique allows precise control of layer thickness, composition and doping, and very thin layers with abrupt interfaces on the atomic scale, can be grown [2]. The schematic of an MBE system is shown in figure 3.1. The major components are: the reaction, preparation and occasionally a buffer chamber. The preparation chamber is where degassing is done and wafers stored ready for the epitaxial growth. The buffer chamber helps maintain vacuum during change or loading of wafers. Within the reaction chamber there are; beam generators and beam monitors, beam shutters, heated substrate holder and temperature sensors. The most common method of generating the molecular beams is heating the constituents using Knudsen cells (effusion cells) until they gain enough kinetic energy to effuse from the orifices into the chamber by thermo-ionic emission. The effusion cells are mounted onto the reaction chamber with the openings facing the substrate holder. Computer controlled mechanical shutters are used to allow the emission of different species of atoms to be directed at the substrate. The substrate holder is heated and also rotated to enhance uniformity of layer thickness, alloy composition and doping across

the wafer. The substrate temperature or growth temperature is an important growth parameter that determines the quality of the wafer [3]. Thermocouple and a pyrometer are both used to measure the growth temperature. On the opposite sides of the system is usually mounted the Reflective High Energy Electron Diffraction (RHEED) gun and an observation screen.

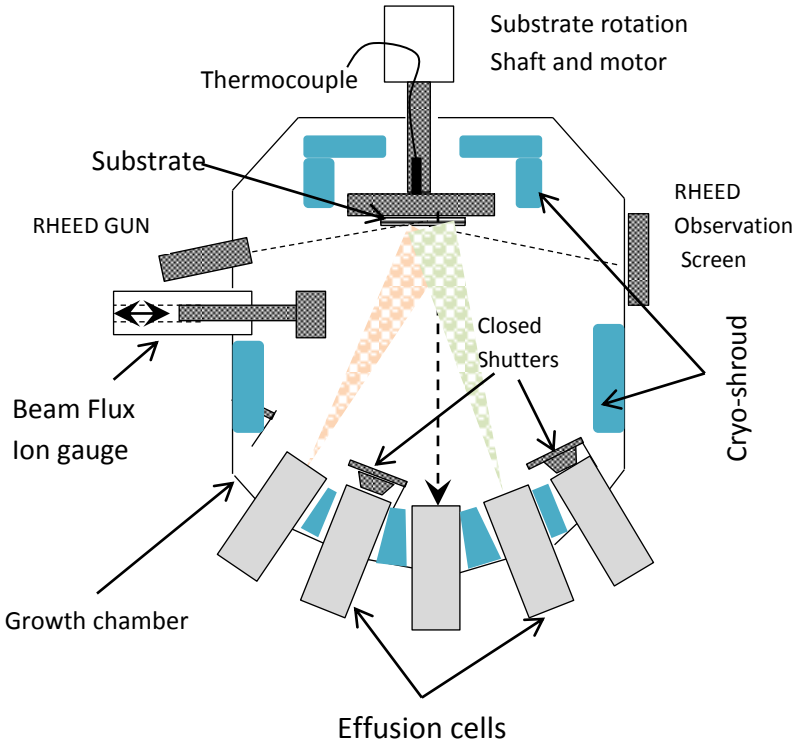

Figure 3.1: MBE system schematic.

The other advantage of MBE over other epitaxial techniques is enabling the in-situ monitoring of growth process using the RHEED signals. A high energy (5-50 keV) electron beam from the RHEED gun is sent inside the reaction chamber towards the sample, striking the surface at a glancing angle such that it penetrates one atomic layer, and the reflected beam is directed onto the fluorescent screen. Figure 3.2 shows how the RHEED oscillations form during growth of each monolayer. When a complete layer has grown the reflection of electron to the screen is maximum resulting in the maximum RHEED signal. As a new layer

begins to grow islands form and some electrons are scattered and fewer are reflected onto the screen. The minimum RHEED signal corresponds to half-grown layer when more islands have formed resulting in highest electron scattering. Finally as the layer becomes more complete the wafer surface become smoother and scattering reduces until a maximum reflection resulting in maximum RHEED signal occurs again. This process results in the oscillation of RHEED pattern intensity, and the period of oscillation indicates the growth of a single monolayer.

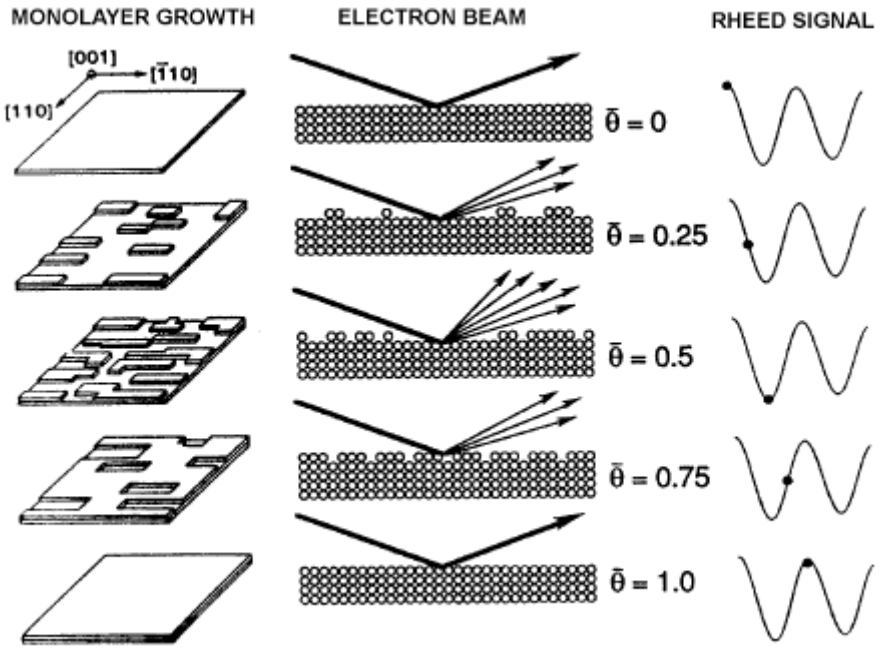

Figure 3.2: Schematic diagram of illustrating the mechanism behind the RHEED showing the RHEED signal as a function of $\bar{\theta}$ (fractional layer coverage) [4]

Besides determining the growth rate information such as surface morphology can be deduced from RHEED signal. Parallel streaks on the screen indicate a smooth growth, and a spotty pattern implies rough growth (alloy clustering or formation of quantum dots), as illustrated on figure 3.3.

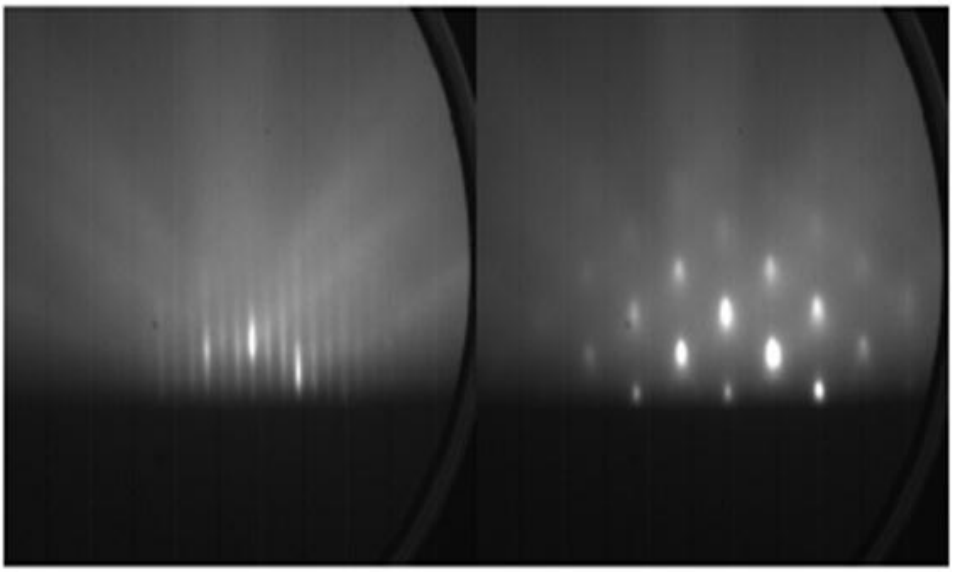

(a) (b)

Figure 3.3: The RHEED patterns showing (a) smooth growth, (b) rough growth [3].

A photograph of a Riber Compact21 MBE system at Chalmers University of Technology used in growing some of the devices studied in this work is shown in figure 3.4.

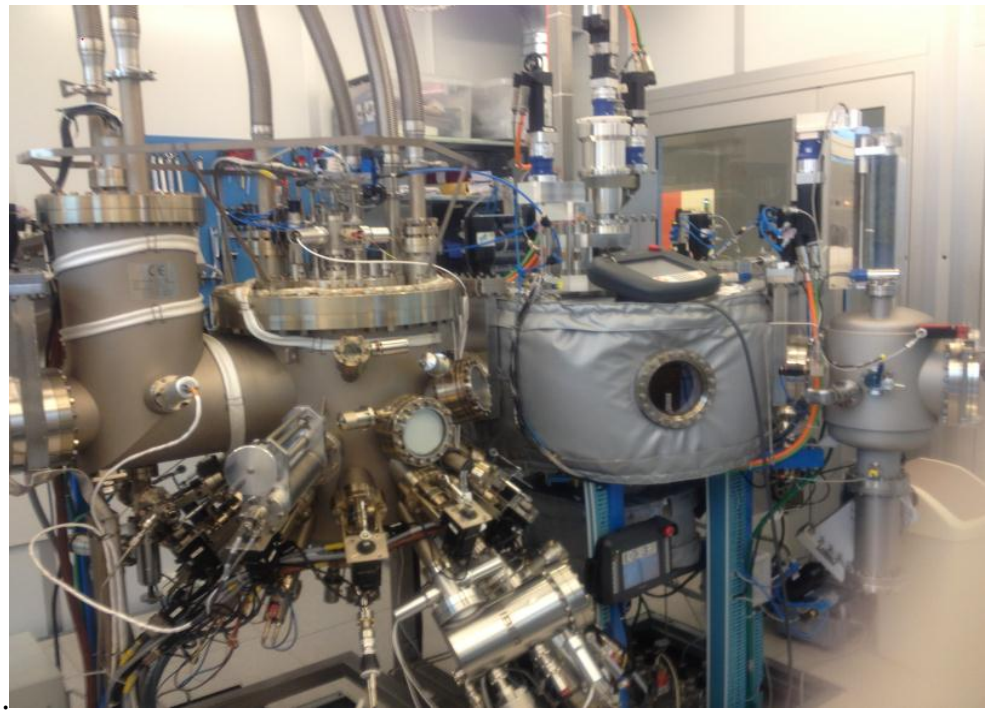

Figure 3.4: A photograph of a Riber Compact21 MBE system at Chalmers University of Technology used in growth of $GaAs/GaAs_{1-x}Bi_x$ devices in this work.

The details of the Molecular MOVPE growth process can be found in references, [1] and [5].

3.2 Fabrication

Majority of the devices studied in this work came as wafers from the growers and had to be fabricated into structures suitable for each measurements performed, except for contactless measurements such as photoluminescence. The devices fabricated include the solar cells and high field bars.

The fabrication mainly involves formation of a structure and electrical contacts on the device wafer. In this work, Ohmic contacts were formed to offer a low resistance path for both types of carriers in and out of the devices. For an Ohmic contact to form a metal work function should be smaller than the semiconductor work function, for an n-type semiconductor, and the reverse holds for a p-type semiconductor, figure 3.5. To increase possibility of formation of Ohmic contacts, contact layers are often highly doped, the technique of which was deployed in this work. The tendency to form an Ohmic contact by a highly doped semiconductor is shown in figure 3.6, where $E_F, E_C, E_{vac}, \phi_M, \phi_S \; and \; \chi$, are the Fermi, conduction band and vacuum energy levels respectively and, metal work function, semiconductor work function and electron affinity respectively. In reality a semiconductor-metal junctions are not fully Ohmic. For a semiconductor-metal contact, the 'Ohmic' contact does not infer a linear I-V characteristic, but implies that the contact does not limit the current flow [6].

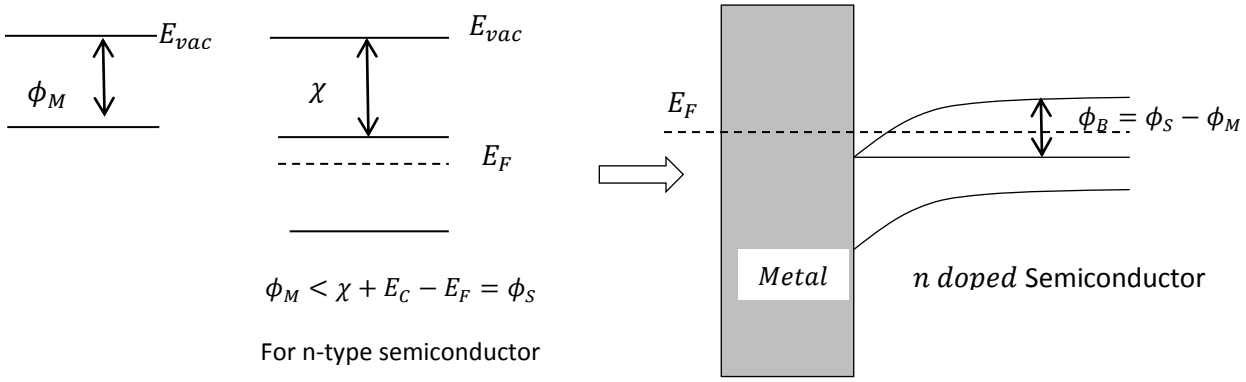

Figure 3.5: Formation of Ohmic contacts

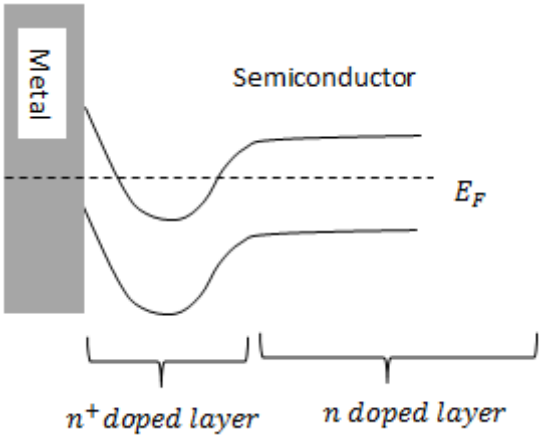

Figure 3.6: Formation of Ohmic contact by high doping

The Fabrication process involves four major steps illustrated by figures 3.7 (a) to 3.7 (f).

- Preparation and Cleaning: Wafer resizing and removal of surface dirt and oxides.
- Photolithography: Imprinting a pattern of a device onto the wafer using photosensitive chemical, 'photo-resist', photo-masks using ultra violet (UV) light.
- Formation of metal contacts (metallization): Metal contacts are evaporated onto the devices under UHV conditions.
- Isolation etches: Physical formation of the structure of the device using chemical (wet etchants) or dry etching (ion beams).

- **Preparation and cleaning**

The wafer is cut into the desired size and shape using a scriber. The cut piece is mounted on a glass holder using a thin even layer of crystal bonder. This is then followed by washing the chips with acetone to remove non-chemically bond dirt or debris. The device piece is then examined under the microscope for any evidence of dirt spots. If some dirt spot are observed then it requires gently wiping with a swab and rewashing.

Immediately after growth most wafers will start developing an oxide layer. Unlike the dirt washed by acetone, oxides are chemical layers and have high resistance to flow of electric current. The effect of unremoved oxide is increasing of the metallic contact resistance typically into the 10^3-10^6 Ω range, resulting in a poor fill factor for the device. The device piece is therefore washed with ammonia solution 1:10 = NH_3: de-ionised (DI) water, for ~ 15 seconds and immediately rinsed with DI water. The process is repeated about 3 times to ensure complete removal of the oxide layer. Alternatively 1:3, HCl: H_2O warmed solution can be used instead of Ammonia.

- **Photolithography**

Photolithography involves two major processes; (i) Application of photo-resist (spin coating), (ii) Exposure and Development

(i) Spin coating: The device is placed on the spin coater and covered with a small amount of PBRS 150 positive photoresist. After all bubbles have escaped the solution, the spin coater is spun at ~4000 rpm for 30 seconds, which results in the formation of a uniform layer of ~1µm photoresist.

The device is then soft baked for 10 sec at 90 °C to activate the photoresist.

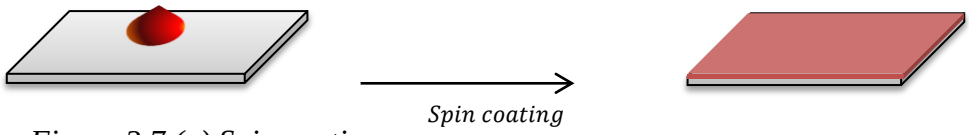

Figure 3.7 (a) Spin coating

(ii) Exposure: The device is loaded onto the mask aligner and a desired pattern on the mask is aligned with the device, and then lowering the mask too close to the device to avoid light from straying to unwanted regions of the device. UV light is then switched for 10-20 seconds chemically changing the photo-resist on the exposed parts of the device.

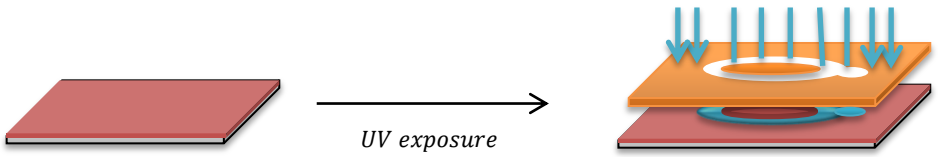

Figure: 3.7 (b) Ultra-violet exposure.

(iii) Development: The device is immersed into a sodium hydroxide bath at ratio of 1:10 of NaOH: H_2O, until a pattern appears on the device. The device is removed, washed with DI water and blown dry with zero grade nitrogen.

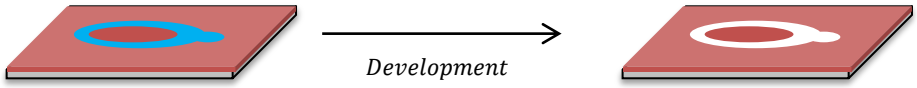

Figure 3.7(c): Development

❖ **Contact formation (Metallisation)**

The device is re-washed with ammonia, followed by DI water, blown dry with zero grade nitrogen and immediately loaded onto the evaporator ready with metals to be evaporated. In all devices either the Au/AuGe/Ni/Au (on n-type semiconductor) or Au/ZnAu/Au (on p-type

semiconductor) or TiAu metal systems were evaporated onto the semiconductor under a high vacuum using the Edwards Vacuum Coating Unit E306A.

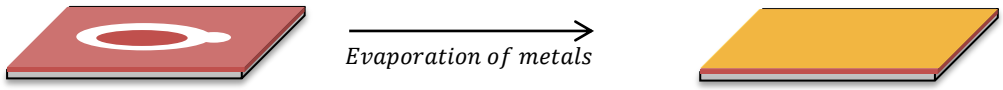

Figure 3.7 (d): Evaporation

After the system has cooled down (~2hrs), the devices are removed and placed in acetone bath. The areas with photoresist underneath are lifted off and the remaining metallic areas form the contacts.

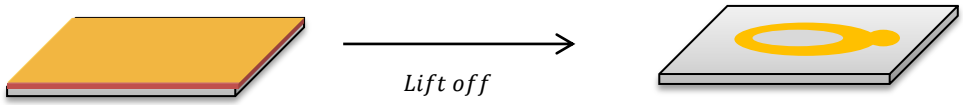

Figure 3.7 (e): Lift-off

❖ **Etching or device isolation**

The photolithography process is repeated, this time using the negative of the mask. This ensures the device areas are protected and the other areas will be exposed to UV light. The device is hard baked at 150 °C for 5 minutes. The surface of the device is scanned with a surface profiler to establish a reference level for an isolation etching. The device is then placed into an etchant mixture, 1:8:80 = H_2SO_4: H_2O_2:H_2O, with a typical etch rate of 0.5 µm/minute for GaAs based materials. After etching desired depth, the profiling is done for confirmation and extra etching may performed depending on the outcome. The device is washed with acetone to remove the photoresist layer, and later DI water. For Au/AuGe/Ni/Au and Au/ZnAu/Au annealing is required to diffuse the metals and harden the contact. Care must be taken with P-type annealing done on shallow junctions, as the Zn can migrate deeper into the junction. The devices were packaged by mounting on either ceramic or thin copper blocks as well as wire bonding to more robust contacts.

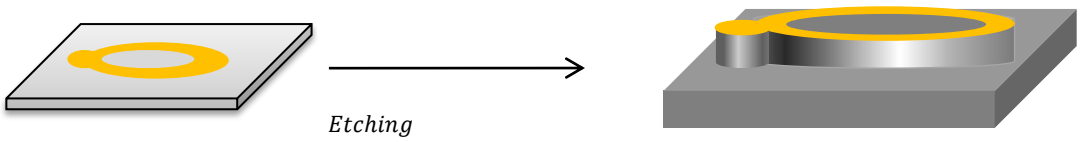

Figure 3.7 (f): Device isolation (etched depth exaggerated to show device structure)

3.3 Photoluminescence (PL)

Photoluminescence is a handy technique used to obtain a wealth of information on optical properties of a semiconductor material or device. It is a non-intrusive technique in which the material under test is excited by a light source (often a laser) of energy greater than the band gap of the material, generating electron hole pairs in the process. The excited carriers relax to their lowest energy states and subsequently recombine through different path ways available, which may include, radiative recombination with emission of photons and or different non-radiative paths often resulting in emission of heat energy into the material, the former resulting in the PL spectrum. Some possible recombination processes are shown in the figure 3.8. A PL spectrum can compose of one or more of processes (a) to (e) (radiative recombination processes). The most common transition is the band (bottom of conduction band) to band (top of valence band), which has the energy equivalent to the band-gap of the material. The primary purpose of PL is to determine the band-gap of the material.

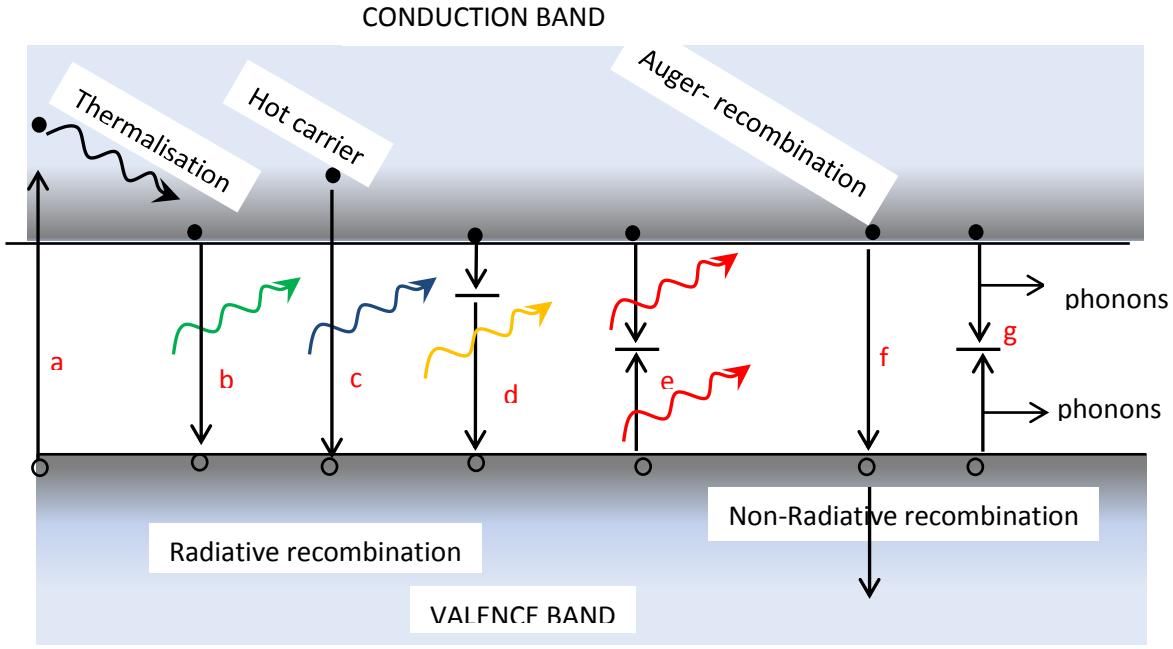

Figure 3.8: (a) Excitation (b) Band to band, (c) Hot carrier, (d) conduction band trap to valance band, (e) recombination centre radiative recombination, (f) Auger recombination, (g) non-radiative recombination via traps.

Figure 3.9 shows a schematic of the PL set up used in Essex University Optoelectronic laboratory to perform measurements on the samples. The samples were mounted on the liquid bath cryostats; Oxford Instruments Variox cryostat with a temperature range of 8 K-300K or a custom made cryostat with a temperature range of 77 K-300 K. A 480 nm Argon laser or 660 nm diode module lasers were used as excitation sources depending on sample measured. The PL emission from the sample was focused onto a Bentham M300 monochromator. Long pass filters of 630 nm and 760 nm are placed at the entrance of the monochromator, for 480 nm and 660 nm lasers respectively. The filters cut out the laser reflection, which can damage the photomultiplier (PMT) tubes, and or give a false signal. To further reduce the possibility of laser interference, the sample angle is slightly re-adjusted, to just shift the reflected laser spot from the monochromator entrance. The spectrally resolved PL is picked from the output of the monochromator with a sensitive photodetector. A Hamamatsu In/InGaAs

photomultiplier tube, with a nearly flat response in the range of 900 nm to 1600 nm was used to amplify the signal. The lock-in-phase technique was used to measure the output signal from the PMT, therefore the laser beam incident on the sample was modulated by a mechanical chopper, before being fed into a Stanford research system SR830 lock-in-phase amplifier. The measurements were automatically recorded in a PC via a GPIB connector.

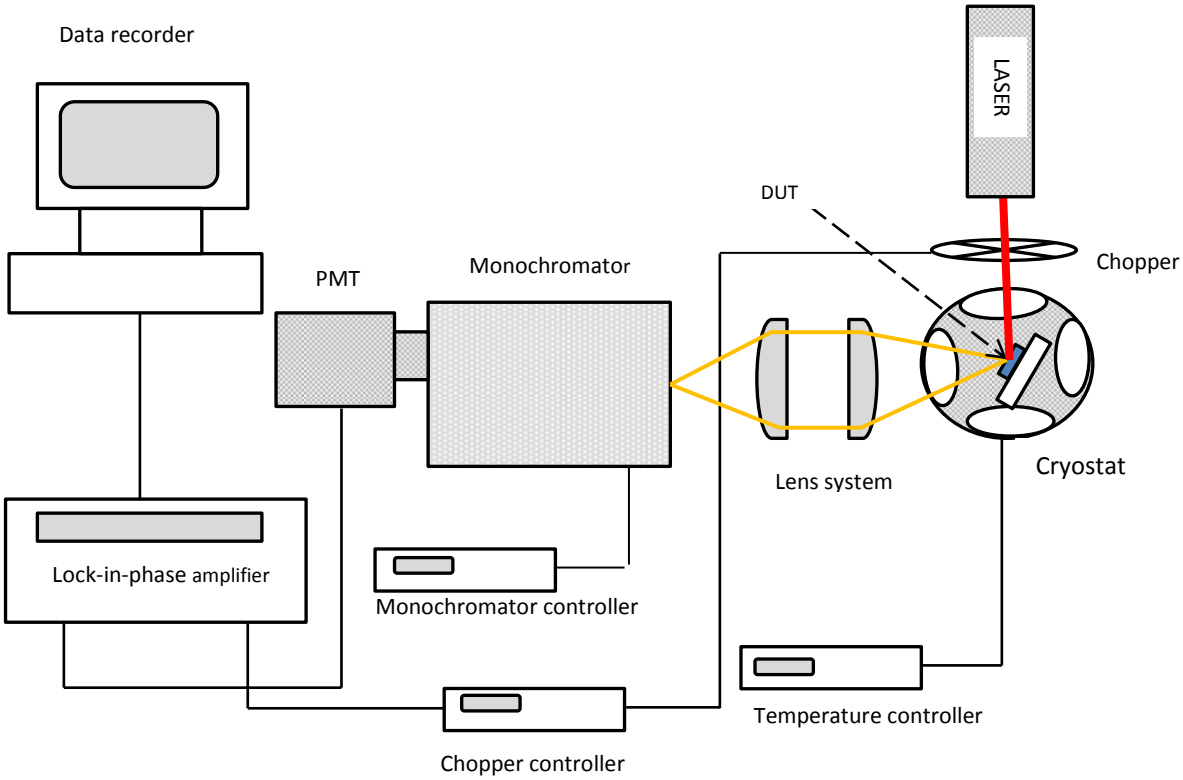

Figure 3.9: The PL set-up used in optical characterisation of the samples

3.4 I-V Measurements

3.4.1 Dark I-V characterisation

Dark I-V characterisation is a precursor to the performance of a solar cell under illumination. A wealth of information on the quality of the junction can be obtained from the dark I-V. Most importantly the amount of leakage current across the junction, which is influenced by the recombination currents and the shunt resistance, and set an upper limit on V_{oc}, generated

by the device. Analysis of the dark current density plots show the amount of dark current density generated by the device as well as revealing the nature of the dominant dark current density component. The resistance across the junction (shunt resistance) as well as the resistance along the junction (series resistance), can also be estimated from the dark current density plots, using various numerical techniques available. In this work the diffusion and recombination dark currents had been estimated using the Shockely ideal diode equation to probe the V_{oc}, of the devices comparatively. The contacts also must be tested for Ohmic behaviour; The effect of poor contacts can range from completely blocking to the flow of current to limiting the current which can result in incorrect measurements. An I-V scan was done between -1 V to +1 V to see the contact behaviour especially in the forward biased direction. The set-up used for dark I-V characterisation is the same as that light I-V characterisation (figure 3.11), explained in the following section, except that the solar simulator will not be used.

3.4.2 Light I-V characterisation

The light I-V characteristics of a solar cell are very important as they give the key figures of merit such as short-circuit current density (J_{sc}), open circuit voltage (V_{oc}), fill factor (FF), which are used to determine the efficiency of the cell under different operation conditions. For terrestrial devices like the ones tested in this work, AM1.5G characterisation is the ideal choice. It is a challenge to reproduce an AM1.5G spectrum for testing solar cells. However a standard which serves as a reference spectrum (ASTM-G173-03 global) normalised to give a total irradiance of 1000 W/m^2 has been developed for calibration of various simulators used. Reference detectors are tested under this conventional standard spectrum, with and spectral mismatch factor determined for each. These can later be used to calibrate any simulator for AM1.5G conditions. The set-up for room temperature I-V characterisation in the Essex

Optoelectronic Laboratory is shown in figure 3.11. The same set-up was used for low temperature characterisation with the device mounted inside a cryostat. Newport 96000 150 W Xenon arc lamp was used with an AM1.5G filter was installed was used to simulate the AM1.5G spectrum. Figure 3.10 shows the AM1.5G, the simulator and AM1.5G filter spectrums.

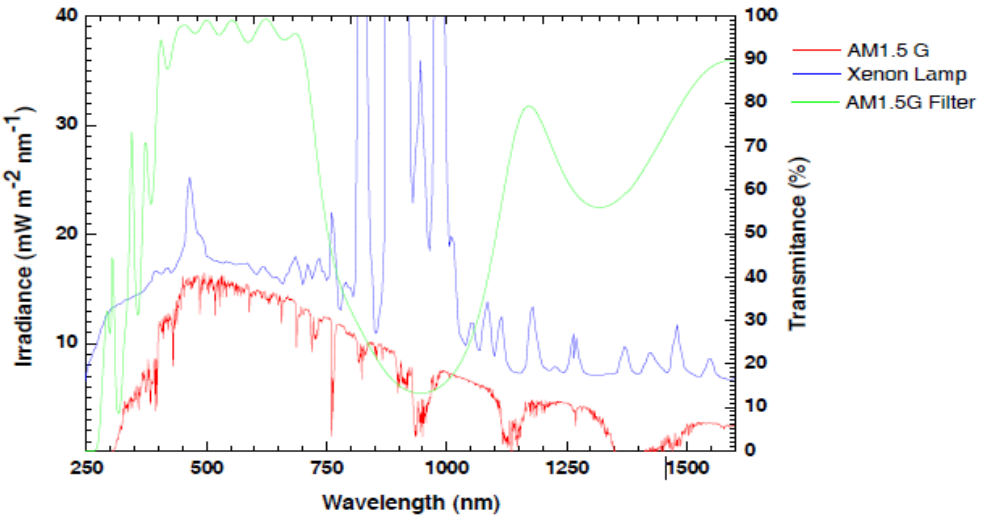

Figure 3.10: The AM1.5G (red), Xenon lamp (blue) and AM1.5G filter (green) spectrums [4].

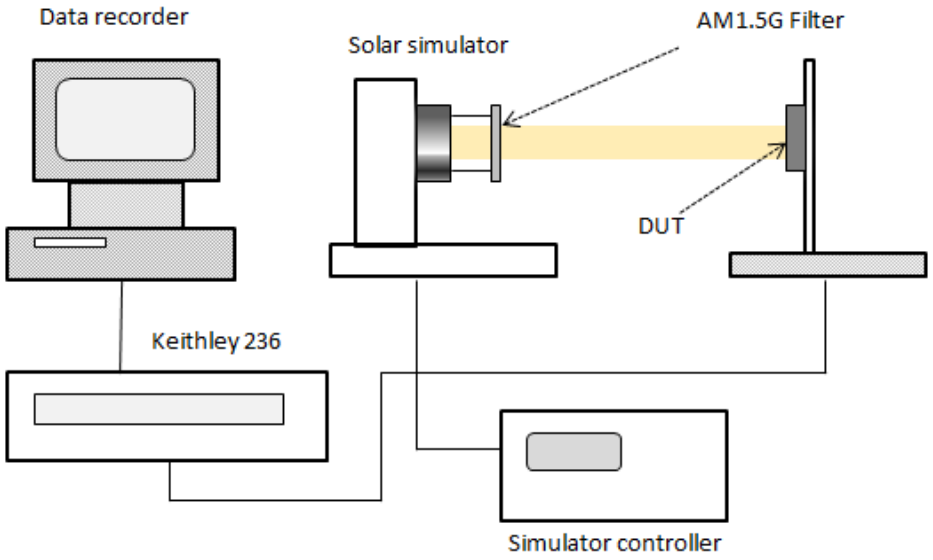

Figure 3.11: The experimental setup for measuring the I-V characteristiccor of solar cells.

The solar cells under test were mounted on a custom made probe station, shown in figure 3.12. The probe station major components are; the copper block that serves as back contact as well as a heat sink. Beneath the copper block is a Peltier cooler controlled by an ILX Lightwave LDC-3724B laser diode controller to keep the temperature of the block and cell almost constant. A thermistor bead embedded in the copper blocks gives temperature feedback to the controller.

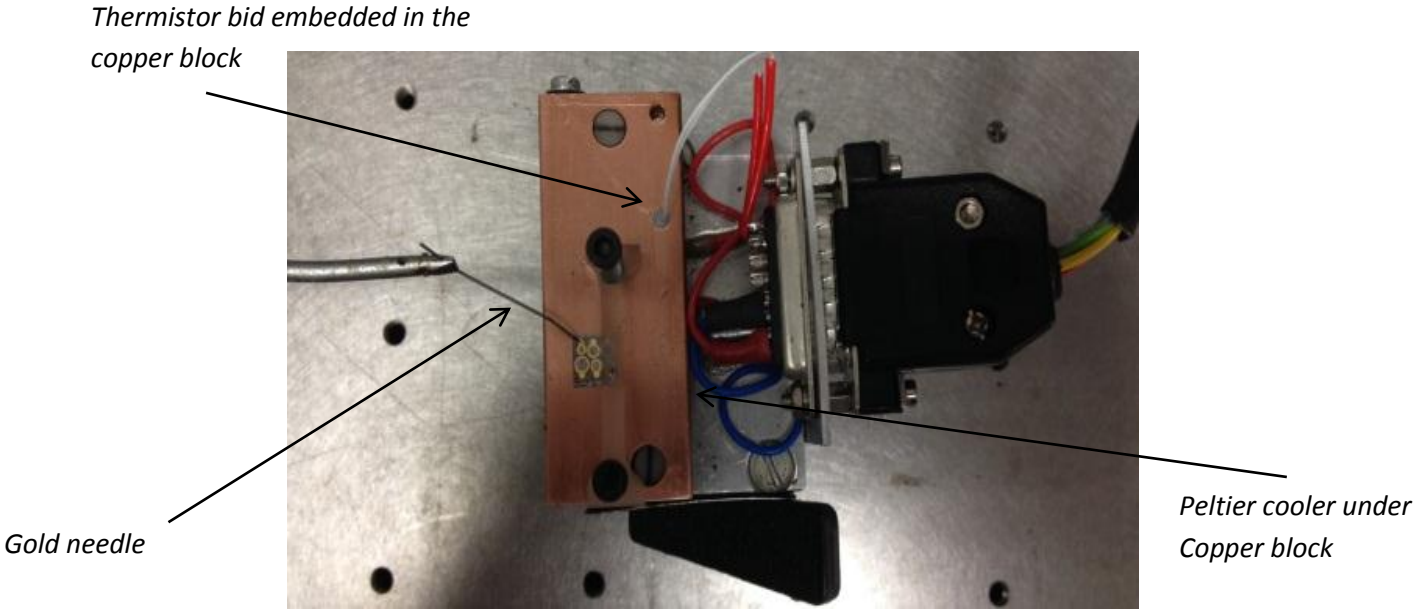

Figure 3.12: The solar cell probe station used

The input power on the devices was measured with a 340 Trisolsolar power meter using a calibrated silicon reference cell (1413_VLSI reference cell). A Keithley 236 kit was used in the source voltage-measure current mode to ramp a voltage signal over a chosen range of voltages on the device, at the same time measuring the current produced by the device. The results were automatically stored on a PC via GPIB.

3.4.3 Spectral response

The spectral response of the photocurrent is a deeper analysis of the generation of photocurrent by the device. In I-V characterisation, the measurement of short-circuit current was done using a broadband illumination which gives a global short circuit current value. The spectral technique uses dispersed light to determine the short circuit current generated at each wavelength (practically a narrow band). Since different light wavelengths are absorbed at different depths of the device, the spectral response techniques have the ability of depth resolution of device's performance. In this work a Bentham M300 monochromatic with a resolution capability of less than <0.1 nm [7] was used, to disperse the quartz halogen lamp with a spectral range of 350 nm to 2.5 µm. Because of the low power of dispersed light, the photocurrent was measured with a lock-in-phase amplifier (Stanford Research Systems SR30 Lock-In Amplifier) technique to illuminate noise from the background light. The set-up used is shown in figure 3.13. The device under test can be mounted inside the cryostat if temperature dependent measurements were performed. The data is recorded in a PC via a GPIB connector.

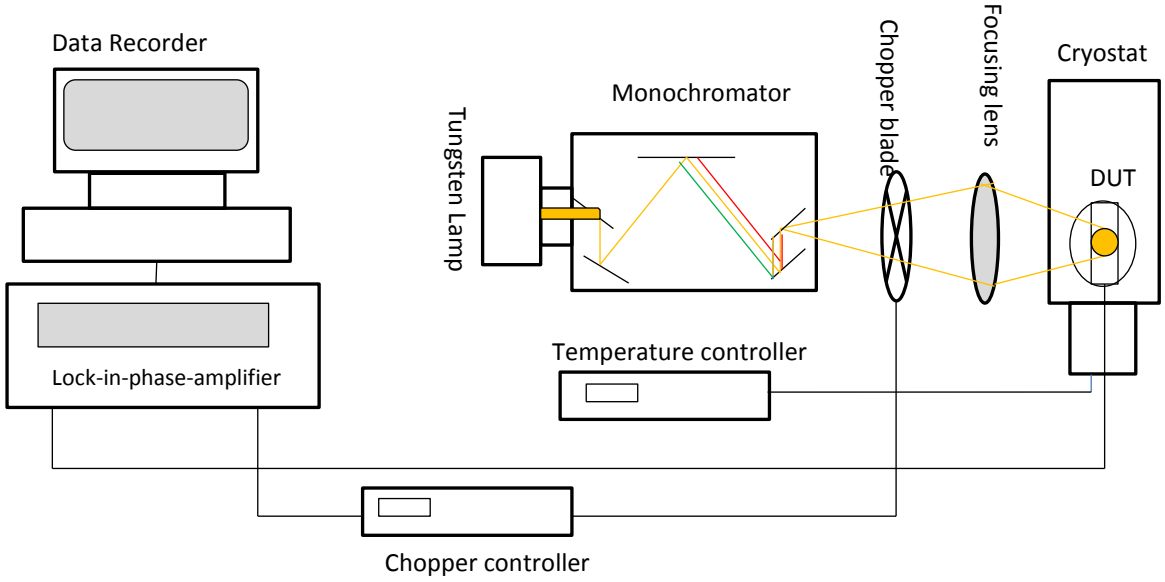

Figure 3.13: The spectral characterisation set-up used in Essex Optoelectronic laboratory.

There spectral short circuit current can be determined using one of the methods in figure 3.14. A collimated beam can be used to illuminate an area greater than the device area, as well as a reference detector used. The areas of the devices are later used in normalisation. Alternatively the light can be focused to fall entirely within the device area, in this case only the incident power for such light is needed. The former method was used in this work.

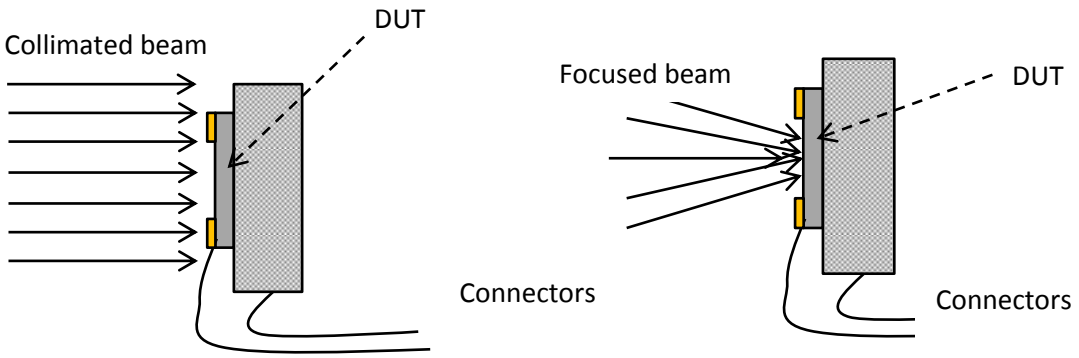

(a) (b)

Figure 3.14: Methods for measuring spectral response of the short circuit current; (a) a collimated beam covering an area greater than the device area, (b) light focused to fully fall within the device area.

3.5 Photoconductivity

Photoconductivity is the process whereby mobile carriers are created by absorption of incident radiation. Both steady state photoconductivity (SSPC) and transient photoconductivity (TPC) measurements on the devices were performed using the set- up represented by diagram 3.15.

The photoconductivity (PC) technique investigates the behaviour of an electrical conductivity of a semiconductor with different excitation energies.

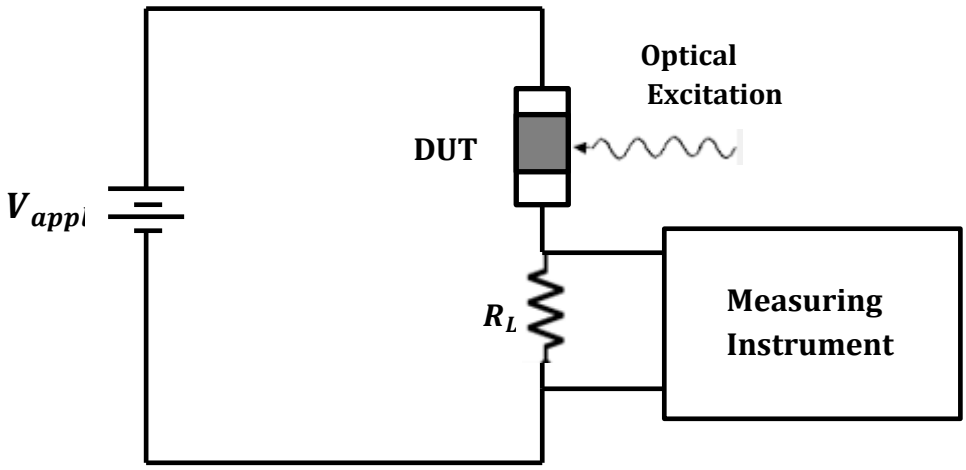

Figure 3.15: Photo conductivity set up used to study SSPC and TPC.

The total photoconductivity in a semiconductor material is the sum of photoconductivity under illumination, $\Delta\sigma_{PC}$ and the σ_0 electrical conductivity of the material in darkness.

$$\sigma = \sigma_0 + \Delta\sigma_{PC} \tag{1}$$

For materials with high resistivity the dark conductivity is negligible compared to the photoconductivity under illumination, $\sigma \approx \sigma_{PC}$. High field devices were fabricated from $GaAs_{1-x}Bi_x$ bulk sample at 1.8 % Bismuth concentration. Due to the undoped capped layers of the devices very high resistance (1.2 MΩ), contact formed. Given that condition the dark conductivity was assumed negligible.

Modulated photoconductivity measurements were made on the samples by chopping a He-Neon laser source of 660 nm at a frequency low enough to observe carrier decay dynamics. The spectral photo-conductivities of the devices were measured by mounting the device into the cryostat, by extending the connectors. Excitation power dependency measurements were made using the same set-up and measurements taken for different laser intensities.

In transient photoconductivity some crucial changes are; the optical excitation should be of very narrow width with very low frequency. The Q-switched, mode locked Nd:YAG laser emitting at 1064 nm and with and an option to tune to 533 nm was used. The lasers pulses are of 100 picoseconds width with 5 Hz repetition rate. The capacitive impedance of the circuit must be low enough not to mask the decay of the signal. Therefore high speed cables were used and the circuit path made as short as possible to reduce both resistive and capacitive impedances.

_____

References

[1] R. Potter, "*Optical processes in dilute nitrides*" PhD. Thesis, University of Essex," (2003).

[2] J. R. Arthur, "Molecular beam epitaxy", Surface science, Vol 500, pp. 189-217, (2002).

[3] Y. Song, "**Novel Materials and Technologies for IR Optoelectronic Applications**", PhD. thesis, Chalmers University of Technology, (2012)

[4] A. M. R. Godenir, "**Novel Dilute nitride Semiconductor Materials for Mid-Infrared Applications**", PhD. Thesis, University of Lancaster (2008)

[5] B. Royal, "*GaInNAs/GaAs multiple quantum well solar cells*", PhD. Thesis, University of Essex, (2011)

[6] S.O. Kasap; "**Electronic Materials and Devices**", 3rd Edition, Mc Graw-Hill, (2006)

[7] Bentham.co.uk, "M300 Monochromator" [Online], [available at; http://www.bentham.co.uk/m300.htm, [Accessed on 19 December 2014],

4 Dilute nitride solar cell results

4.1 Introduction

4.1.1 Effect of temperature on efficiency

The temperature effects on the performance of a solar cell have always been a subject of interest, given that solar cells are often operating at temperatures that differ from the room temperature, which is commonly assumed in many designs. Temperature effects can be complex as it comes through a number of parameters that are also related, making it hard to decouple the effects on the parameters from one another. However the degree of the importance of each parameter can be derived from theoretical models of temperature dependency. The most important parameter of any solar cell is its efficiency, which depends on many other parameters.

Theoretically the net effect of increasing temperature of any solar cell device is the reduction of efficiency [1]. This is based on effect of temperature on a semiconductor material. When the temperature of a semiconductor increases the band-gap reduces. In a solar cell which is a p-n junction, as the temperature increases the photogenerated current (J_L) increases due to additional absorption at lower end of spectrum as the bandgap reduces. Reduction of bandgap results in lower built-in voltage which places an upper limit on the open circuit voltage(V_{oc}). Secondly as the temperature increases the equilibrium population of carriers increases exponentially. The effect of the latter in a solar cell is increasing the dark current, which has a twofold effect; reduction of V_{oc} due reduction of short circuit current density (J_{sc}) due to increased recombination current. As a result the loss in (V_{oc}) outweighs any gain in (J_{sc}), resulting in efficiency loss as temperature increases.

The ultimate efficiency of a solar cell device depends on the ability to collect the photogenerated carriers (quantum efficiency). The quantum efficiency (QE) of any solar cell depends on the diffusion length (L) as in equation 4.1

$$QE(\lambda) = \alpha L/(1+\alpha L) * \exp(-\alpha W_d) + [1 - \exp(-\alpha W_d)] \quad (4.1)$$

Diffusion length is related to temperature of the material as in equation 4.2

$$L = \sqrt{kT\mu/q\tau} \quad (4.2)$$

These relations suggest diffusion length is directly proportional to square root of temperature ($T^{\frac{1}{2}}$) which is generally a weak dependence. Mobility (μ) also has temperature dependency from lattice vibration point of view. Mobility dependency of temperature is dominated by lattice scattering at elevated temperatures and impurity scattering at lower temperatures. The approximate temperature dependencies are $T^{\frac{-3}{2}}$ for lattice scattering and $T^{\frac{3}{2}}$ for impurity scattering [2]. The resultant effect on the diffusion coefficient is $T^{\frac{3}{4}}$ which still a relatively weak dependence. Experimental results [3] show that the temperature dependency of mobility over temperature ranges similar to typical ranges in this work (100 K-300 K) , are very small which justifies be assumption that the temperature effects on diffusion length are relatively small and can be ignored.

The temperature effect on the carrier lifetime (τ) which is directly proportional to diffusion length can also be assumed negligible for the temperature ranges (100 K-300 K) over which the study was conducted, due to negligible changes observed in carrier mobility.

4.1.2 Effect of temperature on solar cell dark current.

The temperature dependency of the intrinsic carrier (n_i) concentration varies as in equation 4.3 and 4.4

$$n_i(T) = 2\left(\frac{2\pi kT}{h^2}\right)^{\frac{3}{2}}(m_e^* m_h^*)^{\frac{3}{4}} exp\left(\frac{-E_{G0}}{2kT}\right) = BT^{\frac{3}{2}}\exp(\frac{-E_{G0}}{2kT}) \tag{4.3}$$

$$n_i{}^2(T) = 4\left(\frac{2\pi kT}{h^2}\right)^{3}(m_e^* m_h^*)^{\frac{3}{2}} exp\left(\frac{-E_{G0}}{kT}\right) = BT^{3}\exp(\frac{-E_{G0}}{kT}) \tag{4.4}$$

where T is the temperature, m_e^* is the effective mass of electron, m_h^* is effective mass of the hole, E_{G0} is the band-gap linearly extrapolated to zero and B is a constant which is essentially independent of temperature.

These relations suggest that both the ideal and recombination dominated diode dark currents have strong temperature dependency; T^3 and $T^{\frac{3}{2}}$ respectively.

For the ideal (Shockley) case, the dark current in a p-n junction varies with applied voltage as shown in equation (4.5).

$$J = n_i{}^2\left[q\frac{D_n n_i^2}{L_n N_a} + q\frac{D_p n_i^2}{L_p N_d}\right]\left(\exp\left(\frac{qV}{kT}\right) - 1\right) \tag{4.5}$$

where all symbol have their usual meaning.

Substituting $n_i{}^2$ expression from equation 4.4 yields,

$$J = AT^3\exp(\frac{-E_{G0}}{kT})\left(\exp\left(\frac{qV}{kT}\right) - 1\right) \tag{4.6}$$

where A is a constant. A similar expression can be derived for non-ideal case.

A more generalised expression for temperature dependency of dark current in a p-n junction diode is derived from a generalised diode equation;

$$J = J_0\left(\exp\left(\frac{qV}{mkT}\right) - 1\right) \tag{4.7}$$

$$\text{where } J_0 = A'T^{\gamma}\exp(\frac{-E_{G0}}{mkT}) \tag{4.8}$$

where A' is a material dependent constant, m is the ideality factor and γ is a constant that varies between 1-4 to include possible dependencies on other parameters [4].

4.1.3 Effect of temperature on solar cell open circuit voltage.

The open circuit voltage of a diode V_{0c} is approximated by equation 4.11, derived from relations 4.8 to 4.9.

$$V_{0c} = \frac{kT}{q}\ln\left(\frac{J_{sc}}{J_0}\right) \tag{4.9}$$

where J_{sc} is the short circuit current.

Substituting the expression for J_0 in equation 4.8 into 4.9 yields;

$$V_{0c} = \frac{kT}{q}(\ln J_{sc} - \ln B' - \gamma\ln\mathrm{T} + \frac{qV_{G0}}{kT}) \tag{4.10}$$

Assuming $\frac{dV_{G0}}{dT}$ does not depend on $\frac{dJ_{sc}}{dT}$,

$$\frac{dV_{oc}}{dT} = \frac{V_{0c} - V_{G0}}{T} - \gamma\frac{k}{q} \tag{4.11}$$

Equation 4.11 shows that the temperature sensitivity of the V_{0c} of a solar cell depends on the bandgap. A solar cell with a small bandgap has strong temperature sensitivity of V_{0c} than the one with a larger bandgap.

4.1.4 Effect of radiation levels on the solar cells.

At elevated radiation levels, under low injection recombination rates are linear and the superposition of currents is applicable [1]. When incident flux is increased by factor X, the photo-generated current is expected to increase by approximately;

$$J_{conc} = XJ_{sc} \tag{4.12}$$

and

$$V_{oc}(X) = \frac{mk_BT}{q} ln\left(\frac{XJ_{sc}}{J_0} + 1\right) \approx V_{oc}(1) + \frac{mk_BT}{q} lnX \tag{4.13}$$

where J_{sc} is the shortcut current density at 1 sun concentration.

These analytical expressions reveal that in a single p-n junction solar cell the short circuit current is expected to increase linearly with intensity of light while voltage increases logarithmically and saturates as it approaches the built-in potential of the junction. In overall both increase in J_{sc} and V_{oc} will result in increase of efficiency with radiation. With non-conventional designs which may have several junctions and quantum confinement of carriers like the devices studied in this work n-i-p-i, MQWs, and p-i-n structures), there is a possibility of departure from the generalised expression in equations in 4.12 and 4.13.

As the design and dimension of the devices change from that of a single p-n junction to more complex structures such as n-i-p-i, MQWs and others, the temperature and radiation effects are not readily predictable as for a conventional p-n junction. In those cases experimental observations are invaluable in studying the temperature responsivity of the devices. This chapter is the presentation of the experimental observation on temperature and radiation responsivity of the non-conventional solar cell studied in this work.

4.2 The conventional GaAs solar cell (TS0419)

The structure of a GaAs p-n junction solar cell (TSO419) that served as a standard also referenced as the base design for the rest of the non-conventional devices (MQWs, p-i-n and n-i-p-i) is shown in figure 4.1.

Material	**Thickness (nm)**	**Doping (cm^{-2})**
n type GaAs	200	(Si) $2x10^{18}$
n type $Al_{0.8}GaAs_{0.2}As$	40	(Si) $2X10^{18}$
n type GaAs	200	(Si) $2X10^{18}$
P type GaAs	3000	(Be) $2X10^{17}$
p+ type GaAs	20	(Be) $2X10^{17}$
p+ Substrate		

Figure 4.1: The structure of the GaAs p-n unction solar cell (TSO419).

4.3 Dilute nitride p-i-n solar cells results

4.3.1 Device structures

The structures of the dilute nitride p-i-n solar cells studied are shown in figure 4.2. The first p-i-n, "pin1" solar cell is a GaAs/$Ga_{1-x}In_xN_yAs_{1-y}$ with a 600 nm, nominally undoped $Ga_{0.906}In_{0.094}N_{0.028}As_{0.972}$ intrinsic region. The second p-i-n, "pin2", is a GaAs/$Ga_{1-x}In_xN_yAs_{1-y}$ with a 900 nm, nominally undoped $Ga_{0.973}In_{0.027}N_{0.02}As_{0.098}$ intrinsic region. All the devices were grown by solid source MBE with RF plasma source for atomic nitrogen flux generation. "Pin2" had a SiO_2/SiN_x anti-reflection coating layer while pin1 had no anti-reflection coating, but was passivated by a 50 nm $Al_{0.3}GaAs$ layer.

Material	Thickness (nm)	Doping (cm^-3)
p+- GaAs	50.00	Na=5.0E18
p –$Al_{0.30}$GaAs	30.00	Na=2.0E18
p-GaAs	220.00	Na=2.0E18
UD-$Ga_{0.906}In_{0.094}N_{0.028}As_{0.972}$	600.00	None
n $Ga_{0.906}In_{0.094}N_{0.028}As_{0.972}$	400.00	Nd=1.0E17
n GaAs	500.00	Nd=2.0E18
n GaAs substrate		Nd~2.0E18

(a)

Material	Thickness (nm)	Doping (cm^-3)
p+ GaAs	50	Na=1.0E+19
p–GaAs	250	Na=2.0E+18
$Ga_{0.973}In_{0.027}N_{0.02}As_{0.098}$	900	None
n-GaAs	600	Nd=5.0E+17
n-GaAs		Nd~2.0E+18

(a)

Figure 4.2: $Ga_{1-x}In_xN_yAs_{1-y}$ p-i-n structures (a) "pin1", i=600 nm and N% 2.8 % (b) "pin2", i=900nm and N%=2.0 %.

4.3.2 Spectral response

The relative spectral response profiles of the p-i-n solar cells in figures 4.3 (a) and (b) confirm the absorption of $Ga_{1-x}In_xN_yAs_{1-y}$ beyond the cut-off wavelength of GaAs material. "Pin1" and "pin2" have the absorption edges of 1250 nm and 1160 nm, corresponding to band-gaps of 1.01 eV and 1.07 eV respectively. The QE of the devices could not be measured as the Silicon (110 nm cut-off wavelength) calibrated detector available would not cover the entire spectral range of the devices. However from the relatively high peaks at the lower wavelengths corresponding to $Ga_{1-x}In_xN_yAs_{1-y}$ region, it can be assumed as good QE in that region. In fact p-i-n $Ga_{1-x}In_xN_yAs_{1-y}$ solar cells with near unity QE (>70 %) has been demonstrated before [5 and 6].

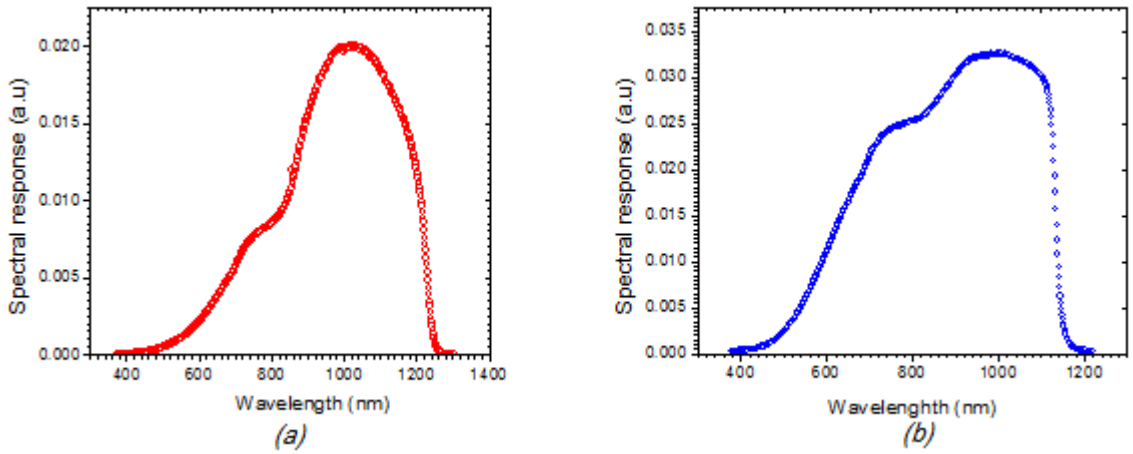

Figure 4.3: Spectral response of $Ga_{1-x}In_xN_yAs_{1-y}$ p-i-n devices (a) "pin1", i=600 nm and N%=2.8 and (b) "pin2", i=900 nm and N%=2.0, measured using the set-up shown in section (figure 3.13).

4.3.3 Dark current I-V measurements

Figure 4.4 shows the dark current density of the dilute nitride p-i-n solar cells plotted together with those of the standard GaAs p-n junction (TS0419) solar cell. From the figure it can be seen that the $Ga_{1-x}In_xN_yAs_{1-y}$ p-i-n bulk devices generate reverse saturation currents comparable to that of the GaAs p-n junction solar cell ($1x10^{-6}$ Acm^{-2} to $2x10^{-5}$ Acm^{-2} at -0.5 V). A dark current several orders of magnitude was expected from the p-i-n bulk devices as the intrinsic region extends the SCR and generation-recombination current is directly proportional to the SCR (W_d), as shown in equation 4.14;

$$J_{scr} = \frac{qn_iW_d}{\tau_{scr}} \tag{4.14}$$

where τ_{scr} is the average recombination lifetime of carriers in the SCR and all other symbols have their usual meaning. For the same reason the $Ga_{1-x}In_xN_yAs_{1-y}$ p-i-n solar cell with a 900 nm intrinsic region ("pin2"), was expected to generate more dark current than the $Ga_{1-x}In_xN_yAs_{1-y}$ p-i-n with 600 nm intrinsic region ("p-i-n1"). However the observed higher dark current in pin1 may be due to a slightly lower absorption edge (narrower

bandgap) of the ("pin1") at 1250 nm compared to 1160 nm in "pin2". The effect of bandgap narrowing is the increase in the equilibrium carrier concentration which increases the dark current. The latter effect can outweigh the effects of the thickness of the intrinsic region. The ideality factors calculated from the dark current characteristics are shown in table 4.1. Ideality factors of more than 1 are typical for $Ga_{1-x}In_xN_yAs_{1-y}$ materials [7 and 8] however ideality factor of more than 2 may indicate presence of other transport mechanism like tunnelling.

Device design	$\mathbf{n_1}$	$\mathbf{n_2}$
GaInNAs_pin2	1.75	1.75
GaInNAs_pin1	2.30	2.30

Table 4.1: Ideality factors of $Ga_{1-x}In_xN_yAs_{1-y}$ p-i-n solar cells: "pin1", i=600 nm and N% =2.8 %; "pin2", i=900nm and N%=2.0 %.

The GaAs solar cell (TS0419) shows the lowest dark current (figure 4.4) typical of a crystalline material without impurities unlike the dilute nitrites with Nitrogen defects. However the GaAs p-n junction dark current exhibited an ideality factor of more than 2.0, which was an unexpected and could not be readily explained.

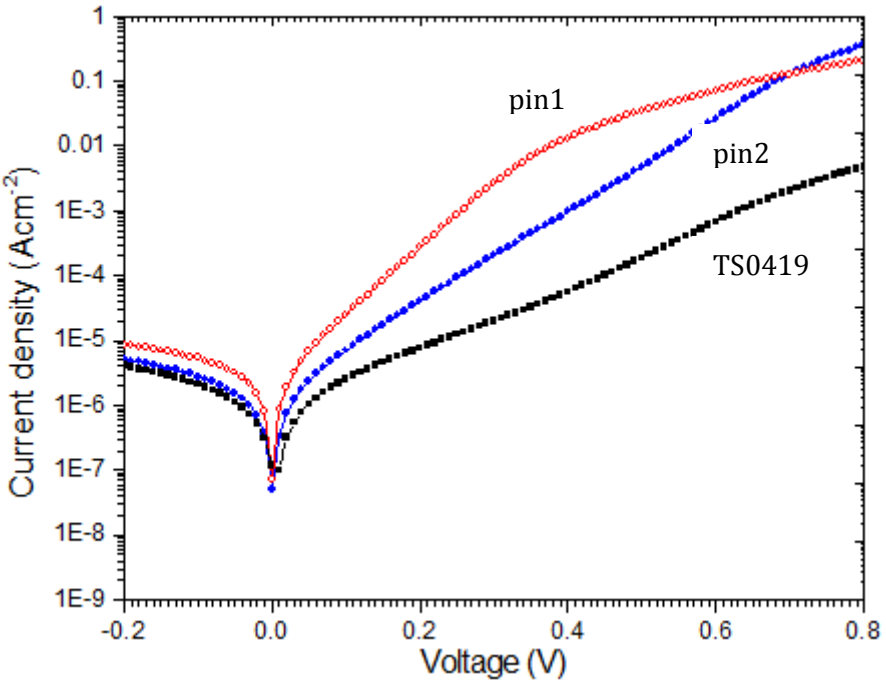

Figure 4.4: Dark current density-voltage (J-V) characteristics of bulk $Ga_{1-x}In_xN_yAs_{1-y}$ p-i-n solar cells and a conventional GaAs pn junction solar cell (TS0419): "pin2" N=2.0 %; "pin1" N=2.8 %.

4.3.4 AM1.5G I-V characteristics

Figures 4.5 (i) and 4.5 (ii) show the room temperature AM1.5G x 1 Sun I-V characteristics of "pin1" and "pin2" solar cells respectively plotted together with power developed by the solar cell. The figures of merit of the solar cells were calculated from the I-V characteristics and are shown in table 4.2.

Device	J_{sc}(mA)	V_{oc}(V)	FF(%)	η (%)
"Pin1"	13.6	0.35	54.5	2.6
"Pin2"	23.5	0.60	68.8	9.5

Table 4.2: AM1.5G figures of merit for the p-i-n bulk $Ga_{1-x}In_xN_yAs_{1-y}$ solar cells ("pin1" and "pin2").

Not all performance parameters of the two p-i-n solar cells (table 2) could be directly compared due to some differences in designs of the cells. Besides the effects of the difference in doping densities and thicknesses of the emitter and base layers, the significant difference between the two (J_{sc}) is probably due to "pin2" having an anti-reflection coating while "pin1" has none. Assuming typical reflection losses in an unprocessed GaAs substrate which varies from 23% to 40% in the wavelength range of 400 nm to 900 nm [9], a projected (J_{sc}) of 19 mAcm-2 would be achievable in "pin1", revealing that the J_{sc} of the two devices do not differ significantly. "Pin1" with a smaller larger absorption edge (smaller bandgap) is expected to have a lower V_{oc} as the results indicate. However a closer look at the difference between the absorption edges mentioned in the previous section shows that it will only result in a 0.06 eV band-gap difference in the devices. This does not account for the difference of 0.25 V observed in the V_{oc}, of the devices. Therefore the nitrogen composition which was higher in pin1 (2.8 %) and lower in "pin2" (2.0 %), is possibly the one resulting in the observed difference in the V_{oc}(s). It has been shown [10] that the reduction of V_{oc} due to material degradation as nitrogen composition increases in solar cells is more than the decrease due to band-gap narrowing. This brings us back to the importance of the quality of the dilute nitrides in solar cell performances. For the dilute nitride p-i-n to be included in tandem solar cell for enhancing performance they need to perform better than the best GaAs cell which currently has a $J_{sc} > 29$ mAcm^{-2} [11].

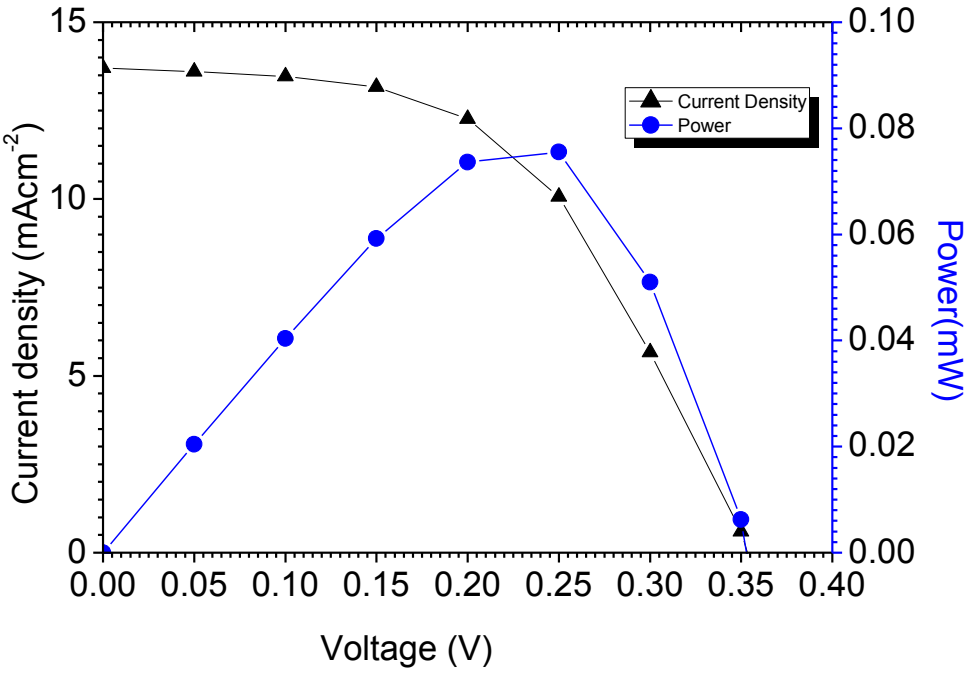

(i)

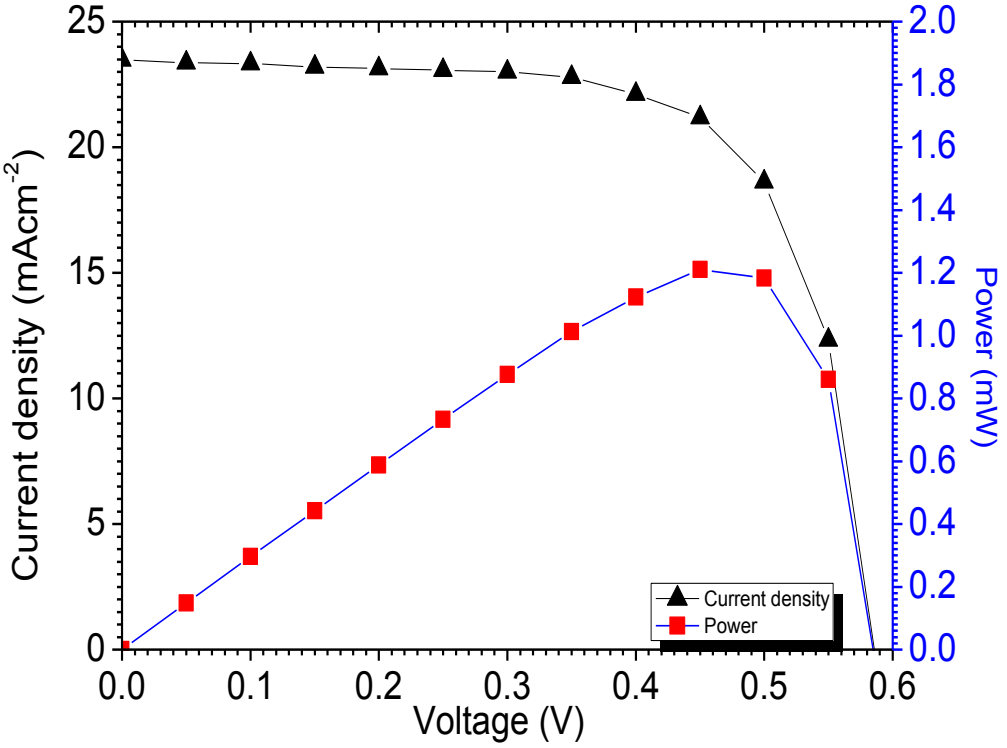

(ii)

Figure 4.5: I-V characteristics of: (i) bulk $Ga_{1-x}In_xN_yAs_{1-y}$ p-i-n solar cell, "pin1" (N04032014), i=600 nm and N=2.8 % and (ii) bulk $Ga_{1-x}In_xN_yAs_{1-y}$ p-i-n solar cell, "pin2", i=900 nm and N=2.0% under AM1.5G simulator spectrum at 1 Sun (1000 Wm^{-2})

4.3.5 Modelling of dark currents in p-i-n solar cells

The parameters used in simulating the GaAs diffusion current are shown in table 4.3.

Parameter	Value
Electron Mobility (cm^2/Vs)	1500 ($N_a=2x10^{18}$ cm^{-3}) 3000($N_a=2x10^{17}$ cm^{-3})
Hole Mobility (cm^2/Vs)	150 ($N_d=2x10^{18}$ cm^{-3}) 200($N_d=2x10^{17}$ cm^{-3})
Minority hole lifetime (ns)	10 ($N_d=2x10^{18}$ cm^{-3}) 3000($N_d=2x10^{17}$ cm^{-3})
Minority electron lifetime (ns)	1500 ($N_a=2x10^{18}$ cm^{-3}) 3000($N_a=2x10^{17}$ cm^{-3})
Intrinsic Carrier Density (cm^{-3})	$2.1x10^6$
Surface recombination velocity (cm/s)	10^2

Table 4.3: Parameters used in the diffusion current model. Mobility and lifetime values were obtained B. Royal [12].

Figure 4.6 shows the Matlab simulated diffusion dark current of the TS0419 GaAs p-n junction (base design for the $Ga_{1-x}In_xN_yAs_{1-y}$ p-i-n solar cells) plotted together with the measured dark current density of TS0419. With diffusion saturation current density in the range 10^{-15} Acm^{-2} compared to 10^{-8} Acm^{-2} in the measured dark current implies the diffusion current is negligible. The departure from the ideality factor from unity depicted by the measured dark current confirms high degree on non-radiative recombination mechanisms in the solar cells.

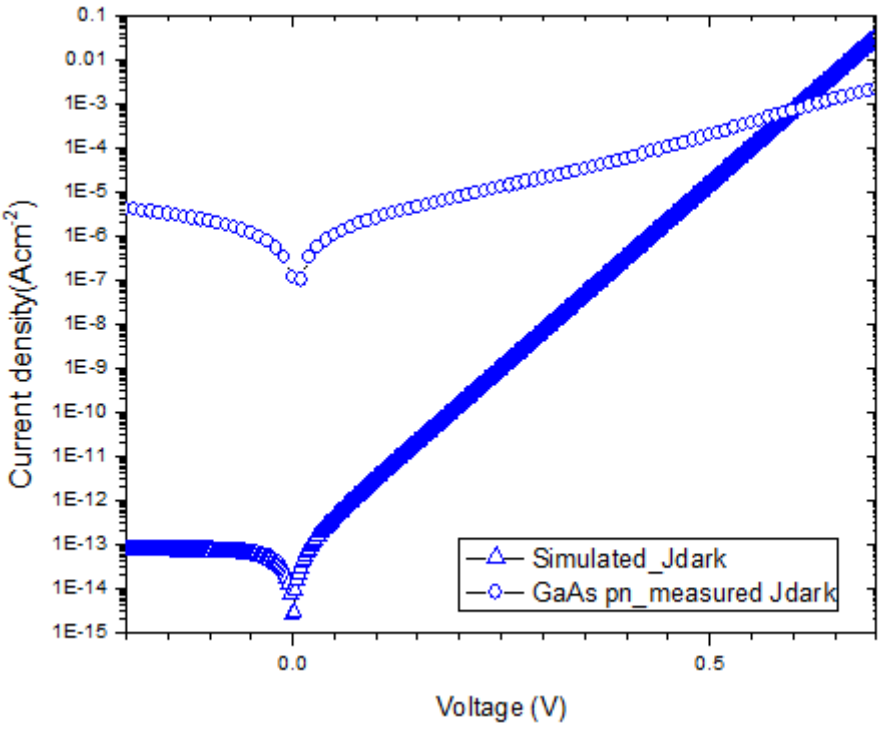

Figure 4.6: Simulated diffusion dark current density of the TS0419 GaAs p-n junction (base design for the $Ga_{1-x}In_xN_yAs_{1-y}$ p-i-n solar cells) plotted together with the measured dark current density of TS0419 GaAs p-n junction solar cell.

In a material where there is high density of traps such as dilute nitrides [10] the SCR dark current can be comparable or even dominate the total dark current of the junction [13, 14]. The classic Sah-Noyce-Shockley (S-N-S) theory for generation-recombination in a material with a trap lying deep in the band-gap is given by equation 4.16;

$$J_{scr} = \frac{qn_iW_d}{\sqrt{\tau_{no}\tau_{p0}}}\frac{2\sinh(eV/2kT)}{e(V_{bi}-V)/kT}f(b) \tag{4.16}$$

where

$$b = \exp\left(-\frac{eV}{2kT}\right)\cosh[(E_t - E_i)/kT + \frac{1}{2}\ln(\tau_{no}\tau_{p0})] \tag{4.17}$$

and $n_i, W_d, \tau_{n0}, \tau_{p0}, V_{bi}, E_t,$ and E_i are intrinsic carrier density, depletion width thickness, electron capture lifetime, hole capture lifetime, built in voltage, energy level of generation-recombination centres or traps energy level, intrinsic Fermi level respectively.

The function $f(b)$ is a slowly varying function of voltage, trap level and lifetime. Under small forward biased condition, (low injection level), the variation of $f(b)$ with applied voltage can be used to extract the dominant trap energy level (E_t) and the average recombination lifetime ($\tau_{avg} = \sqrt{\tau_{n0}\tau_{p0}}$), by a two parameter fit of the S-N-S model to the measured dark current. The average carrier lifetime and the dominant trap level in the early dilute nitrides were measured in bulk $Ga_{1-x}In_xN_yAs_{1-y}$ p-n homojunctions using a two parameter fitting method [13].

However under sufficiently large forward biases, the function $f(b)$ tends to saturate at π/2 [1], and the S-N-S can be approximated as;

$$J_{scr} = \frac{en_iW_d}{\sqrt{\tau_{n0}\tau_{p0}}} \frac{2\sinh(eV/2kT)}{e\,(V_{bi}-V)/kT} \frac{\pi}{2} \tag{4.17}$$

Equation 4.17 leaves only one parameter of interest which is the average recombination lifetime, which can be used as a fitting parameter to the measured dark current density. The results from Friedman et al [13] showed that in $Ga_{1-x}In_xN_yAs_{1-y}$ (dilute nitride) homo-junctions the dark current is dominated by the SCR generation-recombination current, and the dark current could be modelled accurately with the S-N-S model. In this work it is shown that the dark current density of p-i-n $Ga_{1-x}In_xN_yAs_{1-y}$ dilute nitride is dominated by the generation-recombination in the SCR (essentially the $Ga_{1-x}In_xN_yAs_{1-y}$ intrinsic region). Therefore the dark current density of the p-i-n $Ga_{1-x}In_xN_yAs_{1-y}$ can be modelled by the S-N-S applied to the $Ga_{1-x}In_xN_yAs_{1-y}$ (SCR).

Under low forward bias injection condition (40-300 mV), the dark current is dominated by the recombination in the SCR [15 and 16]. In p-i-n structures the SCR can be taken as the sum of the intrinsic region and the depletion width with acceptable accuracy [17]. In a relatively large intrinsic region, such as those used in this work (600 nm and 900 nm); the dark current is expected to be essentially the recombination in intrinsic regions of the p-i-n structures ($Ga_{1-x}In_xN_yAs_{1-y}$).

The n_i is a function of the band-gap (E_g) and effective masses of electrons and holes m_e^* and m_h^* respectively and given by;

$$n_i(T) = 2\left(\frac{2\pi kT}{h^2}\right)^{\frac{3}{2}}\left(m_n^* m_p^*\right)^{\frac{3}{4}} exp\left(\frac{-E_g}{2kT}\right) \tag{4.18}$$

and

$$m_h^* = (m_{lh}^{*3/2} + m_{hh}^{*3/2})^{2/3} \tag{4.19}$$

where m_{lh} and m_{hh} are the light and heavy hole effective masses and all other symbols have their usual meaning.

The density of states effective mass of electrons in $Ga_{1-x}In_xN_yAs_{1-y}$ was derived from the dispersion relation equation predicted by the VBAC model as shown in equation 4.19

$$m_{GaInNAs}^*(E) = m_{GaInNAs}^*\left[1 + \left(\frac{V_{NN}}{E_N - E}\right)\right] \tag{4.19}$$

The heavy and light hole masses were assumed unchanged from that of GaAs and the masses were taken from literature.

The barrier potential V_{bi} was calculated from doping concentrations of the junction given by equation 4.20, assuming doping concentration did not change much due to background doping.

$$V_{bi}=\frac{kT}{q} ln\left(\frac{N_d N_a}{n_i^2}\right) \tag{4.20}$$

The band-gap of the bulk $Ga_{1-x}In_xN_yAs_{1-y}$ in the devices was determined from the spectral short circuit measurements and the effective mass of electrons from available literature [12].

The parameters used in the model together with the deduced average recombination lifetimes are shown in table 4.4. The derived average recombination time was used as a fitting parameter to the measured dark current density.

Design	Material	W_d (nm) T=300 K	E_g (eV)	m_e^*/m_o	m_{lh}^*/m_o	m_{hh}^*/m_o	n_i (cm^{-3})	τ_{avg} (ns)
Pin2	$Ga_{0.906}In_{0.094}N_{0.028}As_{0.972}$	900	1.07	0.081	0.076	0.50	1.29E+9	0.50
Pin1	$Ga_{0.906}In_{0.094}N_{0.028}As_{0.972}$	600	1.01	0.082	0.076	0.50	4.82E+9	0.15

Table 4.4: Parameters used in the model of the solar cells under study and calculated values of average recombination lifetimes (τ_{avg}). m_{lh}^*/m_o, m_{hh}^*/m_o and m_e^*/m_o values were taken from references [2 and 18].

Figures 4.7 and 4.8 show the measured dark current density (empty circles), and the current density simulated by the S-N-S model (solid triangles) for the "pin1" and "pin2" solar cells. The slight departure of the model values from the measured values of the dark current at applied voltages above 0.25 V was thought to be the S-N-S underestimating the dark current due to carrier injection near flat band condition. However for "pin2" at voltages above 0.25 V, the S-N-S model shows slightly higher values for dark current than the measured dark current which rules out the possibility of the injection (diffusion) current setting. In general the overall fit to the S-N-S is fairly good on both plots of the dark current.

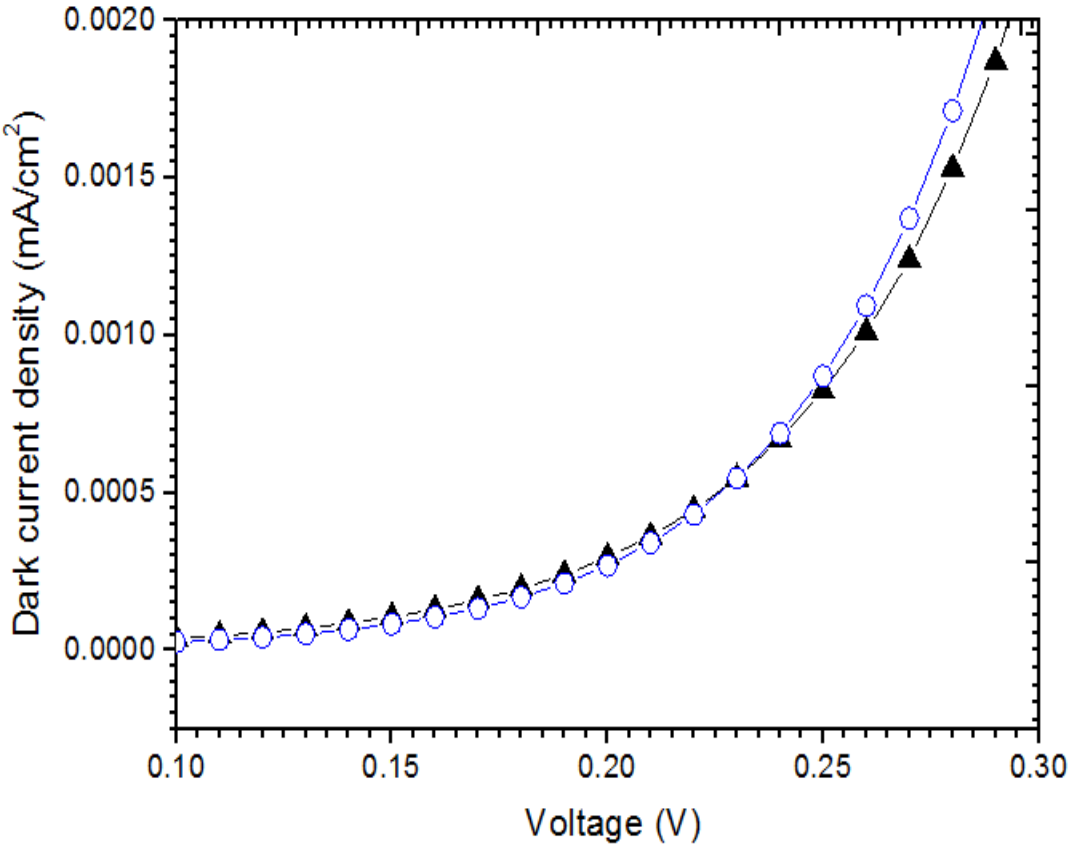

Figure 4.7: Dark current J-V characteristics for $Ga_{1-x}In_xN_yAs_{1-y}$ *"pin1" solar cell: Solid triangles: S-N-S model calculations, Empty circles: Measured dark current.*

The values of the effective recombination lifetimes for dilute nitrides in this work, which vary between 0.15 to 0.50 ns in $Ga_{1-x}In_xN_yAs_{1-y}$ p-i-n solar cells with nitrogen composition of 2.8 and 2.0 % respectively, are in good agreement with those reported in dilute nitrites in literature [19 and 20]. RT recombination lifetimes for dilute nitrides with nitrogen composition between 1.5-2.4 % have been reported commonly to vary between 0.2 ns to 0.9 ns [19].

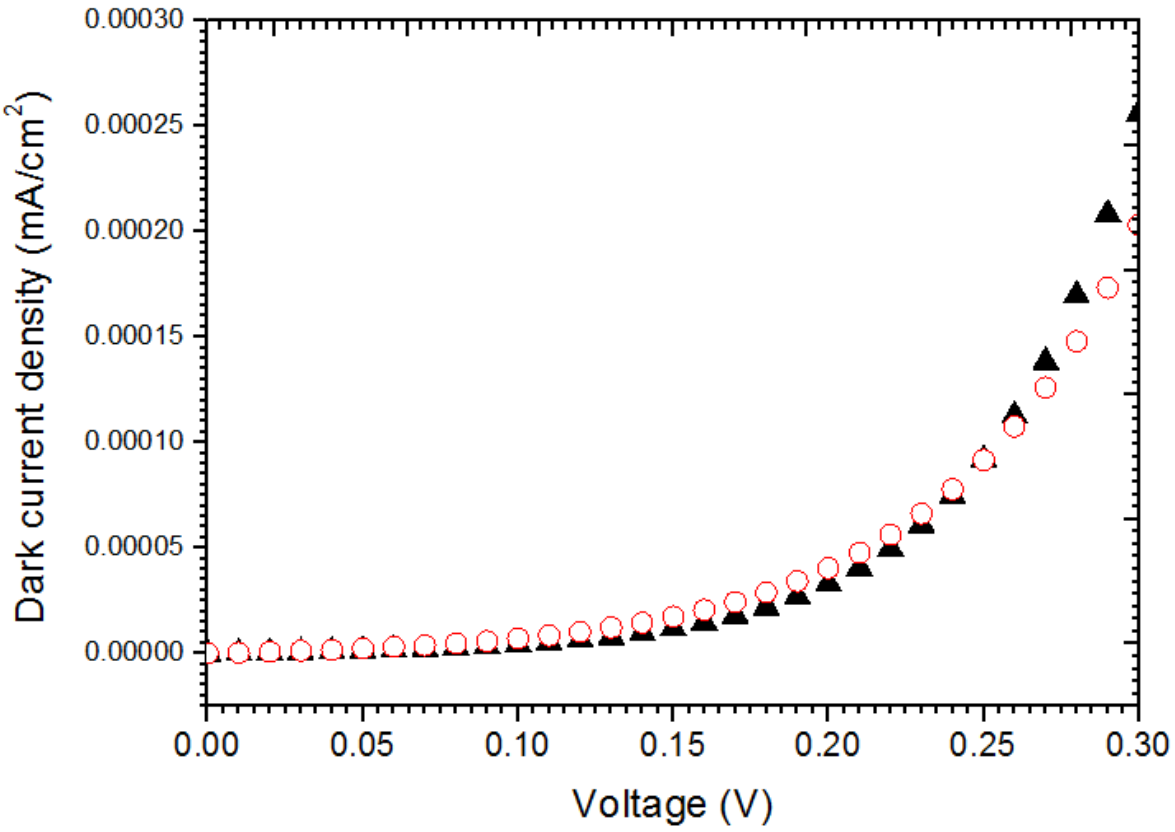

Figure 4.8: Dark current J-V characteristics for $Ga_{1-x}In_xN_yAs_{1-y}$ "pin2" solar cell: Solid triangles: S-N-S model calculations, Empty circles: Measured dark current

4.3.6 Temperature dependence on maximum power

The maximum power of the $Ga_{1-x}In_xN_yAs_{1-y}$ *"pin2"* solar cell was calculated from the light I-V characteristics of the device, measured at different temperatures, under AMG1.5 simulator spectrum. The normalised maximum power was then plotted as a function of temperature as shown in figure 4.9. The temperature coefficient of efficiency of "pin2" solar calculated from figure 4.9 was -0.5 x10^{-3} K^{-1}.

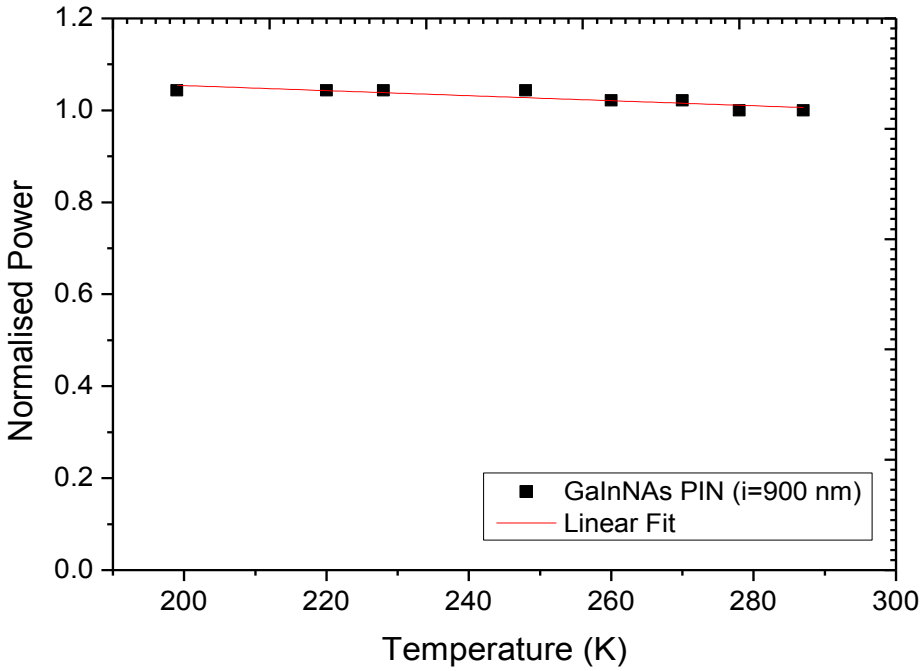

Figure 4.9: AM1.5G J-V characteristics of a $Ga_{1-x}In_xN_yAs_{1-y}$ "pin2" with temperature normalised at room temperature.

4.3.7 Temperature dependence of dark current

The dark current versus temperature J-V characteristics of "pin2" $Ga_{1-x}In_xN_yAs_{1-y}$ solar cell is shown in figure 4.10. The plot shows a typical response of dark current to temperature. When a semiconductor is cooled down its band-gap widens, as a result fewer carriers have sufficient energy to cross the band-gap, effectively reducing the intrinsic carrier density at lower temperatures. Therefore there are fewer carriers that can contribute to the dark current by recombination in any part of the device.

Secondly as the p-n junction cools down the band-gap widens, therefore the applied voltage required to reach the flat band condition increases, the effect of which is observing the injection component of the dark current at progressively high voltages as the temperature drops, as the plots in figure 4.10 shows.

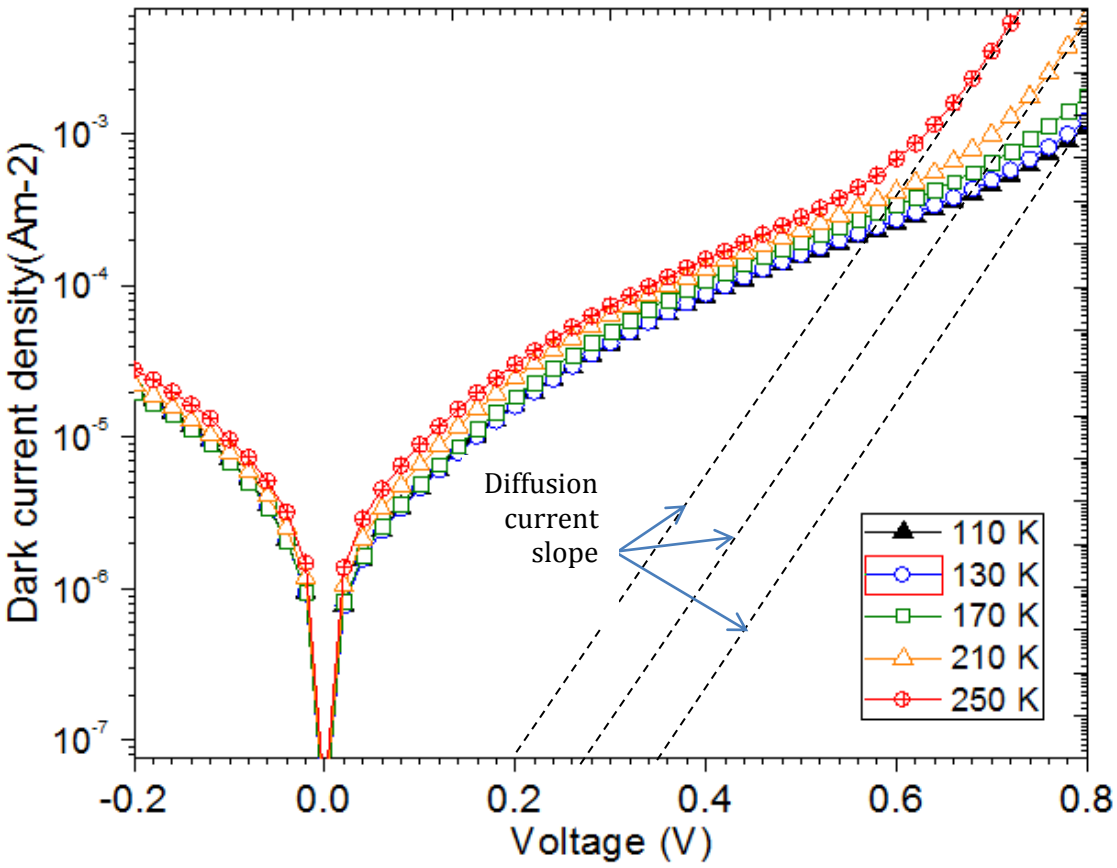

Figure 4.10: Dark current J-V characteristics for a $Ga_{1-x}In_xN_yAs_{1-y}$ "pin2" solar cell with temperature. Diffusion current slope appear at progressively high voltages with decreasing temperature.

4.3.8 Performance at different radiation levels

Figure 4.11 shows the RT J-V characteristics of a "pin1" from 500 Wm^{-2} to 1500 Wm^{-2}. The graphs show a short circuit current increasing linearly with increasing irradiance taking into account the spatial fluctuation of the lamp source at about 20%. Although the actual value of series resistance for "pin1" was not quantified, the effect of series resistance is seen from the shape of the J-V characteristic curve figure which has a low *FF* of 54 % under AM1.5 G spectrum concentrated at 1 Sun. This can be compared to a square like I-V graph of "pin2" (figure 4.13), with a *FF* of 69 % under AM1.5G spectrum concentrated at 1 Sun, which implies it has less series resistance compared to pin1. In solar cell that is meant to operate at

elevated irradiance (Concentrator Solar Cells), series resistance effect becomes important performance factor. The maximum power increases with irradiance as shown in figure 4.12, in agreement with theory discussed at in section 4.1.4. However the *FF* starts to deteriorate, as shown by the negative gradient of the *FF* versus irradiance plot. It must be noted that the scale of the *FF* and power are different hence the shape of the graph do not show relative magnitudes but only the trend. It can be seen that an increase from 1.00-4.25 (425 %) for power corresponds to 1.0-0.83 (17 %) reduction of *FF*, thus a relatively small change in fill factor, however at concentrator levels the effect can be significant.

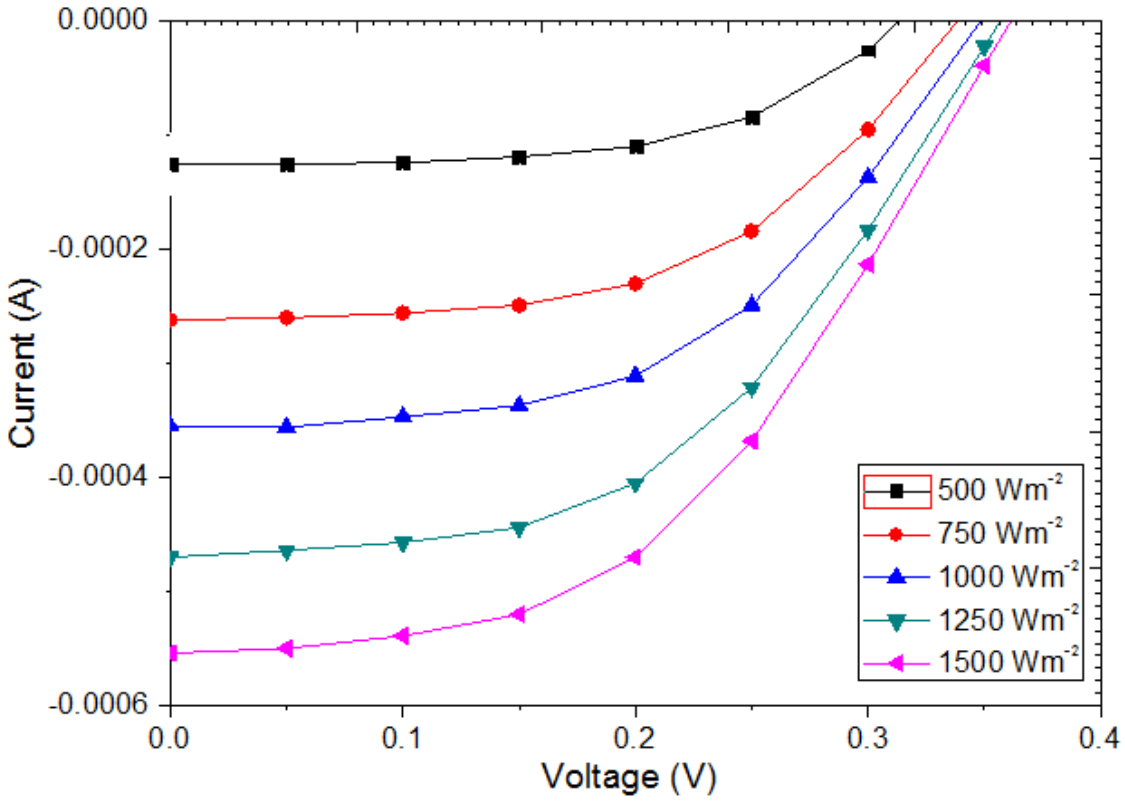

Figure 4.11: I-V characteristics of a $Ga_{1-x}In_xN_yAs_{1-y}$ p-i-n solar cell, "pin1" under AMG1.5 simulator spectrum at different intensity levels.

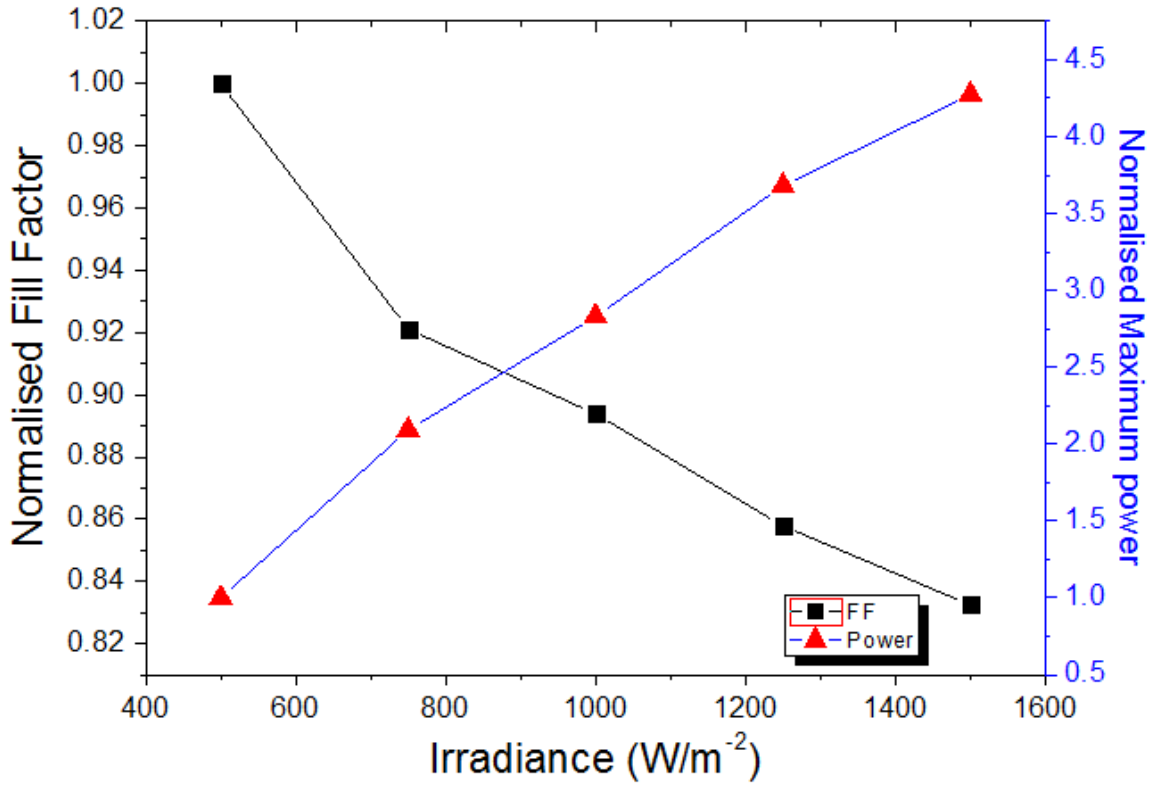

Figure 4.12: The dependence of maximum power and FF of a GaInNAs "pin1" solar cell on the AM1.5G simulator spectrum at different intensity levels.

On the other hand the irradiance responsivity of "pin2" shows both improvement of the maximum power developed and the *FF*, figure 4.14. The improvement of the *FF* can still be explained by low series resistance depicted by the square like shape of "pin2" J-V characteristics. However a closer look at the magnitude of these values show that while the *FF* of "pin2" was slightly increasing, from 1.00 to 1.030 between 500 Wm^{-2}-1500 Wm^{-2}, it represent only 3.0 % improvement in *FF*. Similarly maximum power developed show a 300 % gain over the same range.

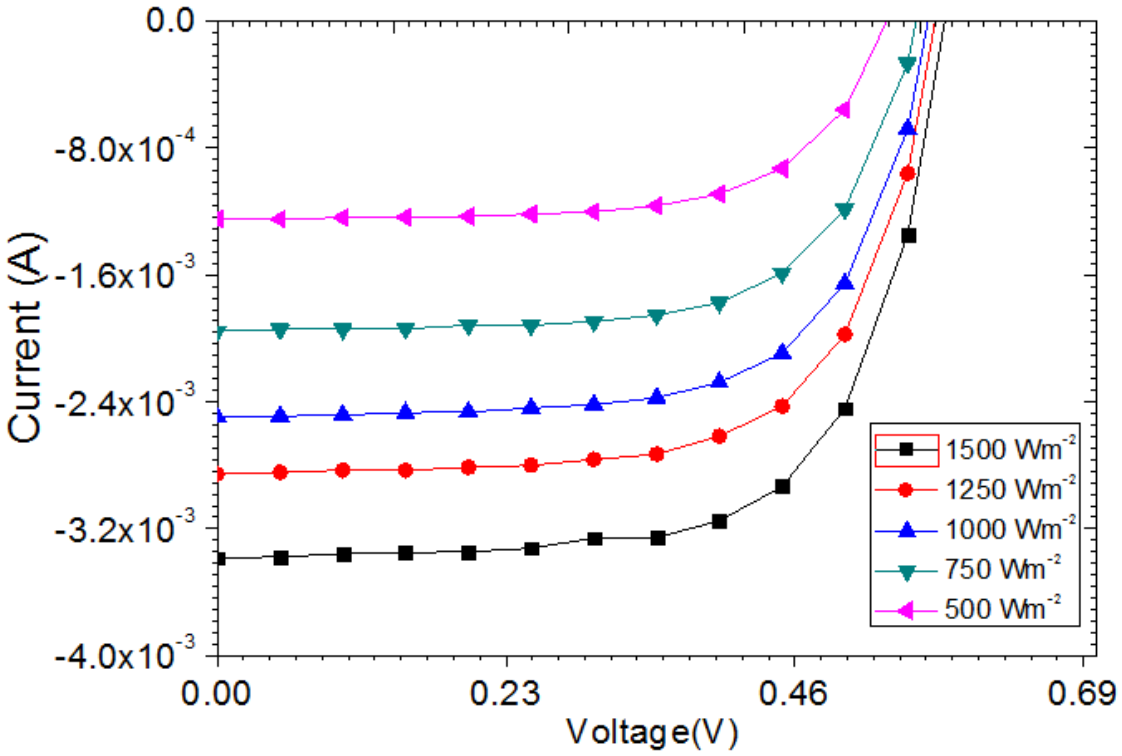

Figure 4.13: I-V characteristics of a $Ga_{1-x}In_xN_yAs_{1-y}$ p-i-n solar cell, "pin2" under AMG1.5 simulator spectrum at different intensity levels.

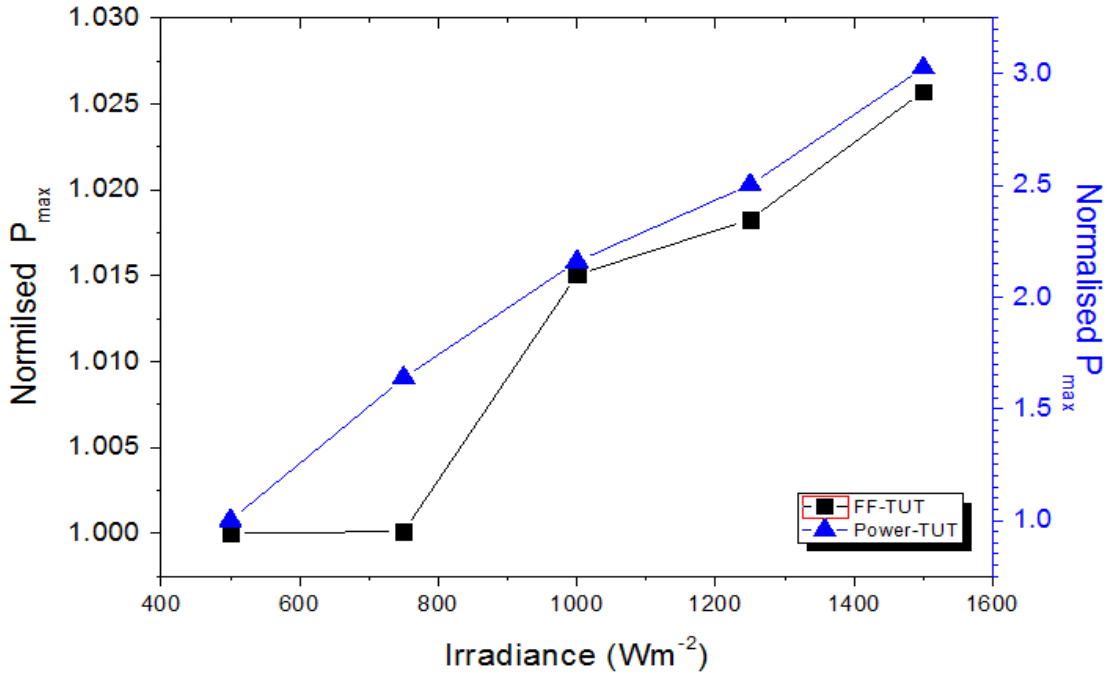

Figure 4.14: The dependence of maximum power and FF of a GaInNAs "pin1" solar on the AM1.5G simulator spectrum at different intensity levels.

4.4 Multiple Quantum Well solar cells

4.4.1 Device structures

The MQWs solar cell devices under study included: n-i-p (VN1585) solar cells with ten 10 nm $Ga_{0.97}In_{0.03}N_{0.01}As_{0.99}$ quantum wells (QWs) separated with 10 nm GaAs barriers. The other set of MQWs are the p-i-n structures (ASN2604 and ASN2605) with $Ga_{0.96}In_{0.04}N_{0.015}As_{0.098}$ quantum wells of width varying between 3.8 nm and 10 nm separated with 10 nm GaAs barriers. ASN2605 was annealed at 750 °C for 5 min and ASN2604 was as grown. The last set of MQWs solar cells is two p-i-n structures; (ASN3134 and ASN3138) with 10 and 20 $Ga_{0.952}In_{0.048}N_{0.016}As_{0.98}$ quantum wells, respectively separated by 10 nm GaAs barriers. The structure of all the MQWSs solar cells are shown in figure 4.15.

Material	Thickness (nm)	Doping (cm^-3)
p+ type GaAs	200	(Be) 2E+18
P type $Al_{0.8}GaAs_{0.2}As$	40	(Be) 2E+18
p type GaAs	600	(Be) 2E+18
UD	20	UD
i	10	i
UD	10	UD
i	10	i
UD	10	UD
i	10	i
UD	10	UD
i	10	i
UD	10	UD
i	10	i
UD	10	UD
i	10	i
UD	10	UD
i	10	i
UD	10	UD
i	10	i
UD	10	UD
i	10	i
UD	10	UD
i	10	i
UD	20	UD
n type GaAs	1900	(Si) 2E+17
n+ type GaAs	20	(Si) 2+18
n + Substrate		

(i)

Material	Thickness (nm)	Doping (cm^-3)
p+ type GaAs	200	(Be) 2E+18
p type $Al_{0.8}GaAs_{0.2}As$	40	(Be) 2E+18
p type GaAs	250	(Be) 2E+18
UD	20	UD
i	3.8	i
UD	10	UD
i	4.3	i
UD	10	UD
i	4.6	i
UD	10	UD
i	5.1	i
UD	10	UD
i	5.5	i
UD	10	UD
i	6.1	i
UD	10	UD
i	6.9	i
UD	10	UD
i	7.8	i
UD	10	UD
i	9.1	i
UD	10	UD
i	10.1	i
UD	20	UD
n type GaAs	600	(Si) 2E+17
n+ type GaAs	20	(Si) 2+18
n + Substrate		

(ii)

Material	Thickness (nm)	Doping (cm^-3)
n type GaAs	200	(Si) 2E+18
n type $Al_{0.8}GaAs_{0.2}As$	40	(Si) 2E+18
n type GaAs	200	(Si) 2E+18
UD	110	UD
i	10	i
UD	10	UD
i	10	i
UD	10	UD
i	10	i
UD	10	UD
i	10	i
UD	10	UD
i	10	i
UD	10	UD
i	10	i
UD	10	UD
i	10	i
UD	10	UD
i	10	i
UD	10	UD
i	10	i
UD	10	UD
i	10	i
UD	10	UD
i	10	i
UD	110	UD
p type GaAs	3000	(Be) 2E+17
p+ type GaAs	20	(Be) 2+18
p + Substrate		

(iii)

Figure 4.15: Structures of MQWs solar cells under study: (i) ASN3134 & ASN3138, (ii) ASN2604 &ASN2605 and (iii) VN1585

4.4.2 Spectral response

The relative spectral response two MQWs devices chosen for comparing the n on p to the p on n designs in $Ga_{1-x}In_xN_yAs_{1-y}$ MQWs solar cells are shown in figures 4.16 (i) and (ii)

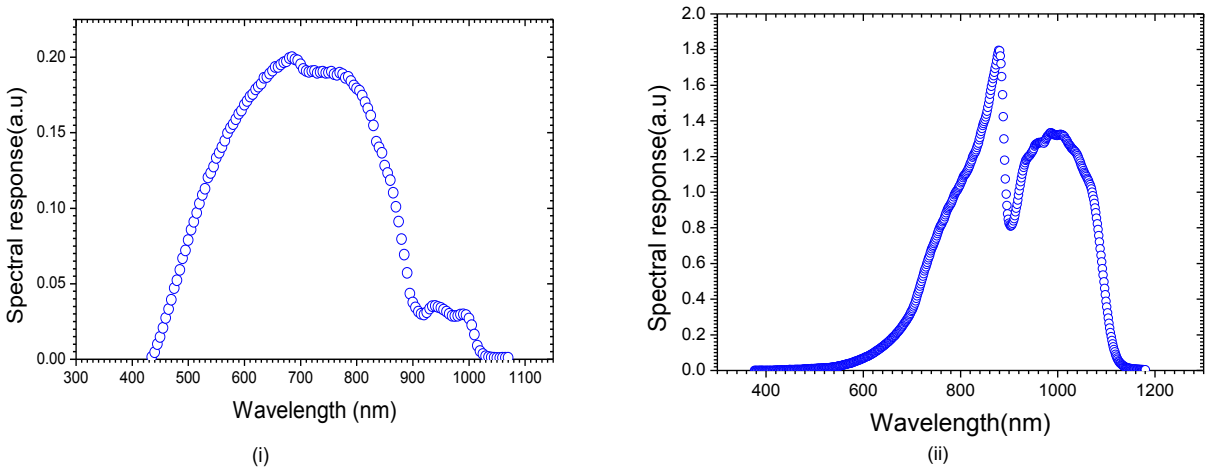

Figure 4.16: Spectral response profile of: (i) an n-i-p MQWs-VN1585 (ii) p-i-n ASN2605 Solar cells

The spectral response of the devices confirms the absorption in the QW regions (beyond GaAs cut-off). What is evident from figure 4.16 (i) and (ii), is the opposite response at the short and long wavelength of the spectrum. The n on p MQW device (VN1585) shows a stronger response at shorter wavelengths and diminished response in the MQW region. On the other hand the p on n MQW device (ASN2605) shows a diminished response at shorter wavelengths (a typical GaAs response is high in the region 500 nm to 870 nm) and a stronger response at longer wavelengths (MQWs region). Effect of nitrogen as discussed in previous chapter is perturbation of the conduction band and negligible effect on the valence band. This results in $Ga_{1-x}In_xN_yAs_{1-y}$ QWs having more electron confinement potential and a quasi 3D condition for holes. Given this picture, in an n on p $Ga_{1-x}In_xN_yAs_{1-y}$ MQWs solar cell, for the electron hole pairs (EHPs) generated in the emitter layer, only the holes will have to cross the intrinsic region with little or no potential impedance (low confinement potential for electrons). Hence the photogenerated current from the emitter or short wavelengths will be

relatively stronger. For the EHPs generated in the deeper parts (base region) the electrons will have to cross the entire intrinsic region which has a strong potential fluctuation for the electrons. Therefore recombination of carriers is likely to occur before the charge is collected to the external circuit. The overall effect is that in an n on p $Ga_{1-x}In_xN_yAs_{1-y}$ MQWs, the contribution of photocurrent can be poor at longer wavelengths (deeper parts of the device) and stronger at shorter wavelengths (shallower regions of the device), as is observed in the spectral response profile of VN1585 figure 4.16 (i). The same argument holds for a p on n design with the reverse effect revealed by the spectral profile of 4.16 (ii). The results show the importance of considering the nature of potential confinement (energy band profile) of quantum well solar cells when designing devices.

4.4.3 Dark Current I-V measurements

Figure 4.17 shows the dark J-V characteristics all p-i-n MQWs solar cells studied in this work. With exception to VN1585, all MQWs solar cell show dark currents higher than that of the bulk p-i-n solar cells discussed in the preceding section (figure 4.4). The MQWs dark current show anomalously high ideality factors of n1= 2.17 to 8.72 and n2=3.05 to 13.05 (table 4.5).

Device design	**n_1**	**n_2**
GaInnAs MQWs_VN1585	2.51	3.05
GaInNAs MQWs_ASN3138	2.13	6.79
GaInNAs_MQWs_ASN2605	2.78	7.18
GaInNAs_ MQWs_ASN2604	5.57	13.05
GaInNAs_MQWs_ASN3134	8.72	8.72

Table 4.5: The ideality factor of the $Ga_{1-x}In_xN_yAs_{1-y}$ MQWs solar cells calculated from the dark current I-V characteristics

The high dark current exhibited by the MQWs solar cells may be associated with extra recombination of carriers trapped in the QWs. However the high ideality factors observed does not support this claim. The increased recombination inside the QWs would tend to increase the radiative component of the dark current resulting in lower ideality factors, or steeper slopes of the graphs (n=1 for radiative recombination).

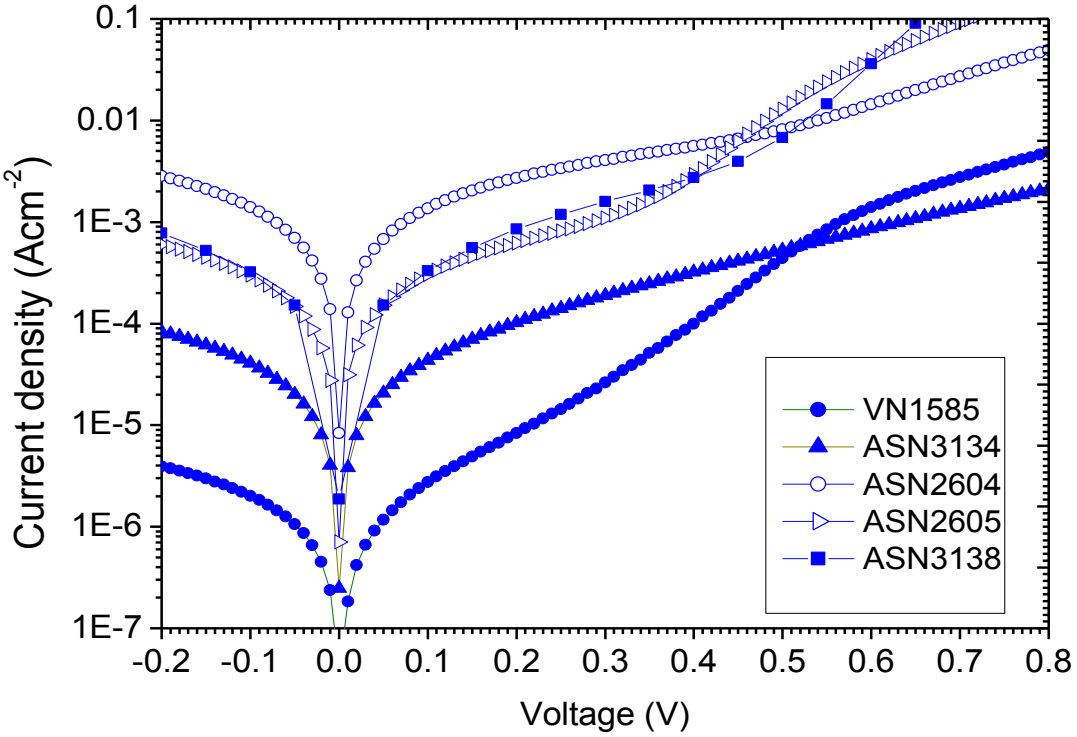

Figure 4.17: Dark current density-voltage (J-V) characteristics of $Ga_{1-x}In_xN_yAs_{1-y}$ MQWs p-i-n solar cells with QWs of nitrogen composition between 1.0 % to 1.6 %. VN1585; N=1.0%, ASN2604 and ASN2605; N=1.5%, ASN3134 and ASN3138; N=1.6 %.

Therefore the relatively high dark current is more likely to be due to defects. Indeed uncommonly high idealty factors in dilute nitride alloys have been observed by a number of researchers [21-23]. Xu et al [22] attributed the high ideality factors to deep-level-assisted tunnelling while Shah et al [21] attributed it to Si doping in the quantum well barriers. In these devices it is a reasonable assumption that deep-level assisted tunnelling as stated by [22] could be a major mechanism resulting in the high values of ideality factors. This claim may be supported by the comparison of the dark currents in ASN2604 and ASN2605, which

are the same design with the latter un-annealed and the former is an asgrown material. The dark current from the ASN2605 as shown with empty triangles (figure 4.17) is reduced by an order of magnitude compared to that of ASN2604 (empty circles; figure 4.17). In addition the slope of the J-V characteristics of ASN2605 shows the emergence of radiative dominated current (steep slope) from 0.35 V as opposed to ASN2604 current which remains non-radiative recombination dominated until a relatively weak radiative current slope emerges around 0.5 V. However is still not clear whether these defects are structure related (MQW/barrier interface defects) or is material related defects (defects inherent to dilute nitrides).

Theoretically the intrinsic impact of QWs in the in MQWs solar cells, would be such that the dark current density is reduced, [24-26] due to supressed qausi-fermi levels in the quantum wells region. This theory is based on the experimental results that show that relaxation of carriers in QW is slower than in the bulk material if there is a high carrier density. The energy difference between quasi Fermi levels compared with the associated energy band can be used as a measure of the local carrier concentration. Carrier concentration at any point in the material determines the recombination rate. In a p-i-n structure at the edge of the intrinsic regions the carriers get injected at higher velocity due to strong electric field, resulting in hot carriers near the intrinsic region edges. The heated electrons results in low carrier concentrations and hence low recombination rate. This effect has been modelled using SimWindows [27] model, and a dip in the quasi Fermi levels in the intrinsic regions of a p-i-n structure is observed. [28]. In MQWs p-i-n structures this effect is expected to increase due to even slower carrier relaxation. Therefore a p-i-n with MQWs in the intrinsic region is expected to have lesser recombination in the intrinsic region compared to a p-i-n with a bulk intrinsic region. Less recombination results in less dark current density. Therefore an ideal MQWs solar cells should have lower dark currents which exhibit a stronger radiative

component, resulting in slightly steeper slope of semi-log I-V plots compared to a similar the bulk p-i-n and single p-n junction. Except for VN1585, all MQWs solar cells generate dark current >10^{-4} Acm^{-2} at -0.2 V (figure 4.17), which is higher than the dark current in the bulk p-i-n devices in the order of 10^{-6} Acm^{-2} at -0.2 V. (figure 4.4).

The effective recombination lifetimes in MQWs was estimated by a single parameter fit to the measured dark using the expression of generation-recombination current shown in equation 4.21,

$$J_{rg} = \frac{en_i W_d}{2\tau_{scr}} e^{\frac{qV}{2kT}} \tag{4.21}$$

where all symbols have their usual meaning. Assuming the recombination current is dominated by the recombination in the quantum wells, W_d can be taken as the total width of all QWs [29]. The results of effective lifetime are shown in table 4.6.

Design	Material	W_d (nm)	E_g (eV) T=300 K	m_e^*/m_o	m_{lh}^*/m_o	m_{hh}^*/m_o	n_i (cm^{-3})	τ_{avg} (ps)
VN1585	$Ga_{0.97}In_{0.03}N_{0.01}As_{0.99}$	100	1.26	0.078	0.076	0.50	6.7E6	65
ASN2604	$Ga_{0.96}In_{0.04}N_{0.015}As_{0.98}$	63	1.20	0.080	0.076	0.50	1.32E8	0.5
ASN2605	$Ga_{0.96}In_{0.04}N_{0.015}As_{0.98}$	63	1.17	0.080	0.076	0.50	2.17E8	0.4
ASN3134	$Ga_{0.952}In_{0.048}N_{0.016}As_{0.98}$	100	1.17	0.08	0.076	0.50	2.17E8	14
ASN3138	$Ga_{0.952}In_{0.048}N_{0.016}As_{0.98}$	200	1.15	0.08	0.076	0.50	2.17E8	13

Table 4.6: Average recombination times in SCR of $Ga_{1-x}In_xN_yAs_{1-y}$ MQWs deduced from dark current measurements

All the calculated effective lifetimes in MQWs are two to three orders of magnitude less than the ones observed in p-i-n solar cells discussed in section 4.2. The MQWs cell with lowest dark current VN1585 as shown in fig 4.17 has highest value for recombination time as expected. The rest of the MQWs cells show very low recombination lifetimes, which vary randomly from device to device without apparent correlation to any parameter.

4.4.4 AM1.5G I-V characterisation

Figure 4.18 shows the AM1.5G J-V characterisation of the best MQWs (VN185) at 1 SUN and plotted together with the maximum power developed by the cell. The measured; short circuit current density (J_{sc}), open circuit voltage(V_{oc}), fill factor (*FF*) were: 0.63 V, 10.6 mAcm^{-2} and 66 % respectively. It is noteworthy to mention that the V_{oc} is higher than those recorded by both the p-i-n devices discussed. This relatively higher V_{oc} is due to the lower dark current observed in VN1585 that is comparable to that of the p-i-n bulk structures (figure 4.4). This condition can occurs if the intrinsic impact of the quantum well system is not dominated by the growth defects (barrier/quantum wells defects) or material defects.

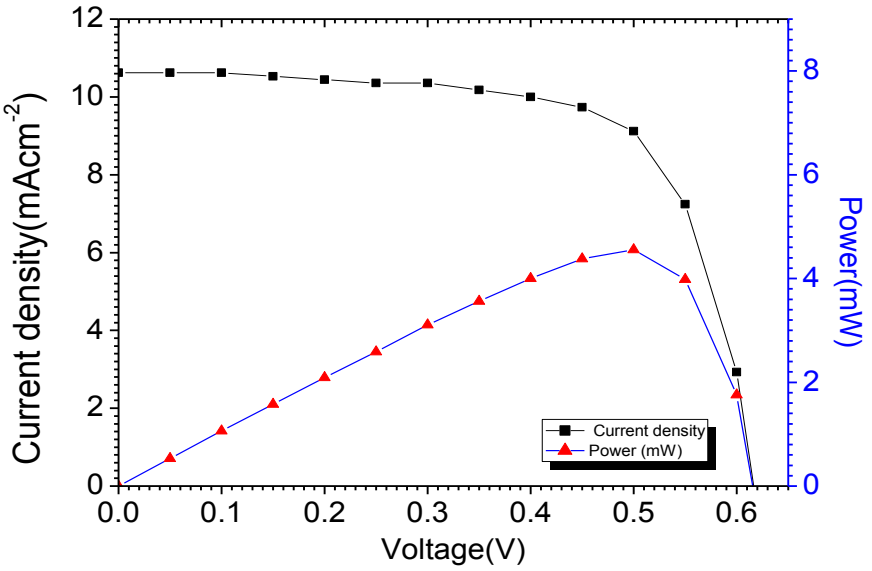

Figure 4.18: I-V characteristics o f $Ga_{1-x}In_xN_yAs_{1-y}$ MQWs solar cell (VN1585) with N% composition of 1.0 %, under the AM1.5G simulator spectrum at 1 Sun (1000 Wm^{-2})

4.4.5 Temperature dependence of maximum power

The temperature responsivity of efficiency or power of MQWs solar cell has been a subject of inreset particularly owing to their promising perormance in concentrators photovoltaics where temperature is elevated significantly from the room temperature. Although in this work the devices were cooled down, a trend on how they will respond to temperaure can be deduced and possibly be used to predict the behaviour at higher temperatures. Figure 4.19 shows the maximum power versus temperature for MQWs solar cell VN1585 normalized at room temperature. The plot shows a nearly flat response with temperature between 120 K and 300 K (room temperature). This low or good temperature coefficient of efficiency observed in MQWs solar cells can be explained by carrier process (escape, recombination and tunnelling) in the quantum wells. Although the low temperature coefficient is observed at low temperature as in this work, some experimental work on MQWs show that there is no further improvement at elevated temperatures because the QE tends to saturate at room temperature [5, 25]. Other work has pointed out that at room temperature carrier capture and escape processes are faster than the competing recombination processes [30], therefore there is no further benefit of carrier escape from the wells as the temperature rises beyond room temperature. The relatively lower temperature coefficients of efficiency in MQWs compared to rest of the solar cells (standard GaAs p-n junction, bulk p-i-n, and n-i-p-i) is attributed to the weak response of the dark current of the MQWs to temperature changes as shown in figure 4.20. This weak temperature response of dark current is a direct consequence of competing processes of carrier escape and recombination inside the well. If the recombination processes are dominant compared to escape process; a reduced voltage will result and less power or efficiency. Although a flat temperature response of efficiency is an unexpected observation for solar cells, the possibility of even a positive temperature dependency of efficiency on MQWs solar cells had been predicted before [29].

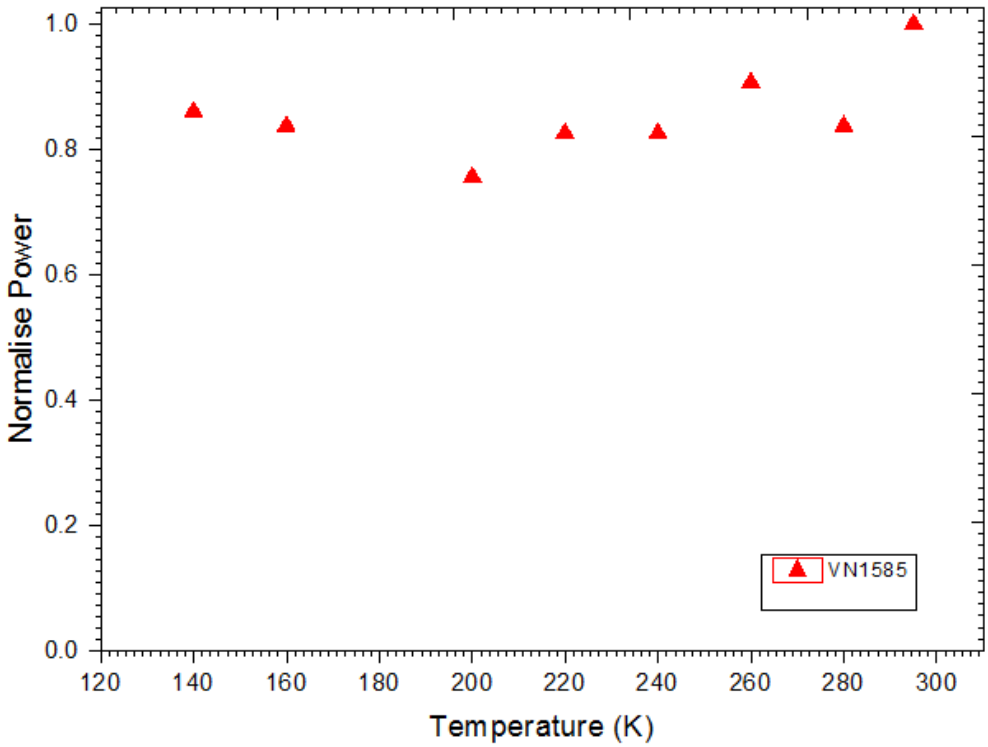

Figure 4.19: Temperature dependency of maximum power developed by a $Ga_{1-x}In_xN_yAs_{1-y}$ MQWs solar cell (VN1585) with N% composition of 1.0 %.

4.4.6 Temperature effects on dark currents

The temperature dependency of the best MQWs solar cell is shown in figure 4.20. The plots exhibits roughly three regions labelled 1, 2 and 3. Region 1 is at low applied voltages and the effective height of the quantum well is at its lowest value, therefore the carriers escape very fast from the quantum wells. If the escape time is faster than the recombination time the quantum confinement effect is negligible and the temperature dependency of the material (device) will resemble that of a bulk material. Region 2 is when the band profile of the quantum well becomes more flat and the effective height of the well is increased. Due to increased quantum well effective height, the carriers take longer to escape from the wells. If the escape time of carriers from the well becomes comparable to the recombination time, the dark current generated in the SCR is insensitive to applied voltage as in region 2. If the temperature drops while the condition of region 2 holds (recombination time being comparable to escape time from the wells), the dark current will become less sensitive to

temperature changes as depicted by closely packed dark current plots in region 2. In region 3 the applied voltage has overcome the barrier potential and the flat band condition has been reached. At flat band condition suddenly large amounts of diffusion current flows and the dark current in the SCR (quantum well region) becomes negligible. Therefore quantum well effect is again negligible in region 3 and the temperature dependency of the dark current of the material resembles that of a bulk material.

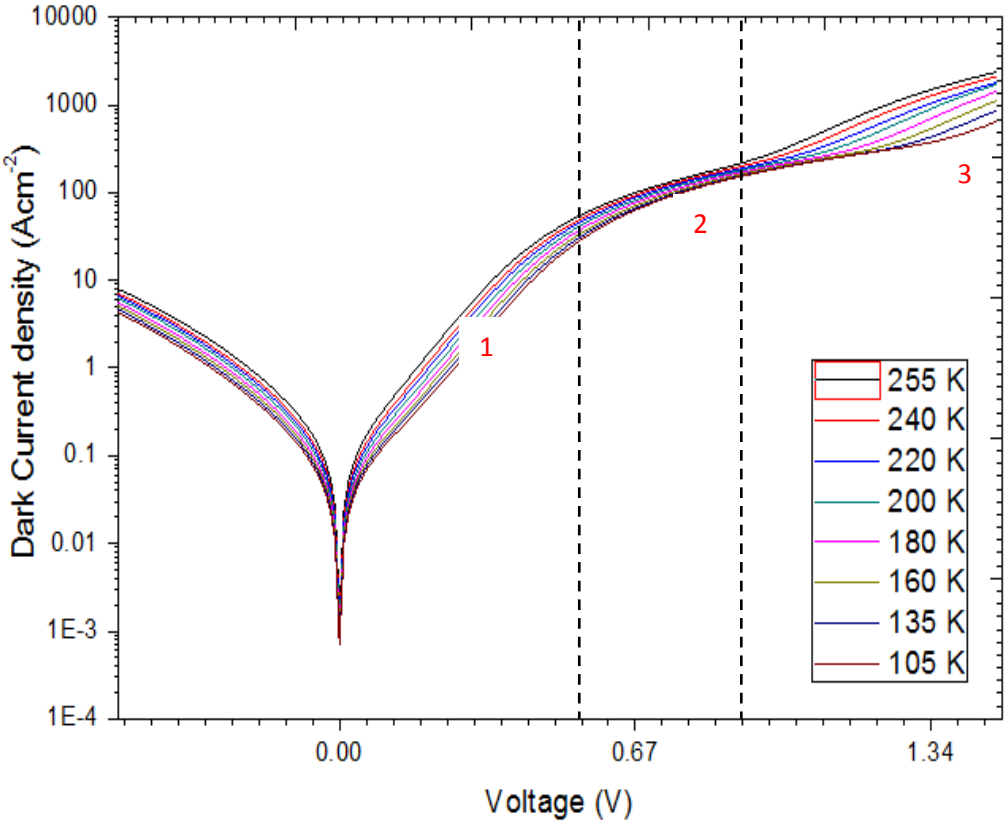

Figure 4.20: Temperature dependency of dark current density of a $Ga_{1-x}In_xN_yAs_{1-y}$ MQWs solar cell (VN1585) with N% composition of 1.0 %.

To further study the carrier process in quantum well region with temperature changes the spectral response of MQWs solar cells is studied with temperature. The spectral response of a MQWs solar cell (VN1585) with relatively shallower wells was compared to that of a MQWs solar cell ASN3138 with deeper wells. Figure 4.21 and 4.22 show the spectral response of VN1585 and ASN3138 with temperature ranges between 15 °C-40 °C. The spectral response of VN1585; figure 4.21 shows a slight increase in the peak of photogenerated current in quantum well region as well as a red shift due to bandgap narrowing as the temperature increases. The latter increase in response can be attributed to thermal assisted escape of carriers from the quantum wells. The result (figure4.21) shows that the spectral short circuit of MQWs with shallow wells increases with increasing temperature.

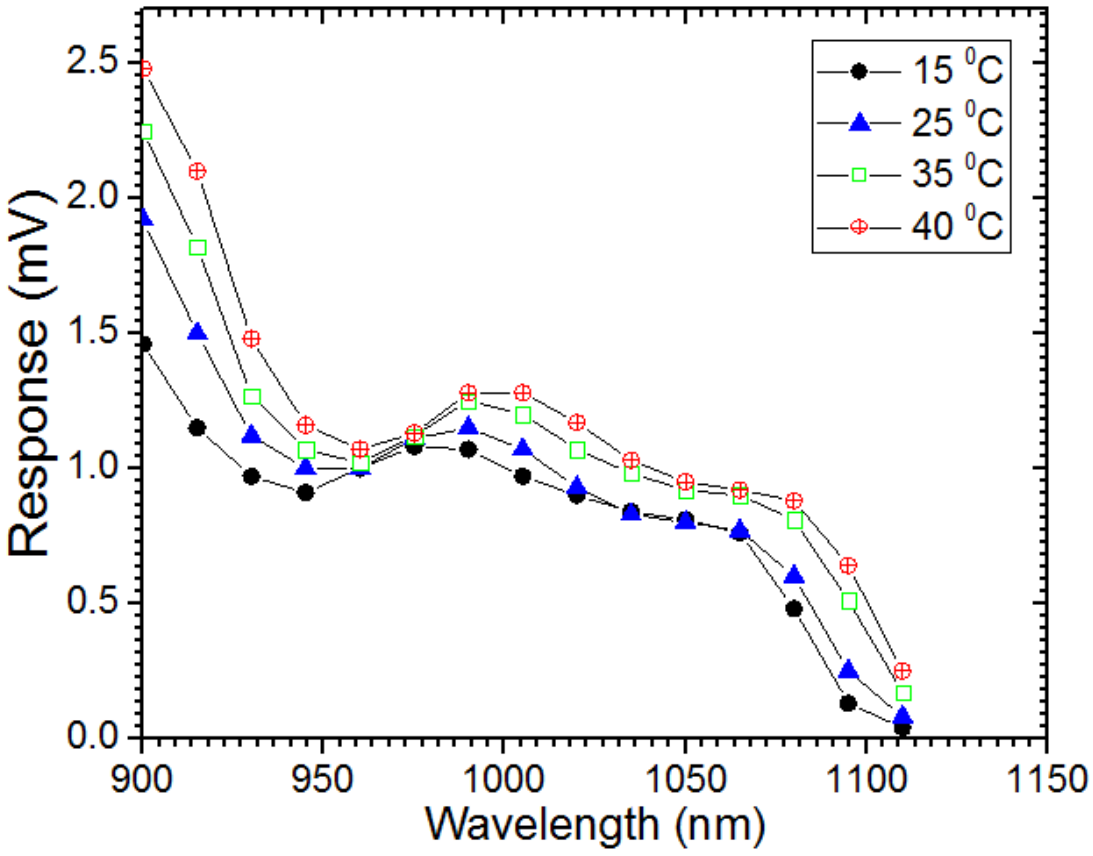

Figure 4.21: Temperature dependency of the spectral response of $Ga_{1-x}In_xN_yAs_{1-y}$ MQWs solar cell (VN1585) with shallower QWs (N% =1%).

Figure 4.22 shows the spectral response profile of ASN3138, which has deeper and many wells compared to VN1585, from 925 nm to 1110 nm (QWs region). The response in MQWs drops as temperature increases which is the reverse effect of what was observed with the response of a MQWs solar cell with relatively shallower wells (VN1585). As the quantum wells become deeper the escape time of carriers increases and more carriers recombine in the wells effectively increasing recombination current which manifest as a reduced photoresponse. As the temperature increases the conduction band becomes more populated with carriers majority of which recombine as the carriers cross the quantum well region. The thermal assisted escape of carriers is dominated by the carrier recombination inside the well and the effect is exacerbated with increasing temperature as more and more carriers populate the conduction band. The results show that for MQWs device with deeper wells the recombination in the wells may dominate resulting in decreasing photoresponse with increasing temperature. In summary, the results show that the responsivity of the MQWs solar cells to temperature depends largely on the competing process of recombination and escape of carriers from quantum wells, which vary from system to system depending on the design of the wells.

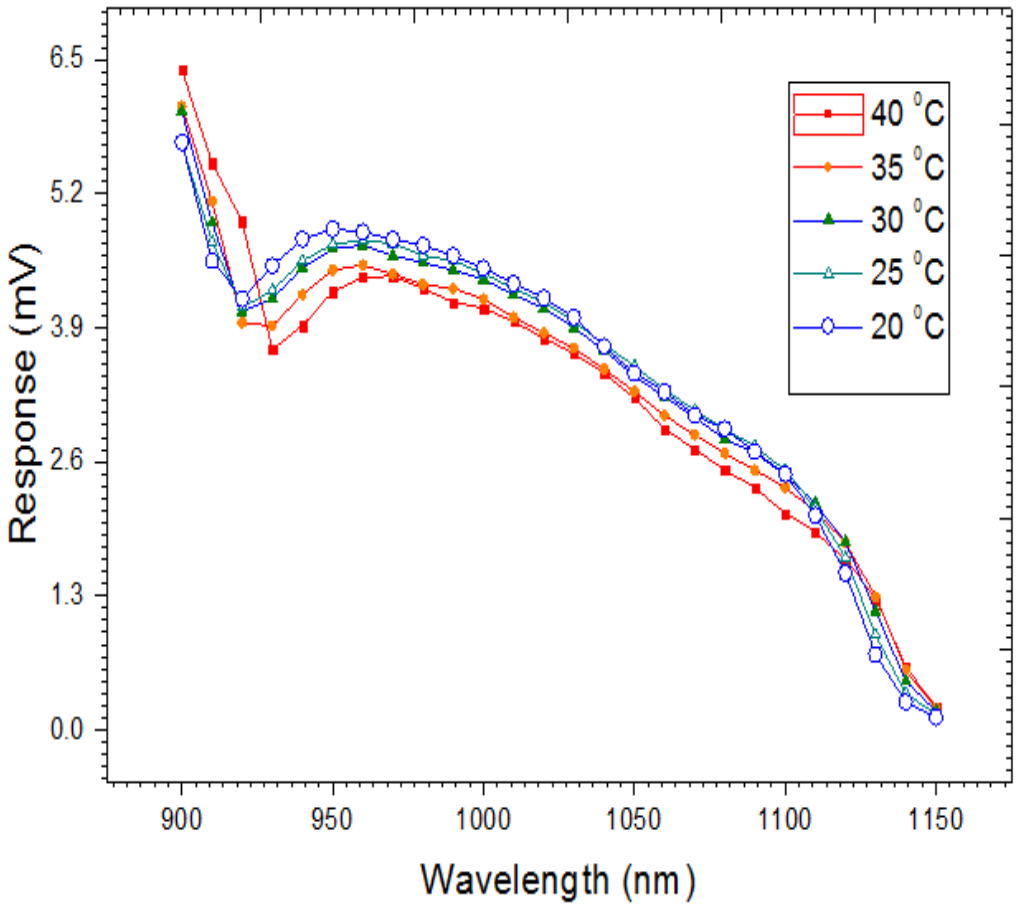

Figure 4.22: Temperature dependency of the spectral response of $Ga_{1-x}In_xN_yAs_{1-y}$ MQWs solar cell (ASN3138) with deeper QWs (N% 1.6 %).

4.4.7 Performance at different radiation levels

In this section the results for response of GaInNAs MQWs to radiation levels is reported. Figure 4.23 shows AM1.5G characteristics of MQWs solar cell-VN1585 with varying irradiance. The variation is linear within experimental error, considering the 20 % fluctuation across the collimated beam of the source of light used.

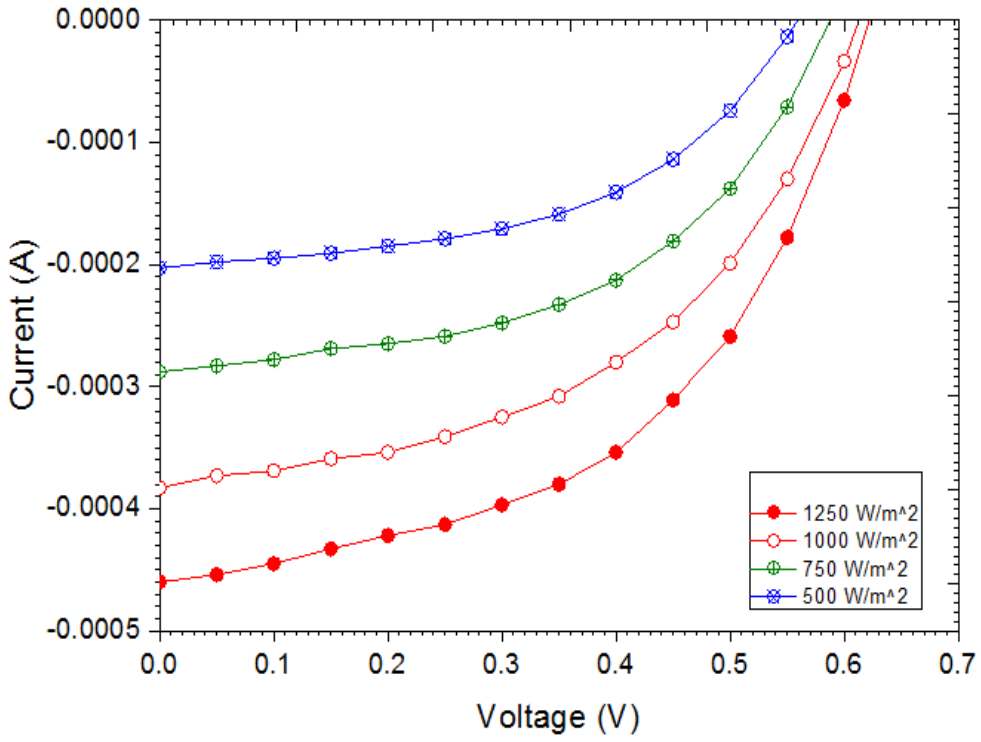

Figure 4.23: I-V characteristics of a $Ga_{1-x}In_xN_yAs_{1-y}$ MQWs solar cell (VN1585) QWs solar cell under the AMG1.5 simulator spectrum at different intensity levels.

In order to probe the direct response of MQWs to radiation levels, light at different intensity levels was dispersed by a monochromator. This was achieved by varying the intensity of tungsten halogen lamp incident on the monochromator entrance by a condenser convex lens. The latter process involves changing the position of monochromator lens; therefore the method is limited by the monochromator aperture admittance also known as the *F* number. Over the small range of intensities achieved the photo-generated current of the best MQWs solar cell VN1585 increases with intensity, across all wavelengths including the MQW region as shown in figure 4.24 (i) and (ii). The intensity levels indicated in the legend of figure 4.24 were measured at the monochromator entrance before the light dispersion. From observation of the response profiles at different intensities, it appears as the responsivity in the QW region is proportional to that of the bulk region, however normalising the spectral response profiles as shown in (figure 4.24 (ii)), clearly shows that in the quantum wells region (930 nm -1030 nm), the photoresponse level is higher than for the bulk region. The excitons resonance

manifesting as sharp peaks in the response profiles (labelled 1 and 2), gets stronger with increasing radiation levels. The latter result shows that quantum wells have a higher radiative efficiency compared to a bulk material.

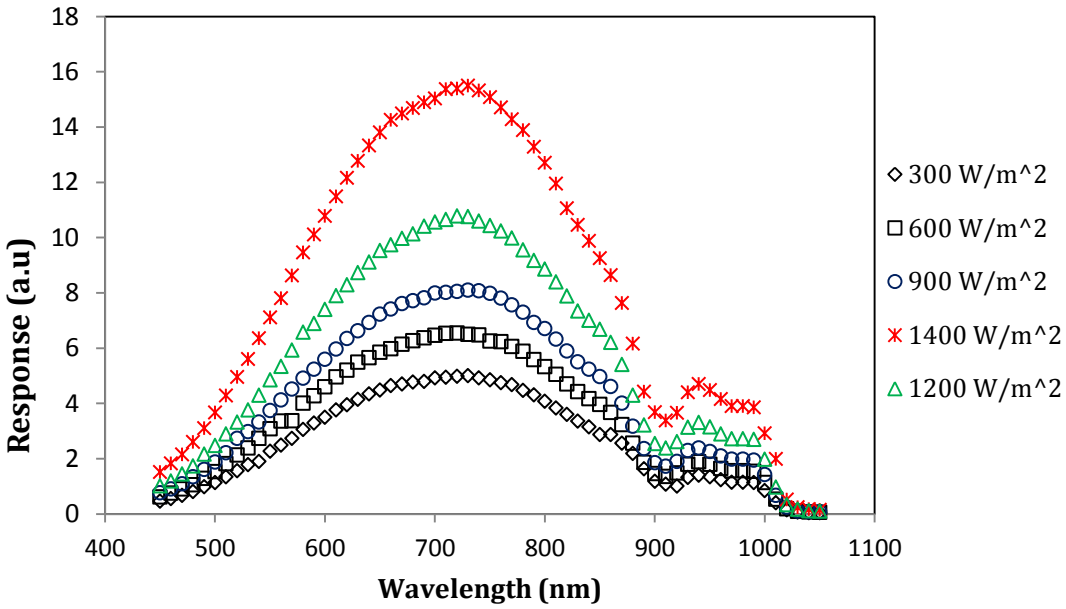

(i)

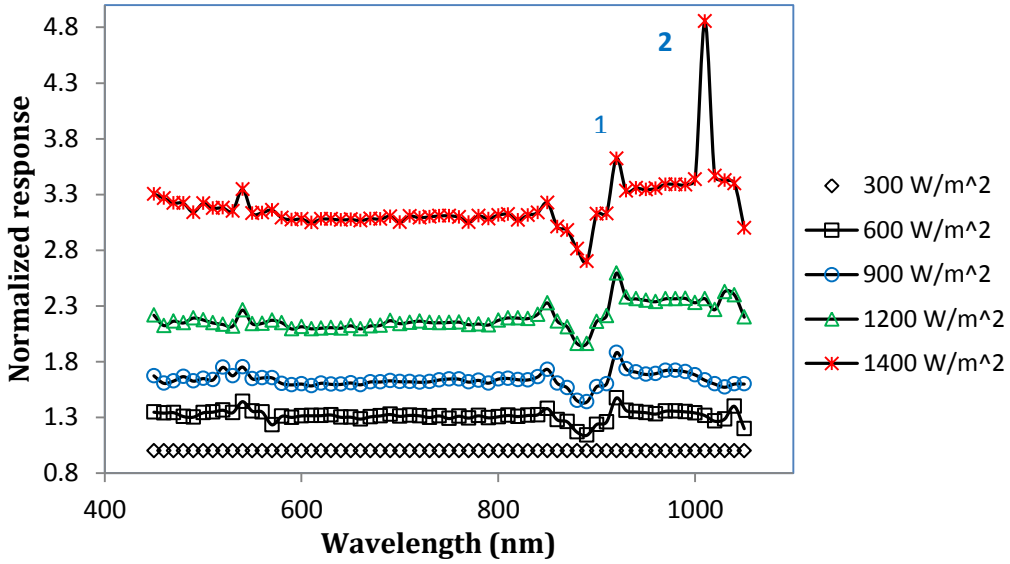

(ii)

Figure 4.24: The dependence of; (i) the spectral response of $Ga_{1-x}In_xN_yAs_{1-y}$ MQWs solar cell (VN1585) with shallower QWs (N% =1%) on radiation level. (ii) the normalised response with radiation level.

Figure 4.25 shows maximum power of MQWs solar cell (VN1585) with irradiance. The *FF* trend could not be established due to short range of intensities. It must be noted that this is very low irradiance level compared to concentrator levels. The behaviour of AlGaAs/GaAs MQWs at elevated temperatures had been studied before by [5], and no difference in responsivity of both short circuit current and open circuit voltage was found.

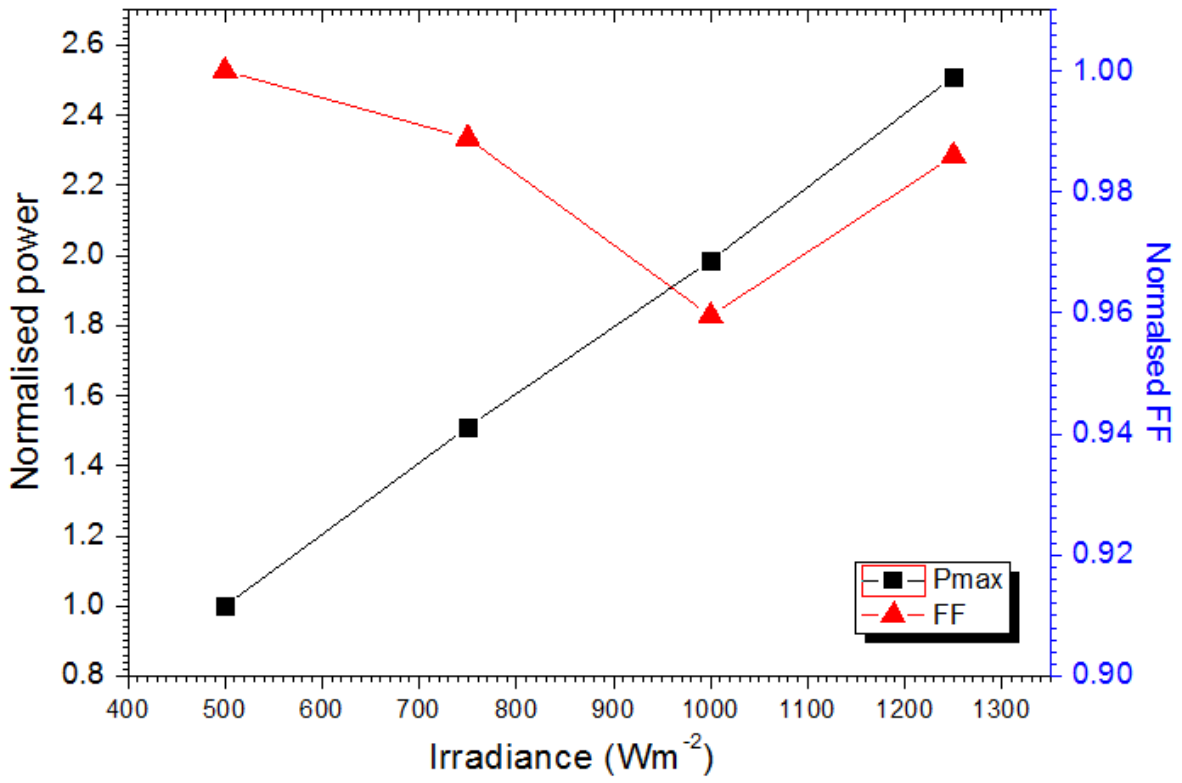

Figure 4.25: The dependence of maximum power and FF of GaInNAs solar cell (VN1585) on AMG1.5 simulator spectrum at different intensity levels.

4.5 n-i-p-i solar cells

4.5.1 Device structures

The n-i-p-i solar cells studied was a GaAs n-i-p-i cell with three repeat layers and a GaInNAs/GaAs n-i-p-i cell with nine repeat layers as shown in figure 4.25 (i) and (ii) respectively. Both devices were grown at Tampere University of Technology by a solid source MBE with RF plasma source for atomic nitrogen. Both devices had no antireflection

coating applied but a 40 nm $Al_{0.89}Ga_{0.11}As$ window layer was grown on top of the n-type layer to reduce surface recombination. In addition a 200 nm thick highly doped n-type contacting layer was grown in all devices.

Material	Thickness (nm)	Doping
n-type GaAs	200	5.0E+18
n-type $Al_{0.8}Ga_{0.2}As$	40	2.0E+18
n-type GaInNAs	100	2.0E+17
p-type GaInNAs	100	2.0E+17
n-type GaInNAs	100	2.0E+17
p-type GaInNAs	200	2.0E+17
n-type GaInNAs	200	2.0E+17
p-type GaInNAs	200	2.0E+17
n-type GaInNAs	200	2.0E+17
p-type GaInNAs	300	2.0E+17
n-type GaInNAs	300	2.0E+17
p-type GaAs	100	2.0E+17
p-type GaAs	20	2.0E+18
P+-type substrate		

(i)

Material	Thickness (nm)	Doping
n-type GaAs	200	5.0E+18
n-type $Al_{0.8}Ga_{0.2}As$	40	2.0E+18
n-type GaAs	100	2.0E+17
p-type GaAs	600	2.0E+17
n-type GaAs	1000	2.0E+17
p-type GaAs	300	2.0E+17
p-type GaAs	20	2.0E+18
P+-type GaAs substrate		

(ii)

Figure 4.26: N-i-p-i solar cell structures: (i) $Ga_{1-x}In_xN_yAs_{1-y}$, with nine repeat layers (ii) GaAs with three repeat layers.

These n-i-p-i devices had selective vertical contacts achieved by ion implants across their width. This was meant to increase vertical transport after charge separation; however this may also introduce defect densities across the entire body of the device. The solar cell devices were fabricated into circular mesa structures 1-2 mm diameters. AuGe/Ni/Au ring contact was evaporated onto the top of the device while Zn/Au contact was deposited at the bottom.

4.5.2 Spectral response

The results of the GaAs n-i-p-i devices were included in this study to demonstrate the applicability of n-i-p-i structure in photovoltaics. The spectral response of GaAs and $Ga_{1-x}In_xN_yAs_{1-y}$ n-i-p-i solar cells is shown in figures 4.27 and 4.28. The normalised spectral response plot of GaAs n-i-p-i solar cell shows a typical shape of GaAs profile shape, with a near flat spectrum between the short wavelength cut-off due to the band-gap of the window layer and a long wavelength cut-off due to the band-gap of GaAs active region, with the cell having an absorption edge of 870 nm (~1.42 eV). This confirms that the photogenerated carriers anywhere in the n-i-p-i layers are contributing to the device photocurrent.

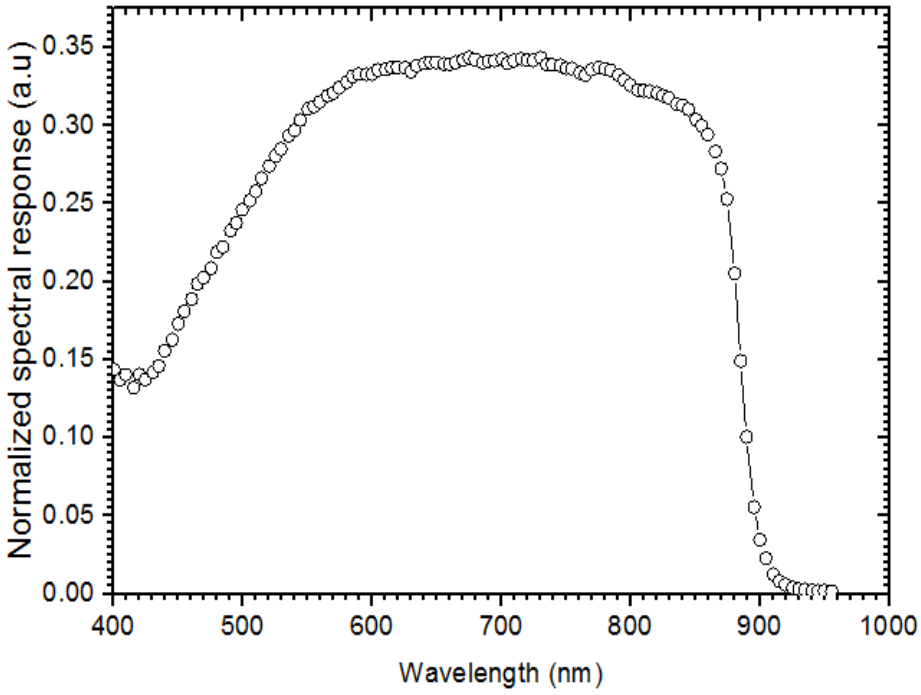

Figure 4.27: The spectral response of a GaAs n-i-p-i solar cell under AM1.5G simulator spectrum set to 1000 W/m^2 .

The relative spectral response of the $Ga_{1-x}In_xN_yAs_{1-y}$ n-i-p-i solar cell shows the contribution of GaInNAs up to 1100 nm corresponding to ~1.1 eV. The lower response at the

longer wavelength is probably due to the lower layers of the n-i-p-i not contributing to the photogenerated current. This could happen as the vertical selective contacts of the device were achieved by ion implantation across its width. If the ion implants could not reach deeper parts of the device, the photogenerated carriers at the bottom will tend to recombine before being collected. In that case the device will behave as a thin solar cell absorbing strongly at the surface and being transparent to the longer wavelength photons.

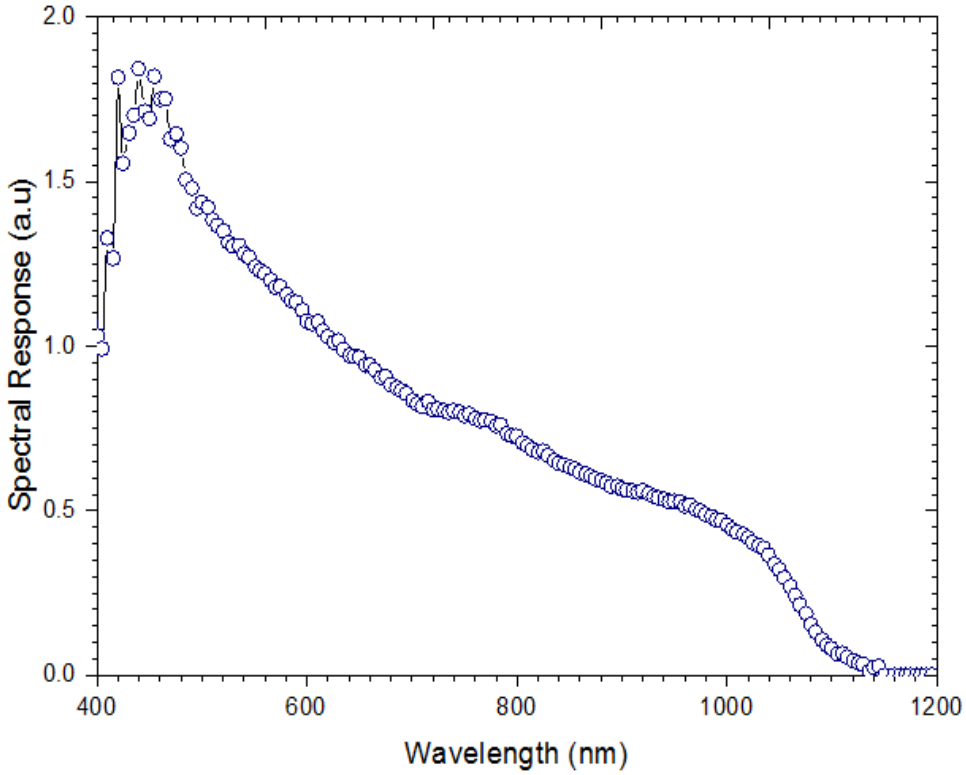

Figure 4.28: Spectral response of a GaAs n-i-p-i solar cell with nine repeat layers.

4.5.3 Dark Current I-V measurements

Figure 4.29 shows the dark J-V plots for a GaAs conventional solar cell (TS0419) (solid triangles) and GaAs n-i-p-i solar cell (empty circles) as well as $Ga_{1-x}In_xN_yAs_{1-y}$ n-i-p-i (empty triangles). The saturation current density ((J_{sc}) of the $Ga_{1-x}In_xN_yAs_{1-y}$ and the GaAs n-i-p-i solar cells measured at -0.2 V is $3x10^{-3}$ and $1x10^{-2}$ Acm^{-2} as seen on figure 4.29.

These values of saturation current exhibited by the n-i-p-i devices is more than three order of magnitude compared to the saturation current density of the GaAs ($4x10^{-6}$ Acm^{-2}) measured at the same voltage value (-0.2 V). These high values of dark current in the n-i-p-i devices explain the low (V_{oc}) of these n-i-p-i solar cells. The ideality factors measured from the dark I-V characteristics varied from 3.35 to 5.02 for GaAs and $Ga_{1-x}In_xN_yAs_{1-y}$ n-i-p-i solar cells as shown in table 4.7. The high dark current density observed in the n-i-p-i devices does not come as a surprise as the repeat layers increase the effective width of the depletion region. Similarly the many interfaces increase defects which increase the non-radiative recombination current. However the unexpected result was of the GaAs n-i-p-i with 3 repeat structure to show higher cark current than the $Ga_{1-x}In_xN_yAs_{1-y}$ n-i-p-i with 9 repeat layers. This may imply structure related defects more than material quality, especially due to the device having had ion implantation across them. However further measurements could not be carried out on the $Ga_{1-x}In_xN_yAs_{1-y}$ n-i-p-i structure as it got burnt before further tests.

Device design	**n_1**	**n_2**
GaInNAs n-i-p-i	3.35	4.50
GaAs n-i-p-i	5.01	5.01

Table 4.7: Ideality factors for the GaAs and $Ga_{1-x}In_xN_yAs_{1-y}$ n-i-p-i solar cells under study.

The high ideality factors imply that their dark current is dominated by non-radiative recombination or presence of other transport mechanism such as tunnelling. While the ideality factors shown by these devices are admittedly higher than typical values, it is not uncommon for n-i-p-i structures. Recently demonstrated GaAs n-i-p-i solar cells by C.D.

Cress et al [31] exhibited dark currents of ideality factors between 1.88 and 4.45, for annealed and asgrown n-i-p-i structures respectively.

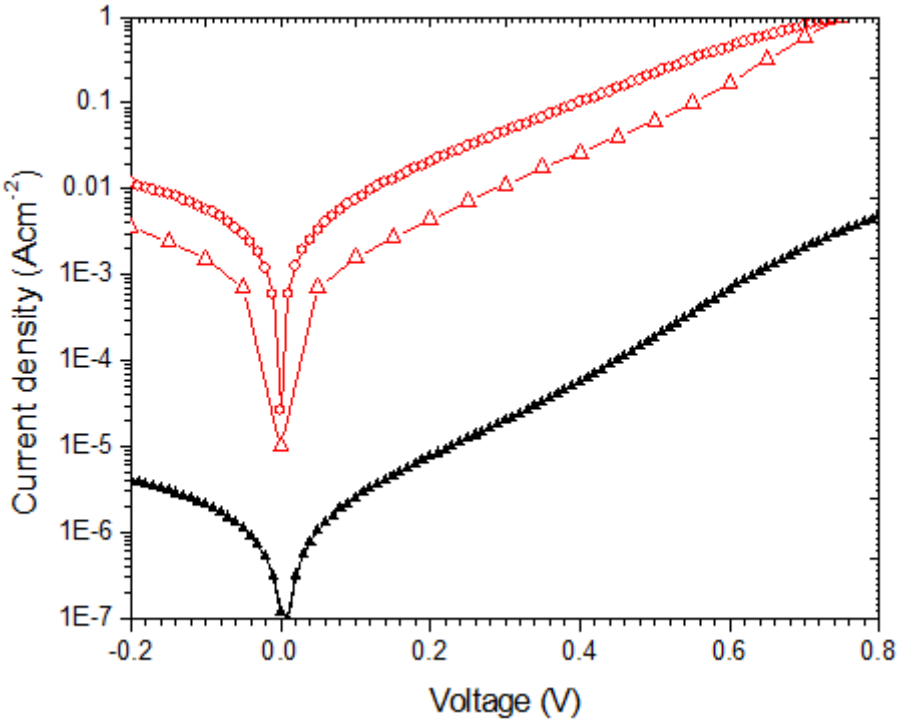

Figure 4.29: Dark current density of the GaAs and $Ga_{1-x}In_xN_yAs_{1-y}$ n-i-p-i solar cells under study. Solid triangles; GaAs conventional p-n junction (TS0419): Empty triangles; GaInNAs n-i-p-i and Empty circles; GaAs n-i-p-i solar cells.

4.5.4 AM1.5G characterisation

The AM1.5G x1sun results of the n-i-p-i solar cells are shown in figure 4.30. The figures of merit for the GaAs n-i-p-i were: J_{sc}=16.0 mA/cm^2, V_{oc}=0.33 V, *FF*=54 % and η=2.2. The $Ga_{1-x}In_xN_yAs_{1-y}$device had a very low J_{sc} of 4.2 mA/cm2 and a V_{oc} of 0.19 V. The low J_{sc} can be explained by the shape of the spectral response plot which shows very low collection at longer wavelengths, which as explained in section 4.4.2. However a V_{oc} of 0.33 V and 0.2 V both in the GaAs and $Ga_{1-x}In_xN_yAs_{1-y}$ n-i-p-i is typical of the n-i-p-is. The n-i-p-i structure in photovoltaics was in the earlier years modelled by Wagner and Leburton and they

commented that despite its supreme carrier extraction there was a foreseen problem of an inherent low V_{oc} [32] especially in thin layers n-i-p-i structures (superlattices), which stems from a nearly depleted structure due to repeated space charge layers. There is no apparent solution to the latter problem besides a trade-off between current and voltage by optimising number and thickness of layers. Results show that the V_{oc} varies to some extent with the fabrication technique and the quality of the selective contacts [31].

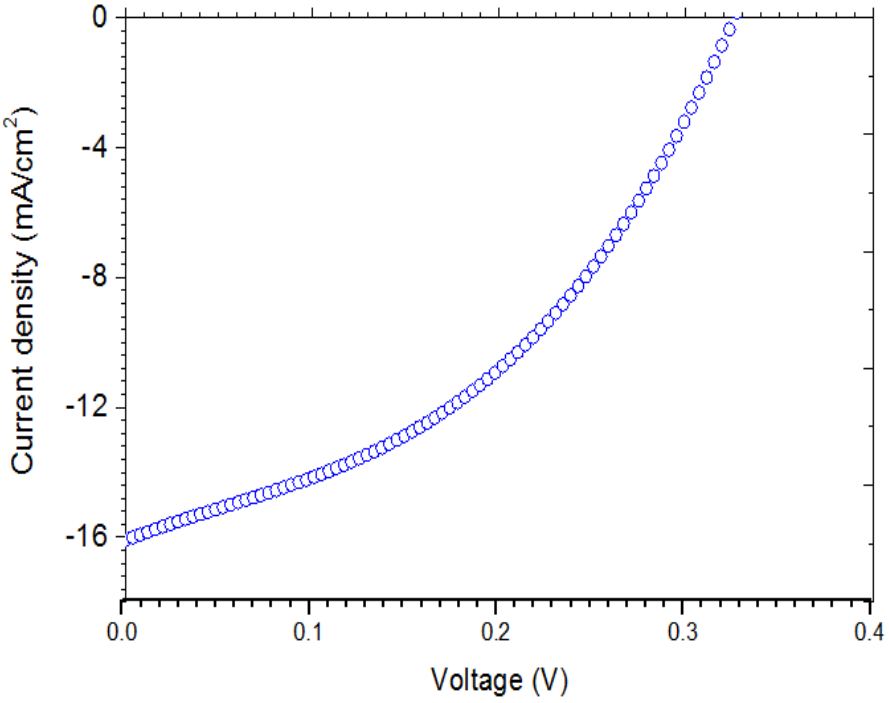

Figure 4.30: AM1.5G characteristics of a GaAs n-i-p-i solar cell.

4.5.5 Temperature dependence of maximum power

The effect of lowering temperature as discussed in section 4.1 is reducing short-circuit current and increasing V_{oc}. The temperature response of the GaAs n-i-p-i solar cell AM1.5G characteristics is shown in Figure 4.31. These plots do not show the normal current-voltage trade-off typical of a solar cell. Simultaneous increase in J_{sc} and V_{oc}, is observed between 240°C and 280° C. This shows that due to excessive dark current in the n-i-p-i devices, the

effect of the reduction of dark current as the n-i-p-i device cools can be more than the accompanying effect of bandgap widening**.** The latter effect explains the strong temperature coefficient of efficiency exhibited by the n-i-p-i solar cells. Despite huge gain of efficiency upon cooling the n-i-p-i solar cells, it would not be of any benefit in photovoltaics as cooling systems can be quite expensive to install together with solar cell devices.

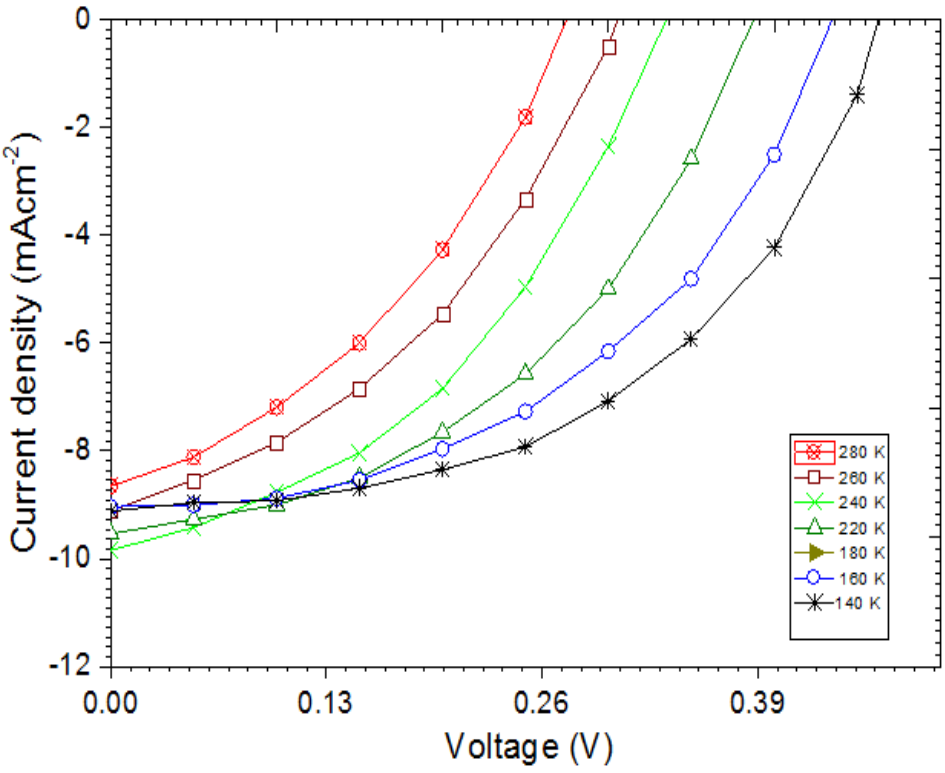

Figure 4.31: Temperature dependence of I-V characteristics of a GaAs n-i-p-i solar cell illuminated by the AM1.5G simulator spectrum.

Figure 4.32 is the plot of the normalised maximum power versus temperature. The estimated temperature coefficient is -13.1 % $x10^{-3}$ K^{-1}, which is the highest temperature coefficient observed in all the solar cell studied.

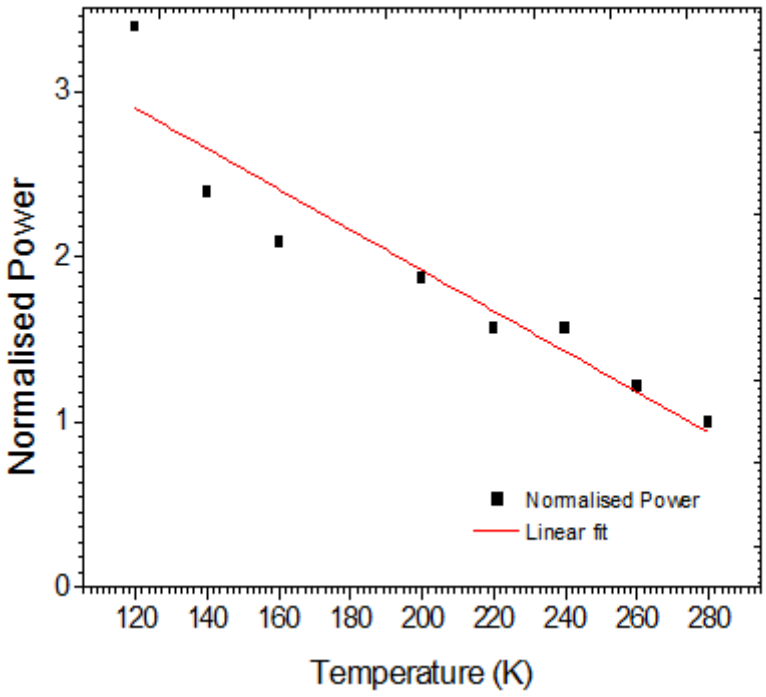

Figure 4.32: normalised maximum power versus temperature for a GaAs n-i-p-i solar cell under study.

The dark current J-V characteristics of the GaAs n-i-p-i solar cell, in figure 4.33 shows an expected trend of reducing current as the temperature reduces. However it can be seen from the I-V characteristics as indicated by dotted arrows that, at relatively higher temperatures the J-V plots show a gentle slope across the entire range of applied voltage. The latter suggest that the non-radiative recombination current dominates the total dark current even at flat band conditions (higher voltages). This high non-radiative recombination is expected in the n-i-p-i devices because of repeated layers of alternating doping in the n-i-p-i structures that result in the overall increase of the depleted region (SCR). At lower temperatures the plots show two regions of a gentle and a steeper slopes. Before the regime of carrier localisation, mobility of carriers increases with reducing temperature. As the mobility of carriers increases the non-radiative recombination process via traps is reduced. For a device that is strongly dominated

by non-radiative recombination, the latter reduction will be significant as shown by the emergence of radiative recombination slope at low temperatures.

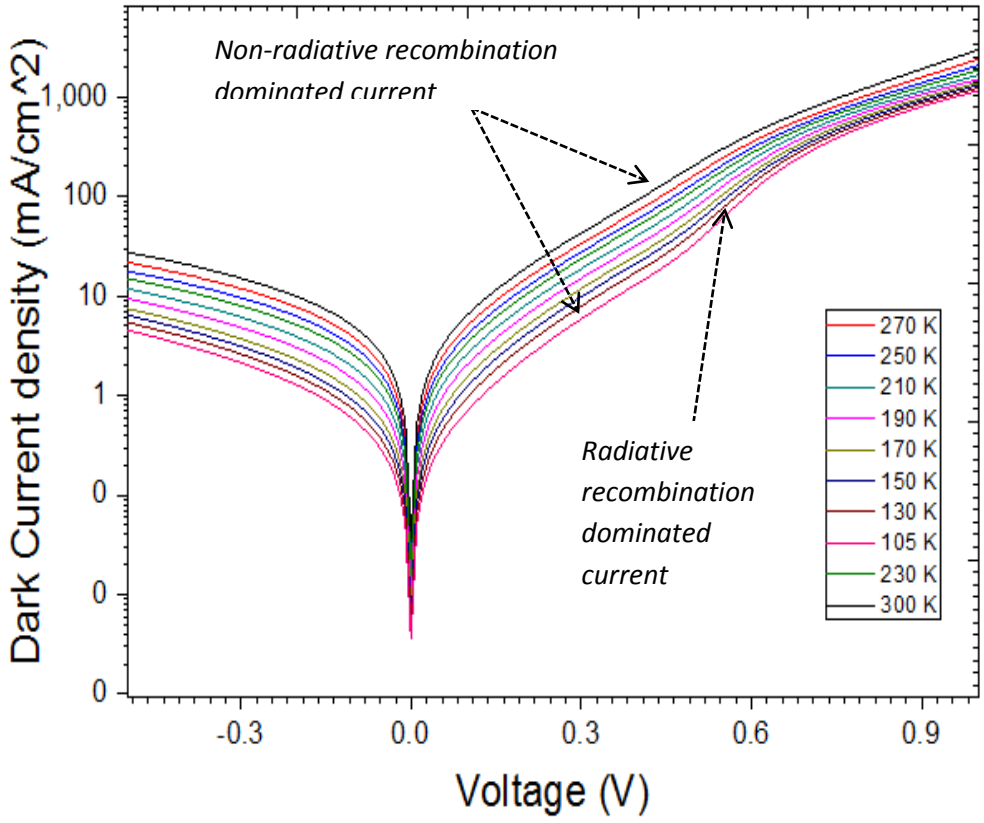

Figure 4.33: Temperature dependency of dark current density of the GaAs n-i-p-i solar cell under study.

4.5.6 Performance at different radiation levels

The testing of the n-i-p-i with radiation levels shows a good gain of voltage as radiation level increases as shown in figure 4.34. The *FF* plotted together with maximum power shows that both the figures of merit (figure 4.35), improve with the radiation level. This shows the possibility of n-i-p-is performing well at concentrator levels of irradiation.

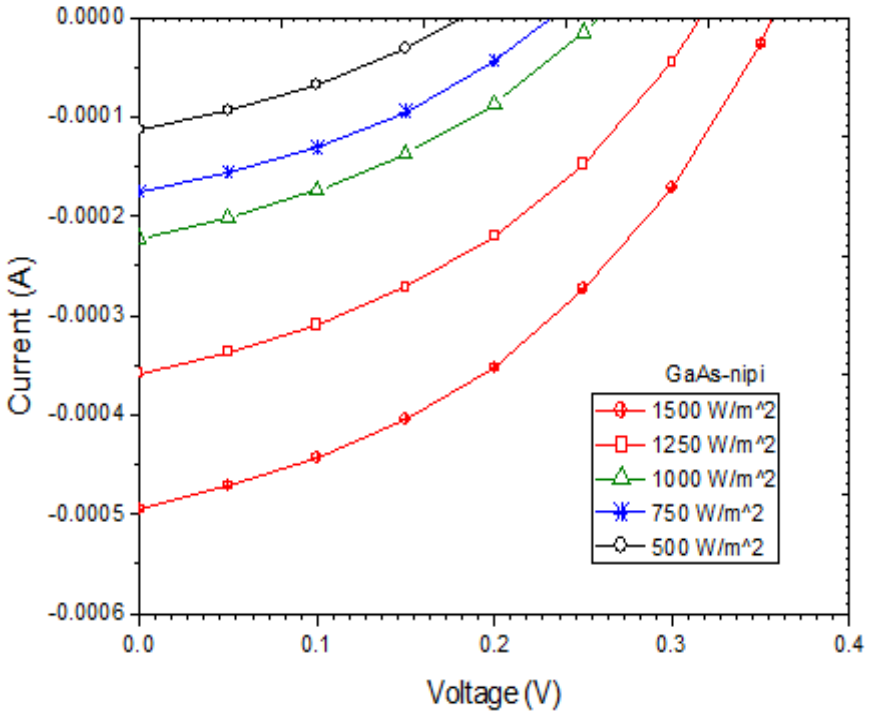

Figure 4.34: I-V characteristics of a GaAs n-i-p-i solar cell at different intensity levels of an AMG1.5 simulator spectrum.

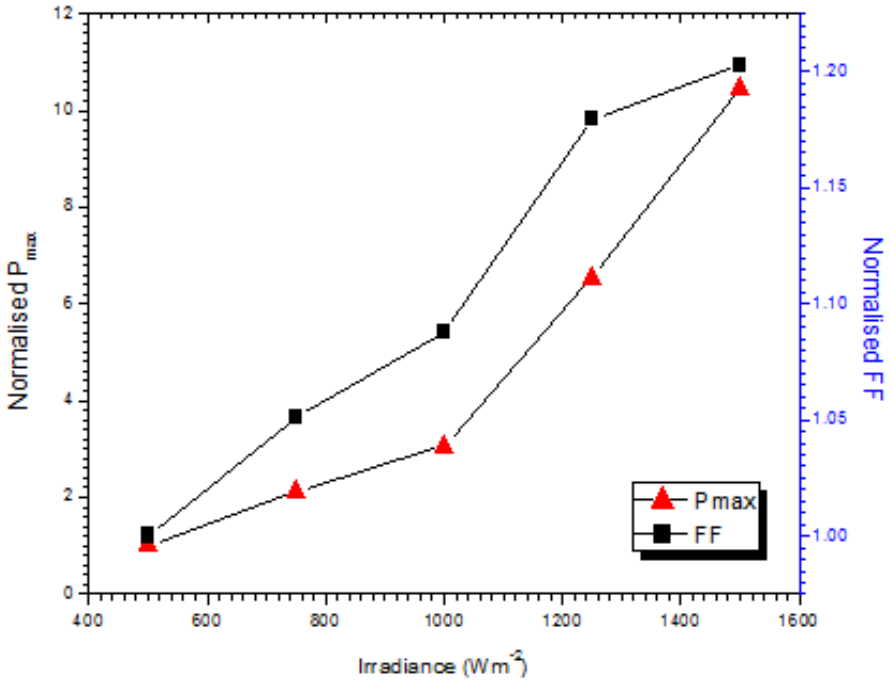

Figure 4.35: The dependence of maximum power and FF of GaAs n-i-p-i solar cell on the AM1.5G spectrum at different intensities.

4.6 Effect of different designs on performance of the solar cell devices

4.6.1 Trapping effect

The trapping effect of each device was deduced from hyperbolic logarithmic plots of current density with temperature. In the SCR the generation-recombination current is given by;

$$J_{0,scr} = \frac{qn_{iW_d}}{\tau_{scr}} \tag{4.22}$$

where, and q,n_i, W_d and τ_{scr} are electronic charge, intrinsic carrier density, depletion width thickness, average recombination lifetime in the SCR respectively.

In case of a single trap or a dominant trap, the recombination lifetime in the SCR can be estimated as;

$$\tau_{SC} = \tau_{p0} exp\left(-\frac{E_t + E_i}{kT}\right) + \tau_{n0} exp\left(\frac{E_t + E_i}{kT}\right) \tag{4.23}$$

where, τ_{n0}, τ_{p0} , E_t and E_i are, electron capture lifetime, hole capture lifetime, trap energy level, intrinsic Fermi level respectively.

When logarithm of dark current density at a specific voltage (corresponding to where the SCR current dominates, in this analysis 0.2 V was chosen) is plotted against the inverse of temperature, the slope of the plots (typical plots are straight line), show the degree of trapping in the device, and can be used to approximate the energy levels of dominant traps. The weak trapping effect will have a near flat slope.

Although the accuracy of the method is limited to a single trap or a single dominant trap in the material, the comparison of the slopes of the plots can reveal relative quality of each device. The results are used to probe any design or material related trends.

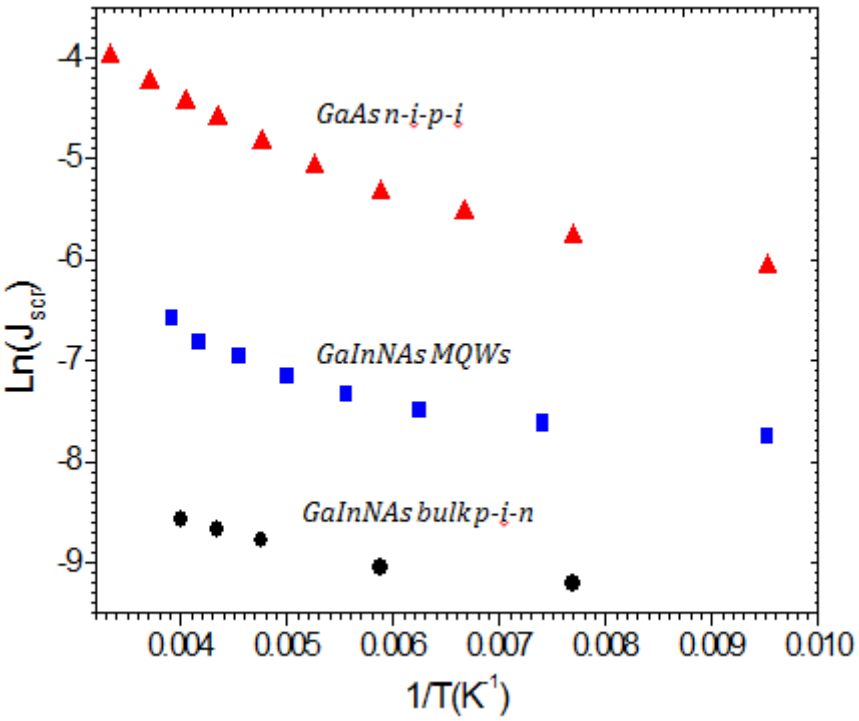

Figure 4.36: Trapping strength in solar cells of different designs studied.

The slopes of the plots in figure 4.36 could not be fit into a linear plot as anticipated; hence the trap levels could not be deduced from the slopes of the plots. However from the slopes in the region between 0.004 and 0.006, the relative degree of the trapping in each junction can be deduced. The n-i-p-i with the steepest plot has the highest trapping effect followed by MQWs and lastly the pin with a near flat slope has the lowest trapping effect. These results are in agreement with the dark currents observed in previous chapter.

4.6.2 Recombination lifetime

The average recombination lifetimes (τ_{avg}) deduced from a fit to dark current density data is shown in table 4.8. The lifetimes show a design related trend, with the p-i-n bulk solar devices exhibiting the longest recombination times, and all the p-i-n MQWs solar exhibit recombination times that are shorter than the p-i-n devices. The dark current density data for the n-i-p-i solar cells could not be used to deduce the average recombination times in the

devices, as it could not fit into either the SNS model (4.17) or the generation-recombination equation 4.21. Observation of data on table 4.4 reveals a correlation between the shunt resistance and the average recombination time (the smaller the shunt resistance the shorter the recombination lifetime), therefore it can be assumed the n-i-p-i design has the shortest recombination lifetimes.

Device design	$\mathbf{n_1}$	$\mathbf{n_2}$	$\mathbf{R_{sh}}$ **(kΩ)**	$\boldsymbol{\tau_{avg}}$ (ps)
GaInNAs_"pin2"	1.75	1.75	23	500
GaInNAs_"pin1"	2.30	2.30	8.4	150
GaInnAs MQWs_VN1585	2.51	3.05	44	65
GaInNAs MQWs_ASN3138	2.13	6.79	0.33	14
GaInNAs_MQWs_ASN2605	2.78	7.18	0.33	0.4
GaInNAs_ MQWs_ASN2604	5.57	13.05	0.07	13
GaInNAs_MQWs_ASN3134	8.72	8.72	2.4	0.5
GaInNAs n-i-p-i	3.35	4.50	0.07	-
GaAs n-i-p-i	5.01	5.01	0.002	-

Table 4.8: Ideality factors, shunt resistances and average recombination lifetimes for the solar cell studied.

4.6.3 Temperature coefficients

The normalised maximum power against temperature for all devices in the near RT ranges is shown in figure 4.37. The temperature coefficients for the solar cells were calculated in two ranges as shown in table 4.9. The n-i-p-i solar cells show the highest temperature coefficient which ranges from -13.1 K^{-1} to -17 K^{-1}. MQW show the lowest temperature coefficients which exhibited both flat and negative slopes. The p-i-n devices show temperature coefficients values between those of n-i-p-i and MQWs, except for the -0.5 x 10^{-3} K^{-1} shown

by “pin2” for a temperature range of 300 K and 200 K, which was assumed to be an anomalous result.

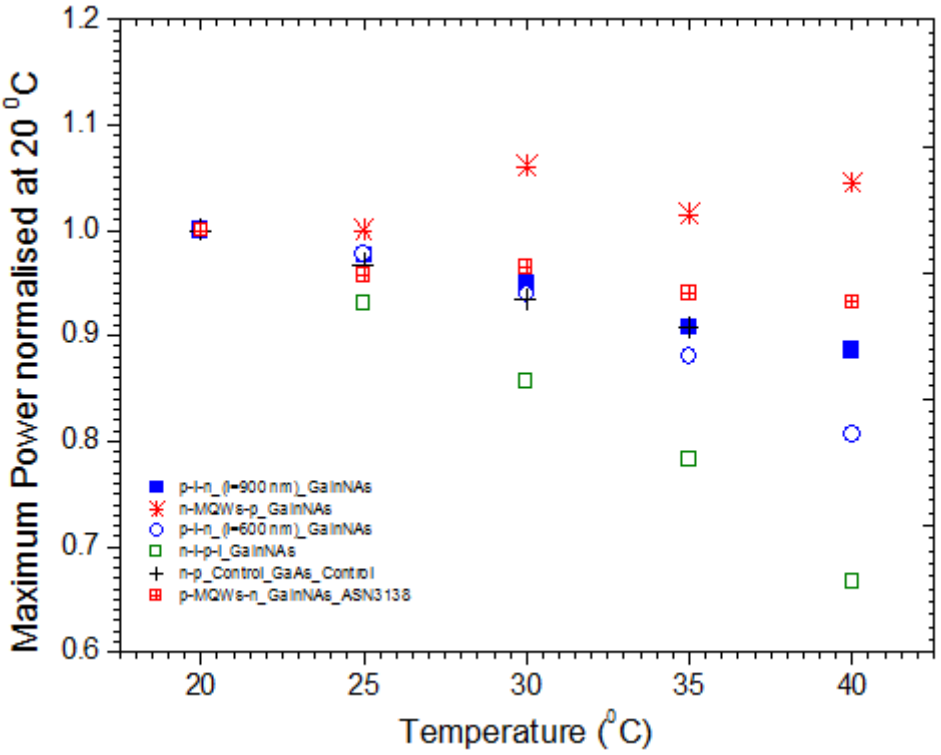

Figure 4.37: Temperature dependence of maximum power of solar cells of different designs.

Device design	**Material**	**Temperature Coefficient (X10^{-3} K^{-1})**	
		Long range (100 K-300K)	Near RT (10 °C -40 °C)
n-i-p-i	GaAs	-13.1	-17
p-i-n (“pin1”)	$Ga_{1-x}In_xN_yAs_{1-y}$	-	-9.5
p-i-n(“pin2”)	$Ga_{1-x}In_xN_yAs_{1-y}$	-0.5	-5
MQW(VN1585)	$Ga_{1-x}In_xN_yAs_{1-y}$	+2.9	+2.5
MQW(ASN3138)	$Ga_{1-x}In_xN_yAs_{1-y}$	-	-3.5

Table 4.9: Temperature coefficients of maximum power (or efficiency) of the solar cells under study.

4.7 Conclusion

The performance of the dilute nitride solar cell devices of different designs have been studied under different operation conditions. Room temperature dark current shows that all dilute nitride solar cells generate much higher dark current than the conventional (p-n) GaAs junction solar cells. The dark current density in the dilute nitride solar cells increases with increasing nitrogen composition. In the dilute nitride solar cells the total dark current density can be represented by the generation-recombination current in the intrinsic region alone (the dark current generated by

$Ga_{1-x}In_xN_yAs_{1-y}$).

The bulk p-i-n dilute nitride solar cell generates less dark current which also has a lower ideality factor compared to that of MQWs solar cells. The MQWs dilute nitride solar cells exhibit dark current with anomalously high ideality factors. The n-i-p-i solar cells exhibit highest dark current density of all the devices, which was an expected as the n-i-p-i structures consist of several p-n junctions, hence increased size of depletion layers.

The carrier trapping effect of the devices is strongest in the n-i-p-i solar cells and least in the bulk p-i-n solar cells. Despite the highest dark current observed in the n-i-p-i solar cells, the V_{oc} of the n-i-p-i solar cells increases markedly with increasing light intensity (figure 4.34) compared to those of p-i-n bulk and MQWs (figure 4.11-4.14 and 4.23). The performance of the dilute nitride n-i-p-i solar cells at elevated radiation levels still needs more detailed study for possibility of using n-i-p-i in concentrator photovoltaics.

The p-i-n design (p-i-n bulk and p-i-n MQWs) show lower temperature coefficients than the GaAs conventional (p-n junction) solar cell. The p-i-n MQWs dilute nitride solar cells are less sensitive (lower temperature coefficient) compared to the bulk p-i-n dilute nitride solar cells.

The spectral response of all the dilute nitride solar cells shows the absorption due to the dilute nitride (beyond GaAs cut-off wavelength). Due to stronger electron trapping compared to holes in dilute nitride alloys, the response of p on n design is different from that of n on p design in the p-i-n MQWs devices. The response by the dilute nitride MQWs show different response absorption of the dilute nitride is smaller in the MQWs region.

References

[1] J. Nelson, "The physic of solar cells", (Imperial College Press, 2003), p 146. [2] B. G. Streetman, S. K. Banerjee **"Solid state electronic devices,"** (Prentice Hall, 2006).

[3] A. Erol, [Ed], "**Dilute III-V Nitride Semiconductors and Material systems Springer Series in material science",** (Springer, 2008).

[4] M. Ballard; *"Electrical and Optical properties of MQWs solar cells under elevated temperature and illumination level"* PhD. thesis, 'Imperial College of London, (1999).

[5] D. J. Friedman, A. J. Ptak, S. R. Kurtz, J. F. Geisz, *"Analysis of Depletion-Region Collection In GaInNAs Solar Cells"* 31st IEEE Photovoltaic Conference, February 2005.

[6] N. Miyashita, Y. Shimizu, N. Kobayashi, Y. Okada, and M. Yamaguchi, *"Fabrication of GaInNAs-based solar cells for multi-junction tandem solar cells*" IEEE, 2006.

[7] D. J. Friedman, J. F. Geisz, S.R. Kurtz, and J. M. Olson, *"1-eV GaInNAs Solar Cells for Ultrahigh-Efficiency Multi-junction Devices"* Presented at the 2nd World Conference and Exhibition on Photovoltaic Solar Energy Conversion; 6-10 July (1998).

[8] S.R. Kurtz , D. J. Friedman,R. R. King, K.M. Edmondson, and N. H. Karam, *"1-MeV Electron Irradiation of GaInNAs Cells",* to be presented at the 29th IEEE PV Specialists Conference, Louisiana, May (2002).

[9] Z. I. Alexieva, Z. S. Nenova, V. S. Bakardjieva, M. M. Milanova and H. M. Dikov, "*Antireflection coating for GaAs solar cell applications***",** Journal of Physics: Conference Series 223 ,012045, (2010).

[10] S. Kurtz, S.W. Johnston**,** J. F. Geisz, D. J. Friedman, and A. J. Ptak, *'Effect of Nitrogen concentration on the Performance of* $Ga_{1-x}In_xN_yAs_{1-y}$ *Solar Cell'*, Prepared for the 31st IEEEE Photovoltaics Specialists Conference and Exhibition, 2005.

[11] M. A. Green, K. Emery, Y. Hishikawa, and W. Warta, *"Solar Cells efficiency tables (version 36)",* Progress in Photovoltaics: Research and Publications, Progress in Photovoltaics: Research and Applications, (2010).

[12] B. Royal, "*GaInNAs/GaAs multiple quantum well solar cells*", PhD. Thesis, University of Essex, (2011).

[10] S. Kurtz, S. W. Johnston**,** J. F. Geisz, D. J. Friedman, and A. J. Ptak, *"Effect of Nitrogen concentration on the Performance of* $Ga_{1-x}In_xN_yAs_{1-y}$ *Solar Cell",* Prepared for the 31st IEEEE Photovoltaics Specialists Conference and Exhibition, 2005.

[13] D. J. Friedman, J. F. Geisz, W. K. Metzger and S.W. Johnson, *"Trap dominated minority carrier recombination in GaInNAs junctions"*, Journal of Applied Physics Vol. 83, No 4, (2003).

[14] Chi-Tang Sah, R. N. Noyce and W. Shockley, *"Carrier Generation and Recombination in P-N Junctions and P-N Junction Characteristics"*, Proceedings of the IRE, pp.1228 – 1243 (1957).

[15] J. Salinger, *"Measurement of solar cell parameters with dark forward I-V characterisation"* Acta Polytechnica Vol. 46 No. 4 (2006).

[16] S. K. Cheung and N. W. Cheung, "*Extraction of Schottky diode parameters from forward current-voltage characteristics"*, Appl. Phys. Lett. Vol **49**, pp. 85 (1986).

[17] J. Connolly, "Modelling and Optimising $GaAs/Al_xGa_{1-x}As$ multiple Quantum Well Solar Cells", PhD. Thesis, Imperial College of London.

[18] S. M. Sze, K. NG. Kwok, **"Physics of Semiconductor Devices", 3rd Edition,** (Wiley Interscience, 2006).

[19] A. Kaschner, T. Luttgert, H. Born, *"Recombination Mechanisms in GaInNAs / GaAs Multiple Quantum Wells"*, Applied Physics Letters, Vol. **78**, pp. 1391, (2001).

[20] J. F. Geisz and D J Friedman, *"111-N-V semiconductors for solar photovoltaic applications",* Semiconductor Sci, Technol. 17 No 8, 2002

[21] J. M. Shah, Y. L. Li, T. Gessmann, and E. F. Schbert, "*Experimental analysis and theoretical model for anomalously high ideality factors (n>2.0) in AlGaN/GaN p-n junction diodes"*, Journal of Applied Physics, Vol. **94**, No. 4, (2003).

[22] D. Z. J. Xu, A. N. Noemaun, J. K. Kim, E. F. Schurbet, M. H. Crawford, and D. D. Kolose, "*The origin of high dioide ideality light-emitting diodes*", Applied Physics Letters Apl Vol. **94**, pp. 081113, (2009).

[23] H. C. Casey Jr, et al., "*Dominance of tunneling current and band filling in InGaN/AlGaN double heterostructure blue light-emitting diodes."* Applied physics letters Vol **68** Issue 20, pp. 2867-2869, (1996).

[24] K. W. J. Barnham, I. Ballard, J.p. Connolly, Ekins-Daukes, B.G. Kluftinger, J. Nelson, C. Rohr, *"Quantum Well Solar Cells",* Physica E , Vol. **14**, pp. 27-36 (2002).

[25] R. Corkish and M. A. Green, *"Recombinations of carriers in quantum well solar cells"* ,Proc. 23rd IEEE Photovoltaics Specialist Conference, New York, pp. 675-689, (1993).

[26] R. Corkish and C. Honsberg, *"Dark currents in double-hetero-structure and quantum-well solar cell"*, 26th IEEE Photovoltaic Specialist Conference, Anahein, CA, 1997

[27] D. Wiston, *"Physical Simulation of Optoelectronic Semiconductor Devices",* PhD thesis, University of Colorado, 1996: http://www.simwindows.com/.

[28] R. Corkish and C. B. Honsberg, " *Simulation of GaAs/InGaAs quantum well solar cells*", retrieved from; http://solar.org.au/papers/99papers/CORKIS.pdf.

[29] G. Haarpaintner, *"Electrical Properties of multiple quanrum wells",* PhD thesis, Imperial College of London", (1995).

[30] J. G. Adams et. al., *"Recent results for single junction and tandem quantum well solar cells"***,** Prog. Photovolt:: Res. Appl: Vol. **19**, pp. 865-877, (2011).

[31] C. D. Cress, S. J. Polly, S. M. Hubbard, R. P. Raffaele, R. J. Walters: *"Demonstration of a n-i-p-i-diode photovoltaic",* Prog. Photovolt. Res. Appl., Vol **19**, No. 5, pp. 552-559, (2011).

[32] M. A. Scolum, D. V. Forbes, J. S. Mc-Natt, S. M. Hubbard: "*Epitaxial regrowth contacts for the n-i-p-i photovoltaic device",* Proc. 37th IEEE Photovoltaic Specialist Conference, pp. 1914-1918, (2011).

5 Dilute bismide results

5.1 Introduction

The first section of this chapter presents the results of steady state photoconductivity (SSPC) and transient photoconductivity on bulk $GaAs_{1-x}Bi_x$ layers. The objective of the measurements was to test the optical quality and measure the minority carrier lifetime in the dilute bismide ($GaAs_{1-x}Bi_x$).

The second section of this chapter presents the results of the Valance Band Anti-Crossing (VBAC) model. The VBAC model was used to determine the compositions of $GaAs_{1-x}Bi_x$ which will result in the suitable band-gaps for the dilute bismide solar cells. The band-gaps of interest are around 1.0 eV which is suitable for the fourth sub-junction in tandem solar cells [1-3]. Unlike the $Ga_{1-x}In_xN_yAs_{1-y}$ the $GaAs_{1-x}Bi_x$ epilayers grown on GaAs substrates results in a strained system and it imposes a limit on the thickness of the epilayer that can be grown. The strain parameter is calculated and used to determine the critical thickness of epilayers for a given Bismuth (Bi) composition.

The remainder of the chapter presents the results of the dilute bismide p-i-n solar cell that had sufficient respond to light to enable electrical and optical characterisation of the device. The characterisation of the $GaAs_{1-x}Bi_x$ p-i-n solar cell includes dark and light I-V measurements, temperature and radiation dependence of efficiency.

5.2 LAAS bulk bismide layer (sample 2412)

The bulk $GaAs_{1-x}Bi_x$ layer from LAAS (Toulouse France) was grown on a low temperature GaAs buffer layer with solid source MBE. The structure and composition of the layer is shown in figure 5.1.

Material	Thickness (nm)	Doping (cm^{-3})
GaAs contact layer	100 nm	undoped
$GaAs_{0.982}Bi_{0.018}$	233 nm	undoped
GaAs buffer layer	100 nm	undoped
SI GaAs substrate		

Figure 5.1: Sample 2412, Bulk $GaAs_{1-x}Bi_x$ layer (1.8 % Bi) grown on GaAs Semi-Insulating substrate (SI).

For photoconductivity measurements high field bars of dimensions 100 µm by 50 µm were fabricated and Ti/Au contacts were diffused at the edges of the bars. The GaAs cap layer shown in the figure 5.1 was etched out to avoid the excitation of the GaAs cap when excitation sources with wavelengths shorter than GaAs cut-off wavelength are used.

5.3 Steady State Photoconductivity (SSPC)

The spectral dependence of photoconductivity (σ) can be used to measure the absorption edge as well the amount of alloy disorder [4]. Figure 5.2 shows the photoconductivity plots of the bulk $GaAs_{1-x}Bi_x$ with 1.8 % Bi concentration for a bias voltage range of 2.0 V to 4.5 V. The response curves show a peak in photoconductivity at 870±5 nm. The latter peak corresponds to the room temperature absorption edge of GaAs (872 nm) and is attributed to the absorption by the GaAs substrate and the buffer layer. Another peak is observed around 950 nm, which is interpreted as the $GaAs_{1-x}Bi_x$ absorption edge. After the GaAs absorption peak a sharp decline in photoconductivity signal is observed. Unlike the GaAs absorption spectrum, on the longer wavelength side of the $GaAs_{1-x}Bi_x$ photoconductivity curves there are elongated exponential tails between 950 nm to 1300 nm. This region of exponential tails is believed to be due to fluctuations in the energy bandgap caused by lattice vibrations and alloy disorders and is known as the Urbach edge (figure 2.10). A larger Urbach tail suggests a larger alloy

disorder [4]. The inverse slope of the ln (σ) versus photon energy (eV) plot gives the Urbach parameter (E_o) which is a measure of the alloy disorder. The Urbach parameter for this $GaAs_{1-x}Bi_x$ was not quantified as the spectral photon flux of the monochromator lamp, which is required for normalising the curves, could not be accurately determined. However the relatively longer tails observed on the longer wavelength side of the $GaAs_{1-x}Bi_x$ photoconductivity peak compared to the sharp decline of photoconductivity immediately after the GaAs absorption edge, suggest there is a large alloy disorder in the $GaAs_{1-x}Bi_x$. The alloy disorder in $GaAs_{1-x}Bi_x$ has also been observed by [1] with a measured Urbach parameter twice as larger (24 meV) as that of GaAs (13 meV).

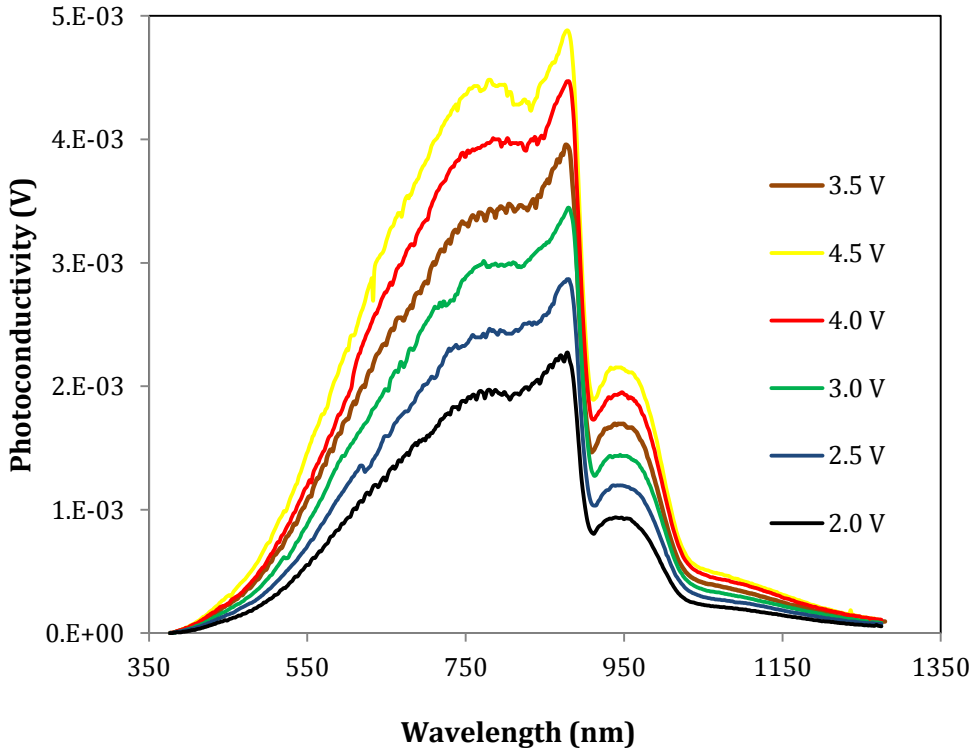

Figure 5.2: Spectral dependence of photoconductivity in a bulk $GaAs_{1-x}Bi_x$ layer with 1.8 % Bi concentration illuminated by the dispersed light from a Bentham M300 monochromator. Measurements were performed between bias voltages of 2.0 V to 4.5 V.

Figure 5.3 shows the photoconductivity signal at a chosen wavelength (950 nm) where absorption is due to $GaAs_{1-x}Bi_x$ only, plotted against bias voltage. The linear relationship observed between the photoconductivity and applied voltage suggests there was no mobility saturation [5] up to 4.5 V (equivalent to an electric field of 90 kV/m, given a bar of 50 µm width). Due to very high resistance of the undoped GaAs cap layer of the $GaAs_{1-x}Bi_x$ sample, the fabricated contacts had a measured resistance of 1.3 MΩ. Therefore most of the potential drop was across the contacts which results in very low electric field in the $GaAs_{1-x}Bi_x$ region. Therefore the linear photoconductivity and voltage relationship is expected for a semiconductor material at the region of low field transport.

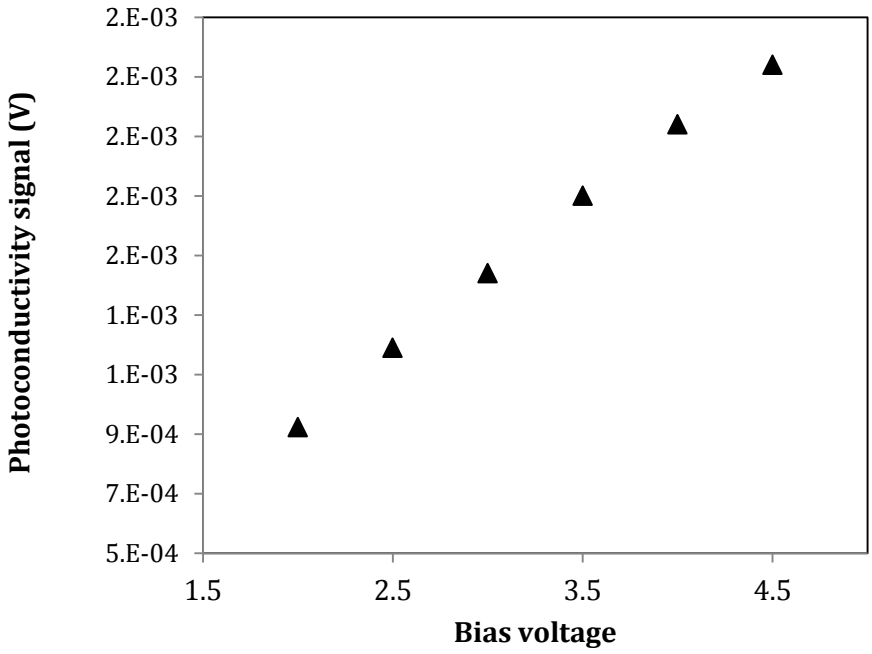

Figure 5.3: Photoconductivity dependence of bias voltage in a bulk $GaAs_{1-x}Bi_x$ layer with 1.8 % Bi concentration. The values of photoconductivity signal were deduced from figure 5.2 at 950 nm (peak absorption of $GaAs_{1-x}Bi_x$).

5.4 Transient Photoconductivity

Figure 5.4 is the transient photoconductivity plots for the bulk $GaAs_{1-x}Bi_x$ at 1.8 % Bi concentration. Minority carrier lifetimes can be deduced from decay constant of the transient photoconductivity plots. From the graphs long decay constants in the order of microseconds were observed, which are too high to be attributed to $GaAs_{1-x}Bi_x$ photoconductivity decay. The carrier lifetime and consequently the decay constants of $GaAs_{1-x}Bi_x$ is expected to be less than the average recombination time in GaAs (10^{-8} s) [5], due to defects introduced in GaAs lattice by incorporation of Bismuth atoms. The non-observance of $GaAs_{1-x}Bi_x$ minority carrier decay could be attributed to some extent the difficulty of getting a low resistance contact to the $GaAs_{1-x}Bi_x$ samples which had an un-doped GaAs cap layer. Due to high resistance of the contacts the overall capacitive impedance of the circuit was too high to observe fast transient associated with the recombination lifetimes. Secondly the Nd: YAG picosecond laser tuned to 533 nm emission to enable excitation the $GaAs_{1-x}Bi_x$ layer with an absorption edge around 950 nm (section 5.3), consequently the laser was tuned to 533 nm emission. With the 533 nm (hv=2.3 eV) emission from the laser, there was a possibility of excitation of GaAs ($E_g = 1.42\ eV$) layer. Although the GaAs cap layer (shown in figure 5.1), was etched out, there was still sufficient GaAs under the contacts that could be simultaneously excited with the $GaAs_{1-x}Bi_x$. If the excitation of GaAs layer is dominant, the decay will be dominated by GaAs recombination time constant resulting in slow decays shown in figure 5.4. The other possible factor could be carrier trapping and re-emission from shallow traps, with an effect of elongated decay constants [6, 7].

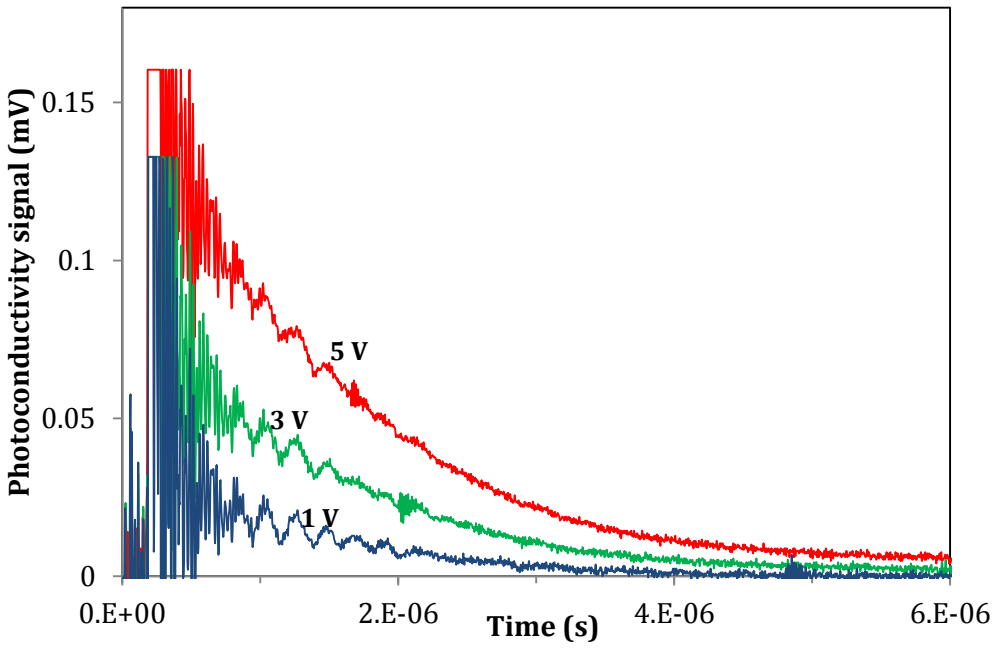

Figure 5.4: Transient photoconductivity in bulk $GaAs_{1-x}Bi_x$ layer with 1.8 % Bismuth concentration.

5.5 Modelling of dilute bismide solar cells

5.5.1 Band Anti Crossing Model (BAC)

The band-gap of $GaAs_{1-x}Bi_x$ suitable for use in tandem solar cells was determined using the Valence Band Anti Crossing (VBAC) model. Unlike the incorporation of Nitrogen (N) into GaAs, which perturbs the conduction band, Bismuth (Bi) interacts more with the valence band of GaAs than its conduction band. Incorporation of Bi into GaAs lattice forms a Bi resonant level closer to the valence band maximum (VBM). The interaction of the Bi resonant level with the GaAs VBM tends to perturb the light hole, heavy hole and the spin off orbit sub-bands. The dispersion relation for the perturbation of $GaAs_{1-x}Bi_x$ valance band is given by;

$$E_{\pm}(GaAsBi) = \frac{E_v(GaAs)+E_{Bi} \pm \sqrt{(E_v(GaAs)-E_{Bi})^2+4xC_{Bi}^2}}{2} \qquad (5.1)$$

where $E_v(GaAs), E_{Bi}$ and C_{Bi} are the VBM of GaAs, Bismuth level and the coupling parameter respectively.

The equation 5.1 has two solutions for E_+ and E_-, which suggest each sub-band will split into two. The strength of perturbation depends on the composition (x) of Bi in the $GaAs_{1-x}Bi_x$ alloy as well as the interaction strength of the Bi level with the host alloy energy band. In the model the interaction strength is given by the coupling parameter (C_{Bi}). Coupling parameter has been reported to vary between 1.55-1.6 [8, 9]. Some work has reported that setting the interaction parameter to 2.2 [10], resulted in VBAC that accurately models the experimental observation The Bismuth defect level E_{Bi} has been estimated by [11] to lie at 0.4 eV below the VBM. The VBAC effects of $GaAs_{1-x}Bi_x$ alloy at Bi composition x=0.01 are shown in figure 5.5.

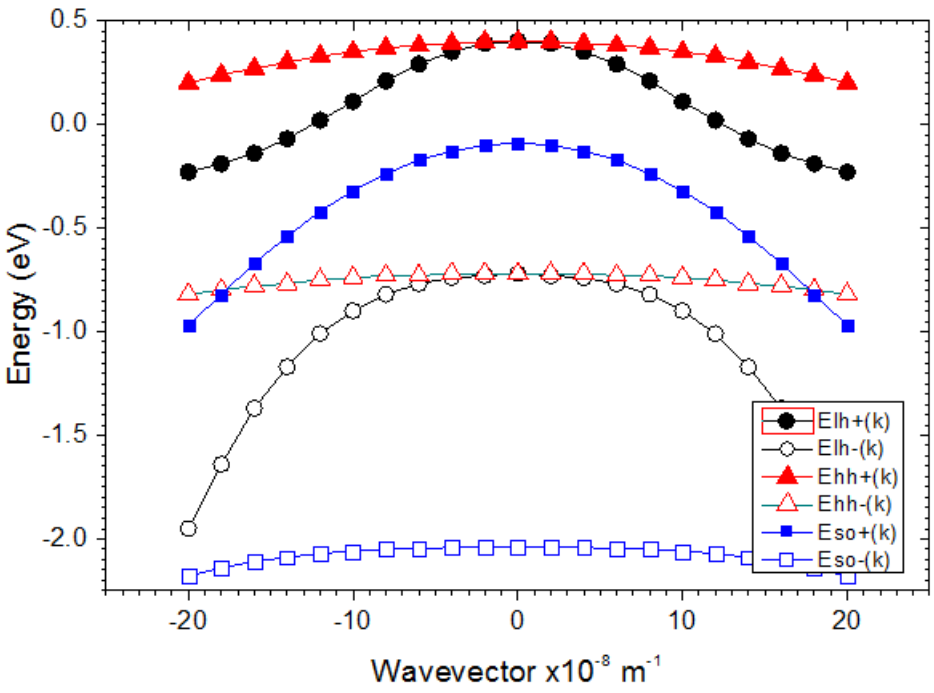

Figure 5.5: VBAC effects in $GaAs_{1-x}Bi_x$ alloy with 1% Bismuth composition: Triangles; light holes E- and E+, Circles: heavy holes E- and E+, Squares; Spin Orbit and its splitting.

The resultant bandgap of $GaAs_{1-x}Bi_x$ was determined by the difference between the GaAs Conduction Band Minima (CBM) and $GaAs_{1-x}Bi_x$ heavy hole (HH) minima. The variation of $GaAs_{1-x}Bi_x$ band gap with Bi composition calculated from VBAC is shown in figure 5.6.

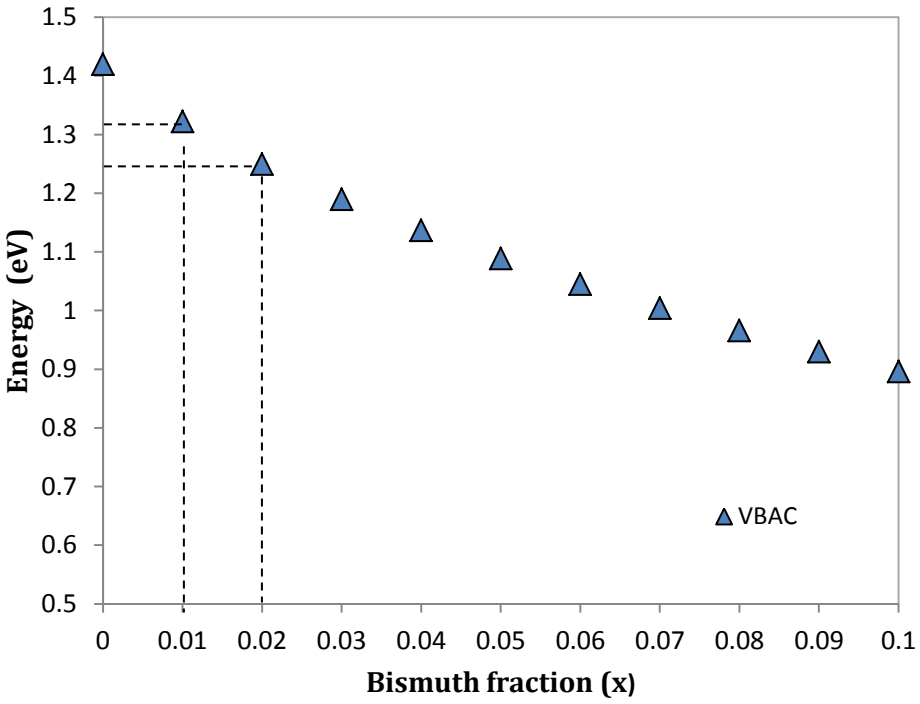

Figure 5.6: Effect of Bi composition on the bandgap of $GaAs_{1-x}Bi_x$ as determined by VBAC model.

Bi composition of 0.01(1%) and 0.02(2%) were chosen to use in both the bulk and MQWs p-i-n solar cells. The band gap of $GaAs_{1-x}Bi_x$ composition 0.01 and 0.02 calculated from the VBAC model in figure 5.2 correspond to band-gap of 1.32 eV and 1.25 eV respectively. The structures of the solar cell based on this model results are shown in section 5.5.

5.5.2 Biaxial strain

In a solar cell it is important that the layers grown should lattice match the substrate to avoid relaxation due to tensile or compressive strain. In case of $GaAs_{1-x}Bi_x$ bulk p-i-n structures the tensile strain builds up with thickness of $GaAs_{1-x}Bi_x$ intrinsic layer due to replacement of smaller Arsenic (As) atoms by larger Bismuth (Bi) atoms. The strain on $GaAs/$ $GaAs_{1-x}Bi_x$ heterostructures (QWs or epilayers) was determined using the strain parameter (ε) in equation (5.2).

$$\varepsilon = \frac{a_s - a_w}{a_w} \tag{5.2}$$

where a_s is the lattice constant of the substrate (GaAs) and a_w is the lattice constant of the material grown. The strain parameter for 1% $GaAs_{1-x}Bi_x$ ($GaAs_{0.99}Bi_{0.01}$) and 2% $GaAs_{1-x}Bi_x$ ($GaAs_{0.98}Bi_{0.02}$) epilayers were found to be 0.0012 and 0.0024 respectively. The critical thickness d(the thickness beyond which relaxation of a strained layers is expected to occur) was calculated using (5.3).

$$d \approx \frac{a_s}{2|\varepsilon|} \tag{5.3}$$

The critical thickness for $GaAs_{0.99}Bi_{0.01}$ and $GaAs_{0.98}Bi_{0.02}$ and was found to be 283 nm and 118 nm respectively. The $GaAs_{0.99}Bi_{0.01}$ bulk p-i-n was grown with only 200 nm intrinsic to avoid possible dislocations. Initially an intrinsic region of 410 nm was intended, as it would exactly match the thickness if intrinsic region in $GaAs_{1-x}Bi_x$ MQW structures. Therefore it would also serve as a standard for the p-i-n $GaAs_{1-x}Bi_x$ MQWs solar cells.

5.6 Structures of the dilute bismide solar cells

The first batch of $GaAs/GaAs_{1-x}Bi_x$ solar cells was grown at Chalmers University of Technology (CUT) in the Department of Microtechnology and Nanoscience using a Riber Compact21 MBE system shown in figure 3.4. Firstly the substrates were degassed in the preparation chamber by heating at a relatively low temperature (<400 °C). The GaAs wafers were then de-oxidated at 650 °C and the RHEED pattern was used to monitor the disappearance of the oxide layer. Then the growth temperature was reduced to 615 °C (the real surface temperature was 580 °C), to grow most part of the structures. All the Bi-containing layers were grown at relatively lower temperature of 360 °C to ensure Bismuth is incorporated [12, 13]. Before and after the Bi-containing part, the growth temperature was linearly graded down and up during the growth of GaAs. The growth rate of all GaAs layers

was $1\mu m/h$ and $1.25\mu m/h$ for $Al_{0.8}Ga_{0.2}As$. Figure 3.5 shows a sample RHEED signal for the $GaAs/GaAs_{1-x}Bi_x$ multiple well solar cells.

The base design (the thickness and doping of the base and emitter regions) was grown same as the base design for the best dilute nitride MQWs solar cell (VN1585), for comparative purposes. The $GaAs_{1-x}Bi_x$ devices included the bulk p-i-n device (T0726) and MQWs p-i-n (T0728 and T0729) solar cells, shown in figures 5.3-5.4. The bulk p-i-n structure has a 230 nm nominally undoped $GaAs_{0.99}Bi_{0.1}$ intrinsic region. The MQWs p-i-n devices T0728 and T0729 had ten 10 nm $GaAs_{0.98}Bi_{0.2}$ and $GaAs_{0.99}Bi_{01}$ quantum wells separated by 10 nm GaAs barriers respectively.

p GaAs	Be $2x10^{18}$ cm^{-3}	200nm
p $Al_{0.8}$ $Ga_{0.2}$ As	Be $2x10^{18}$ cm^{-3}	40nm
Intrinsic	$GaAs_{0.99}Bi_{0.01}$	230 nm
n GaAs	Si $2x10^{17}$ cm^{-3}	2500nm
n+ GaAs	Si $2x10^{18}$ cm^{-3}	20nm
n+ GaAs	substrate	

Figure: 5.7: The design of the p-i-n bulk $GaAs_{1-x}Bi_x$ solar cell (T0726).

p GaAs	Si 2x10^{18} cm^{-3}	200nm
n $Al_{0.8}Ga_{0.2}As$	Si 2x10^{18} cm^{-3}	40nm
n GaAs	Si 2x10^{18} cm^{-3}	200nm
UD GaAs		110nm
i $GaAs_{0.98}Bi_{0.02}$		10nm
UD GaAs		10nm
i $GaAs_{0.98}Bi_{0.02}$		10nm
UD GaAs		10nm
i $GaAs_{0.98}Bi_{0.02}$		
UD GaAs		10nm
i $GaAs_{0.98}Bi_{0.02}$		10nm
UD GaAs		10nm
i $GaAs_{0.98}Bi_{0.02}$		10nm
UD GaAs		10nm
i $GaAs_{0.98}Bi_{0.02}$		10nm
UD GaAs		10nm
i $GaAs_{0.98}Bi_{0.02}$		10nm
UD GaAs		10nm
i $GaAs_{0.98}Bi_{0.02}$		10nm
UD GaAs		10nm
p GaAs	Be 2x10^{17} cm^{-3}	3000nm
p+ GaAs	Be 2x10^{18} cm^{-3}	20nm
p+ GaAs	substrate	

(i)

p GaAs	Si 2x10^{18} cm^{-3}	200nm
n $Al_{0.8}Ga_{0.2}As$	Si 2x10^{18} cm^{-3}	40nm
n GaAs	Si 2x10^{18} cm^{-3}	200nm
UD GaAs		110nm
i $GaAs_{0.99}Bi_{0.01}$		10nm
UD GaAs		10nm
i $GaAs_{0.99}Bi_{0.01}$		10nm
UD GaAs		10nm
i $GaAs_{0.99}Bi_{0.01}$		10nm
UD GaAs		10nm
i $GaAs_{0.99}Bi_{0.01}$		10nm
UD GaAs		10nm
i $GaAs_{0.99}Bi_{0.01}$		10nm
UD GaAs		10nm
i $GaAs_{0.99}Bi_{0.01}$		10nm
UD GaAs		10nm
i $GaAs_{0.99}Bi_{0.01}$		10nm
UD GaAs		10nm
p GaAs	Be 2x10^{17} cm^{-3}	3000nm
p+ GaAs	Be 2x10^{18} cm^{-3}	20nm
p+ GaAs	substrate	

(ii)

Figure 5.8: The design of $GaAs_{1-x}Bi_x$ MQWs solar cells (i) T0728 and (ii) T0729

The other $GaAs_{1-x}Bi_x$ solar cell studied in this work is the p-i-n solar cell grown by plasma assisted MBE in Tampere University of Technology (TUT). The structure of the TUT p-i-n solar cell is shown in figure 5.9.

Material	Thickness (nm)	Doping (cm^3)
p GaAs	50.00	N_a=5x10^{18}
p GaAs	250.00	N_a=2x10^{18}
i $GaAs_{0.98}Bi_{0.017}$	220.00	None
n GaAs	600.00	N_d=1x10^{18}
n GaAs buffer	200.00	N_d=2x10^{18}
n GaAs substrate		N_d~2x10^{18}

Figure 5.9: Structure of the p-i-n bulk $GaAs_{1-x}Bi_x$ studied grown at Tempera University of Technology.

5.7 CUT bismide solar cells results

The dilute bismide solar cells grown in Chalmers University of Technology (CUT), did not respond to light excitation. This included the p-i-n bulk $GaAs_{1-x}Bi_x$ (T0726) and the p-i-n $GaAs_{1-x}Bi_x$ MQWS solar cells (T0728 and T0729). These devices are included as it initially formed part of the proposed study, which was "comparative study of $GaAs_{1-x}Bi_x$ /$GaAs$ and $Ga_{1-x}In_xN_yAs_{1-y}/GaAs$ multiple quantum wells in photovoltaics". The SEM images of the devices are shown in figure 5.10(i), show pits across the entire wafer that could possibly be transcending deep into the active region of the device. The roughness of the normal of a wafer is also shown in figure 5.10 (ii) for comparison.

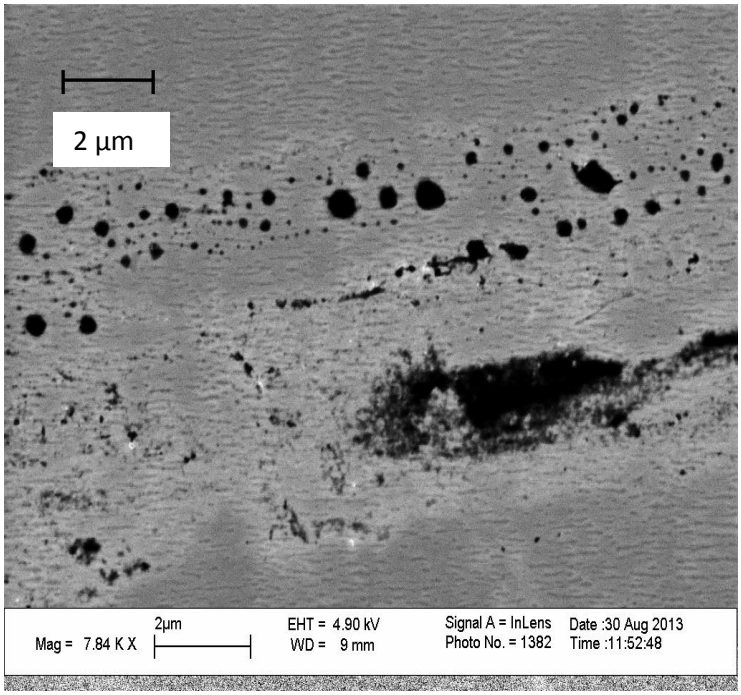

(i)

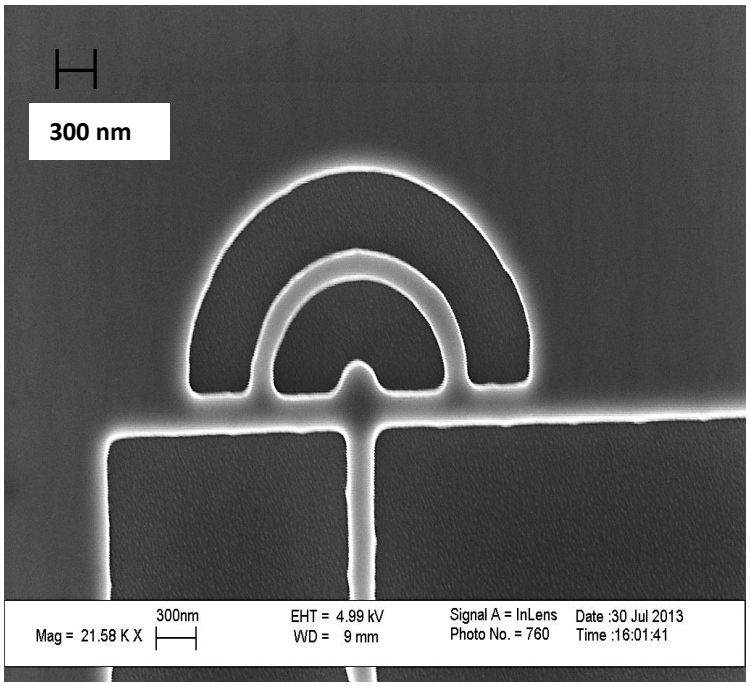

(ii)

Figure 5.10: SEM images of (i) a wafer with normal roughness; (ii) a sample of bismide solar cell wafer grown in Chalmers University of Technology.

The RHEED signal taken during growth of a $GaAs_{1-x}Bi_x$ MQWS solar cell is shown in figure 5.11. The tendency to form a spotty pattern of the RHEED signal confirms that the growth was not smooth.

Figure 5.11: The RHEED signal for $GaAs/GaAs_{1-x}Bi_x$ multiple well solar cell grown at Chalmers University of Technology.

The sample I-V characteristics of the p-i-n bulk $GaAs_{1-x}Bi_x$ (T0726) and the $GaAs_{1-x}Bi_x$ MQWs (T0728) are shown in figures 5.12 (i) and (ii) respectively. The p-i-n bulk $GaAs_{1-x}Bi_x$ (T0726) showed some response to light but did not show typical junction characteristics but rather what appears as a double junction, which was attributed to growth problems (fig. 5.12(i)). The MQWs solar cell (T0728) did not show any response to light and the dark and light I-V characteristics were the same, besides the slight shift due to heating effect of the incident radiation(fig. 5.12(ii)).

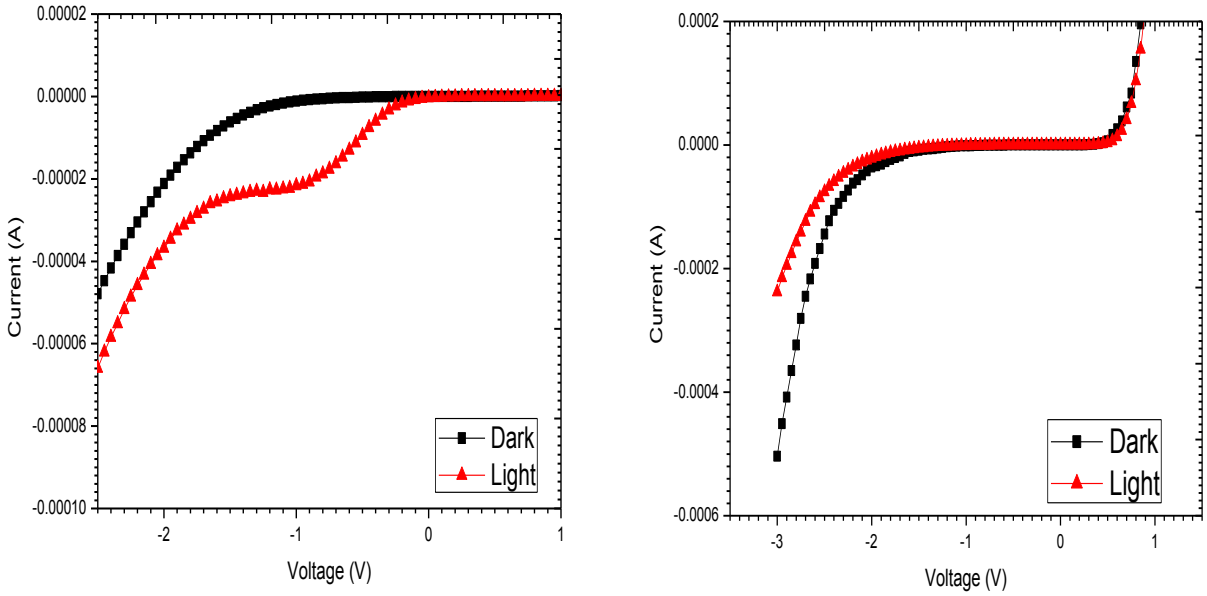

(i) (ii)

Figure 5.12: Dark and light I-V characteristics of $GaAs_{1-x}Bi_x$ solar cells grown in Chalmers University of Technology: (i) bulk p-i-n $GaAs_{1-x}Bi_x$ (TO726) and (ii) MQWs $GaAs_{1-x}Bi_x$ (TO728) solar cells.

5.8 TUT bismide p-i-n solar cell results

The rest of this chapter is dedicated to its characterisation the p-i-n bulk $GaAs_{1-x}Bi_x$ solar cell grown by Tampere University of Technology (TUT) that showed enough photocurrent that enabled various measurements to be performed.

5.8.1 Spectral response

The spectral response of the p-i-n bulk $GaAs_{1-x}Bi_x$ solar cell shown in figure 5.13, confirms the absorption of the $GaAs_{1-x}Bi_x$ layer up to 985 nm. The relative response in the bismuth region is too low but could not be interpreted as poor absorptivity or quality of bismuth as the layer was too thin (230 nm).

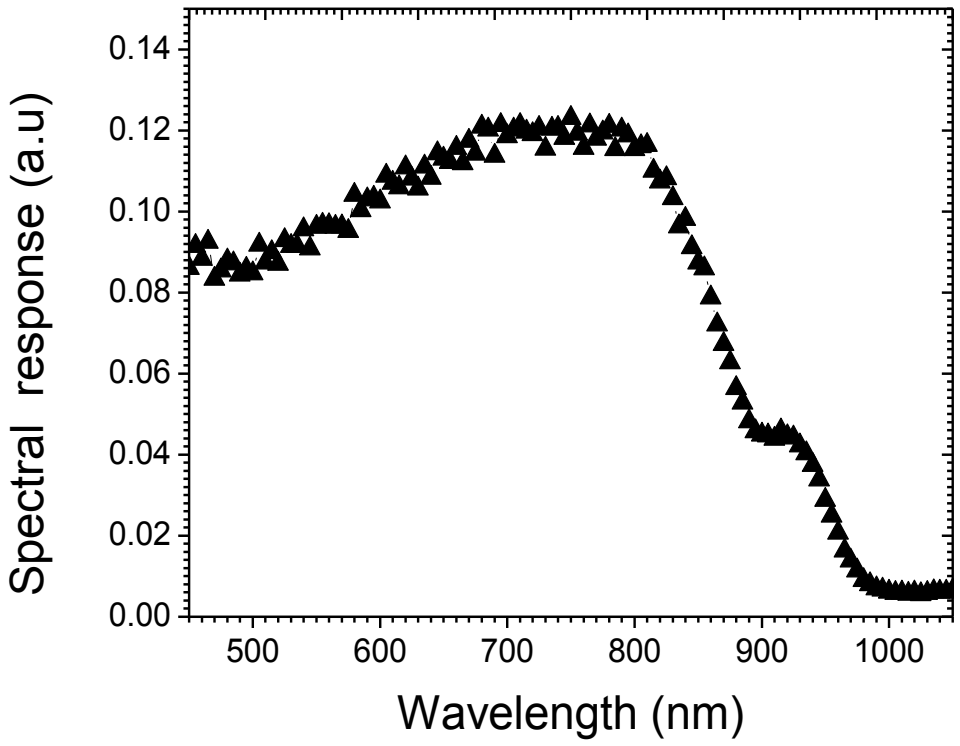

Figure 5.13: The spectral response of the TUT $\boldsymbol{GaAs_{1-x}Bi_x}$ *p-i-n solar cell.*

5.8.1 Dark I-V characterisation

The dark current density of the dilute bismide ($GaAs_{1-x}Bi_x$) plotted together with those of dilute nitride ($Ga_{1-x}In_xN_yAs_{1-y}$) p-i-n solar cells for comparative purposes is shown in figure 5.14. The results show that the generation current density (under reverse bias), are all in the same order of magnitude (10^{-11} Acm^{-2}). Under the forward bias, both the magnitude and ideality factors (~1.8) of the diode do not show any notable differences. However the dilute bismide p-i-n had a much lower intrinsic region of 230 nm as opposed to 600 nm and 900 nm in the dilute nitride p-i-n solar cells. In that case plotting the electric field (E) instead of voltage, against current will give a fairer comparison. The plot of E-J under reverse bias is shown in figure 5.15. The E-J plots also

do not reveal any notable differences in magnitude and quality of the generation dark current.

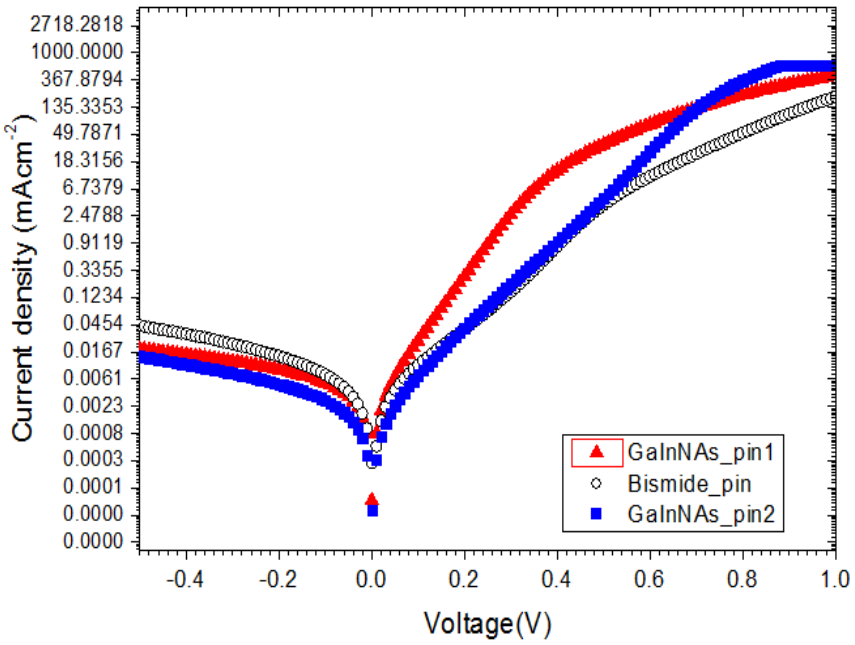

(a)

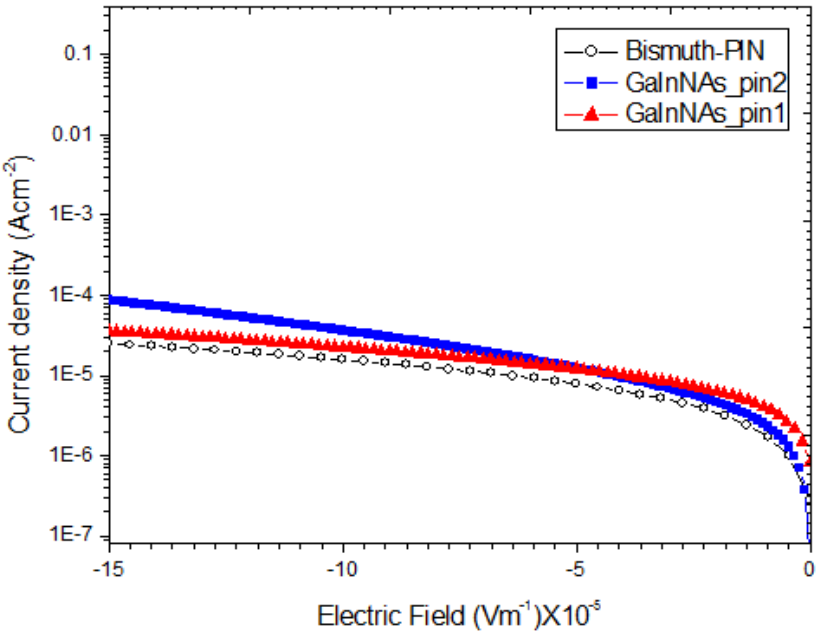

(b)

Figure 5.14: (a) Dark current I-V characteristics of TUT dilute bismide solar cell plotted together with those of bulk dilute nitride p-i-n solar cells. (a) Current density versus applied voltage; (b) Current density versus Electric field: (i) circles; p-i-n solar cell with 230 nm $GaAs_{1-x}Bi_x$ *intrinsic region; (ii) squares; p-i-n solar cell with 900 nm* $Ga_{1-x}In_xN_yAs_{1-y}$ *intrinsic region(pin2), and (iii) triangles; p-i-n solar cells with 600 nm* $Ga_{1-x}In_xN_yAs_{1-y}$ *intrinsic region(pin1).*

5.8.2 AM1.5G I-V characterisation

The AM1.5G I-V characterisation was performed at RT over a range of 1 to 4 suns with the aid of condenser lens. The figures of merit are summarised in Table 1. The device showed; $J_{sc} = 218\ \mu A$; $V_{oc} = 0.42$ V; *FF*=41.3% and η=4.82 %. The low J_{sc} could not be attributed to either poor optical or electrical properties of $GaAs_{1-x}Bi_x$ as the active region of cell was too thin (1.27 µm) to absorb enough light. A GaAs solar cell will need approximately 3 µm to absorb nearly all the incident light as discussed in section 2.5.1. The V_{oc} of 0.4 V is comparable to that of dilute nitride p-i-n devices (section 4). This is reasonable as the bismide junction is generating the dark current approximately same as the dilute nitride p-i-n solar cells are shown in figure 5.14. The short circuit current density increases linearly with intensity as shown in the inset graph of figure 5.15, which is consistent with theory in section 4.1.4 for a bulk material.

Irradiance (W/m^2)	P_{in}(W)	I_{sc}(A)	V_{oc}(V)	P_{out}(W)	FF(%)	η (%)
1000	7.85x10^{-4}	2.18 x10^{-4}	0.42	3.7 x10^{-5}	41.3	4.82
2000	1.57 x10^{-3}	4.47 x10^{-4}	0.45	9.78 x10^{-5}	48.6	6.23
3000	2.3 x10^{-3}	7.73 x10^{-4}	0.46	1.74 x10^{-4}	48.9	7.73
4000	3.1 x10^{-3}	1.06 x10^{-3}	0.47	2.4 x10^{-4}	49.6	7.86

Table 5.1: Figures of merit for bismide p-i-n solar cell at different intensity levels of an AMG1.5 simulator spectrum.

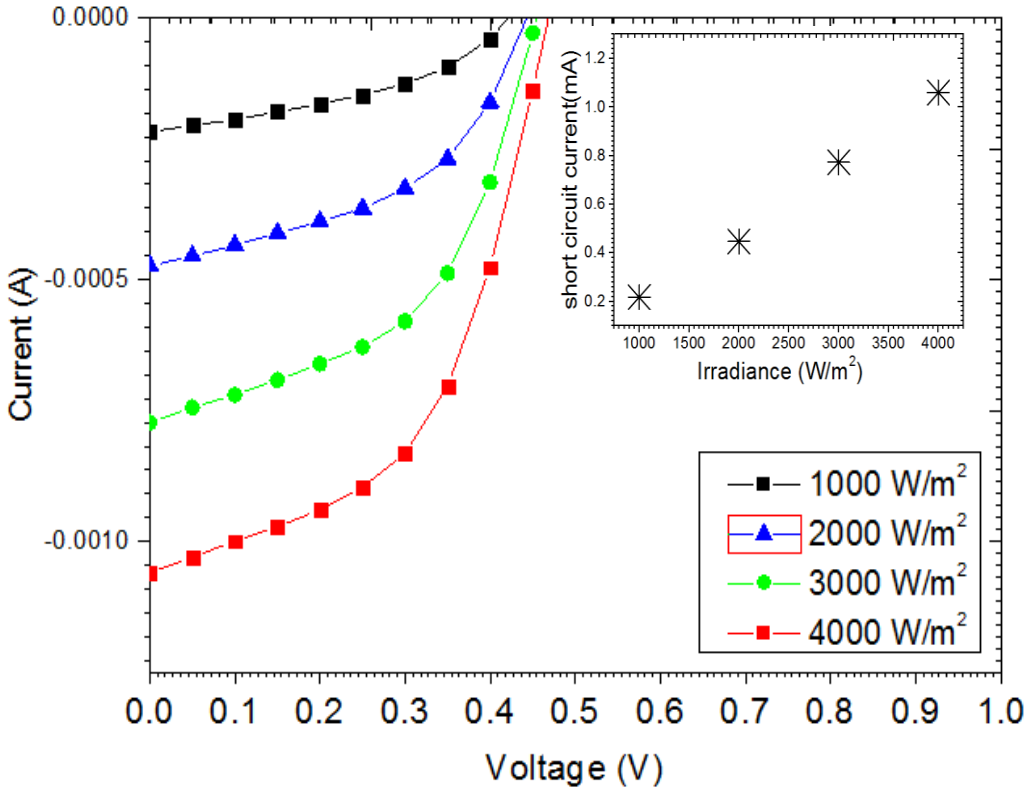

Figure 5.15: I-V characteristics of a $GaAs_{1-x}Bi_x$ *p-i-n solar cell at different intensity levels of an AMG1.5 simulator spectrum.*

5.9 Conclusion

The photoconductivity and spectral response results on the bulk $GaAs_{1-x}Bi_x$ layer and the $GaAs_{1-x}Bi_x$ solar cells confirmed the absorption of $GaAs_{1-x}Bi_x$ beyond the GaAs cut-off wavelength. Photoconductivity spectrum of $GaAs_{1-x}Bi_x$ some alloy disorder as evidenced by long exponential tails on the longer wavelength side of the absorption edge. The measurement of minority carrier lifetime of $GaAs_{1-x}Bi_x$ by could not be successfully deduced from the transient photoconductivity measurements due to possibly unwanted excitation of the GaAs cap layer under the high field bar contacts. The inclusion of $GaAs_{1-x}Bi_x$ (a dilute bismide alloy) does not deteriorate the open circuit voltage (V_{oc}) more than that of the dilute nitride p-i-n solar cells. The dark current density in a dilute bismide

solar is dominated by non-radiative recombination and is of the same order of magnitude as the dark current density of the dilute nitride p-i-n solar cells.

References

[1] C. J. Hunter e.t al., "*Absorption Characteristics of $GaAs_{1-x}Bi_x/GaAs$ diode in Near-Infrared,"* IEEE Photonics Technology Letters, Vol. **24**, pp. 2191-219 (2012).

[2] D. B. Jackrel, Seth R. Bank, H. B. Yuen, M. A. Wistey, and J. S. Harris, Jr., *"Dilute Nitride GaInNAs and GaInNAsSb Solar Cells by Molecular Beam Epitaxy,"* J. Appl. Phys. Vol. **101**, pp. 114916 (2007).

[3] D. J. Friedman, J. F. Geisz, S. R. Kurtz, and J. M. Olson, *"1-eV GaInNAs Solar Cells for Ultrahigh-Efficiency Multi-junction Devices"* Presented at the 2nd World Conference and Exhibition on Photovoltaic Solar Energy Conversion; Vienna, Austria, 6-10 July, (1998).

[4] E. Strohm, M. Adamcyk, B. J. Ruck, and T. Tiedje, *"Photoconductivity of Dilute InGaNAs and GaNAs Alloys Grown by Molecular Beam Epitaxy,"* In APS Meeting Abstracts, Vol. **1**, pp. 30003, (2001).

[5] S.M. Sze, K. NG. Kwok, **"Physics of Semiconductor Devices", 3rd Edition,** (Wiley InterScience, 2006).

[6] Daniel MacDonald*; "On the use of a bias light correction for trapping effects in photo conductance-based lifetime measurements of silicon"*, J. Appl. Phys. Vol. **89**, pp. 2772 (2001).

[7] Christina Honsberg (2013) PVEducation. Available at: http://pveducation.org/, [Accessed 01 July 14].

[8] K. Alberi et al., *"Valence-band anticrossing in mismatched III-V semiconductor alloys"*, Physical Review B., Vol. **75**, Issue 4, pp. 045203, (2007).

[9] K. Alberi et al., *"Valence band anti-crossing in $GaAs_{1-x}Bi_x$"*, Appl. Phys. Lett., Vol. **91**, pp. 051909, (2007).[10] A. R. B. Mohmad, *"Growth and Characterisation of $GaAs_{1-x}Bi_x$"*, PhD. Thesis, University of Sheffield, 2013.

[11] J. Shao, W. Lu, M. Sadeghi, *"Evolution of Valance Band Alignment with Nitrogen Content in GaNAs / GaAs single quantum wells"*, Applied Physics Letters, Vol. **93**, pp. 031904, (2008).

[12] Y. Tominaga, Y. Kinoshita, K Oe, and M. Yoshimoto, *"Structural investigation of $GaAs_{1-x}Bi_x$/GaAs multiquantum wells",* Appl. Phys. Lett., Vol. **91**, pp. 131915, (2008).

[13] Mooney et al., *"Deep level defects in n-type GaAsBi and GaAs grown at low temperatures",* J. Appl. Phys. Vol. **113**, pp. 133708 (2013).

6.0 Conclusion and future work

In this work it has been demonstrated that for $Ga_{1-x}In_xN_yAs_{1-y}$ p-i-n structures based on GaAs design, the total dark current of the device is essentially the dark current generated in the $Ga_{1-x}In_xN_yAs_{1-y}$ intrinsic layer. This model is based on the assumption that for large intrinsic regions such as the ones used in this work (600 nm -900 nm), the SCR is approximated by the intrinsic region thickness. The measured dark current in the p-i-n devices fit well to the S-N-S model. This observation confirms the dominance of non-radiative recombination component of the dark current, which suggest the material has deep traps or recombination centres that lie in the forbidden gap.

The typically low V_{oc} of the dilute nitrides was investigated by comparing the two $Ga_{1-x}In_xN_yAs_{1-y}$ p-i-n solar cell with different nitrogen compositions. The preliminary results indicate that the band-gap difference does not account for large V_{oc} difference exhibited by the devices. The much lower V_{oc} in the device with high nitrogen content was attributed to poor electrical properties of the nitride. Further the average recombination lifetime was estimated and revealed that the recombination lifetimes reduce significantly with nitrogen composition change.

To establish the above observations, further investigation needs to be carried out with a sizeable batch of $Ga_{1-x}In_xN_yAs_{1-y}$ p-i-n structures with differing nitrogen compositions.

The dilute MQWs have been extensively investigated and it has been observed that: radiative recombination in QWs is supressed and the total dark current has anomalously high ideality factors. Despite the theoretical projection that the MQWs solar cell can enhance the efficiency of the tandem solar cell, it is very unlikely with $Ga_{1-x}In_xN_yAs_{1-y}$ unless the source of dominant non-radiative recombination is established and eliminated.

The dark current analysis reveals that increasing N% composition in the solar cell material increases the dark current density in the solar cells. In the set of MQWs with nitrogen composition of 1.0 % (VN1585), 1.5 % (ASN2604 and ASN2605) and 1.6 % (ASN3134 and ASN3138), the MQWs cell with the lowest N% composition (VN1585) produced the lowest dark current. The solar cells with the nitrogen compositions of 1.5 % and 1.6 % which is practically equally nitrogen composition all showed dark currents magnitude that is higher than VN1585. Similarly the bulk p-i-n $Ga_{1-x}In_xN_yAs_{1-y}$ with higher N% composition (2.8%) showed relatively higher dark current density than the p-i-n $Ga_{1-x}In_xN_yAs_{1-y}$ with a lower N% composition (2.0%). Besides the nitrogen composition a clear design related dark current was observed for the set of solar cells studied. In general the bulk p-i-n structures showed the lowest dark current, followed by the MQWs and lastly the n-i-p-i structure with the highest dark current density. Theoretically the intrinsic impact of QWs in MQWs solar cells would be such that the dark current density is reduced due to supressed qausi-fermi levels in the quantum wells region as discussed in section 4.4.3. However in this work the bulk p-i-n solar cell generated less dark current than MQWs p-i-n solar cell by more than two orders of magnitude (figure 4.4 and figure 4.17), except for the MQWs solar cell with lowest Nitrogen composition VN1585. Further work needs to be done to establish if this is related to growth defects on quantum wells or nitrogen composition related.

The $Ga_{1-x}In_xN_yAs_{1-y}$ MQWs show a near flat temperature dependence for the device with shallowest wells (VN1585) and as the depth of the wells increases the temperature coefficients become more negative though still much lower than the standard p-n junction (TS0419) solar cell (see figure 4.37). In this work this has been attributed to competing mechanism of carrier escape from and recombination inside the wells. The latter effect results in dark current which is effectively less sensitive to temperature changes, consequently less temperature coefficients for efficiency of the devices.

The spectral response of $Ga_{1-x}In_xN_yAs_{1-y}$ n-i-p and p-i-n MQWs solar cell show that the difficulty of the electron to cross the strongly perturbed conduction band results in diminished response at shorter wavelengths for p-i-n and longer wavelengths for n-i-p design respectively.

The relative carrier trapping strength in each device was deduced from the slopes of the hyperbolic logarithmic plots of dark current density against temperature. The results show the same trend shown by the dark currents; n-i-p-i showing steepest slopes corresponding to strongest carrier trapping in the devices, followed by MQWs and lastly p-i-n devices. This clearly was not due to material effects as the n-i-p-i that show this result was a GaAs device. Though the dilute nitride n-i-p-i device got blown before it was fully tested, the result of the GaAs n-i-p-i solar cell still gave an insight on the performance of the design. The n-i-p-i structure shows good carrier collection as shown in figure 4.27. However if the dilute nitride or bismide n-i-p-i structure has to be considered as a fourth sub-junction in tandem solar cells the strong carrier trapping effect and relatively high dark current have to be established and reduced. The V_{oc} of the n-i-p-i solar cells increases markedly with increasing light intensity Although the n-i-p-i structures has been modelled and tested for photovoltaic application in the past, there is no report on the performance of n-i-p-i at elevated radiation levels. More experimental work needs to be done to test the n-i-p-i photovoltaic devices under elevated radiation levels, for applicability of the structure in concentrator multi-junction solar cells.

Although, majority of the dilute bismide solar cells could not respond to light, the dilute bismide bulk layers and a bulk bismide p-i-n solar cell enabled the study of photoconductivity and I-V characterisation measurements. Both the dilute nitride and bismide alloy show a band-gap reduction. The inclusion of $GaAs_{1-x}Bi_x$ (dilute bismide) does not deteriorate the open circuit voltage (V_{oc}) more than the $Ga_{1-x}In_xN_yAs_{1-y}$ (dilute nitride). Dark current

density in a bulk p-i-n dilute bismide solar cell is observed to be of same order of magnitude and quality (dominated by non-radiative recombination current) as of the bulk p-i-n dilute nitrides. Photoconductivity measurements reveal strong alloy disorder in dilute bismide alloy ($GaAs_{1-x}Bi_x$) as evidenced by long exponential tails on the longer wavelength side of the absorption edge.

Non-availability of comprehensive data on very important material parameters such as absorption coefficient and the holes effective mass of dilute bismides has thus far hindered a lot of work in modelling dilute nitride solar cells. The absorption coefficient of dilute bismides alloys in the region of UV-IR would enable modelling of photo-generated current by the dilute bismide solar cells illuminated by different spectra. Hole effective mass would enable modelling transitions in dilute bismide quantum wells. The latter models would also enable theoretical comparative study of dilute nitride and bismide quantum wells. In future more experimental work needs to be done on optical transmission and absorption of dilute bismide alloys over a wider range of spectrum (UV-IR) to enable modelling photocurrent on solar cells. Such experiments include transmittance, reflectance and ellipsometry measurements on bulk dilute bismide layers.

APPENDIX A

Matlab script: Diffusion current a GaAs p-n junction solar cell.

%The script calculates the diffusion current in the base and emitter regions of the %GaAs solar cell (base design for bulk p-i-n, and MQWs p-i-n solar cells) using the ideal % Shockley diode equation;

%%$J = (J_{0,base} + J_{0,emitter})\left(\exp\left(\frac{qV}{kT}\right) - 1\right)$

%% $J_{0,base} = q\left(\frac{D_b}{L_b}\right)\left(\frac{n_i^2}{N_b}\right)\left(\frac{(S_b L_b/D_b)+tanh(x_b/L_b)}{(S_b L_b/D_b)tanh((x_b/L_b)+1}\right)$

%%$J_{0,emitter} = q\left(\frac{D_e}{L_e}\right)\left(\frac{n_i^2}{N_e}\right)\left(\frac{(S_e L_e/D_e)+tanh(x_e/L_e)}{(S_e L_e/D_e)tanh((x_e/L_e)+1}\right)$

% CONSTANTS

```
T=298;                          % Room Temperature
k=1.38e-23;                     % Boltzmann's constant
q= 1.60218e-19;                 % Unit electrical charge


%DECLARATION OF VARIABLES
%%%Materials parameters%%%%%%%%%%%%%%%%%%%%%%%%%%%
Na_ba=2E17;                     % Doping density in the emitter region
Nd_em=2E18;                     % Doping density in the base region
mi_ba=3000;                     % Mobility of minority carriers in the base
mi_em=150;                      % Mobility of minority carriers in the emitter
tau_ba=4E-9;                    % Lifetime of minority carriers in the base
tau_em=1E-9;                    % Lifetime of minority carriers in the emitter
S_ba=1E50;                      % Base surface-recombination velocity
S_em=1E2;                       % Emitter surface-recombination velocity
Ni =2E6;                        % Intrinsic carrier concentration
x_ba=3000E-7;                   % Base thickness
x_em=200E-7;                    % Emitter thickness

%DEPENDENT VARIABLES%%%%%%%%%%%%%%%%%%%%%%%%%%%%%%%

D_ba= (k*T/q)*mi_ba;            % Diffusion coefficient of electrons in the base
D_em= (k*T/q)*mi_em;            % Diffusion coefficient of holes in the emitter
L_ba= sqrt (D_ba*tau_ba);       % Diffusion length of electrons in the base
L_em=sqrt(D_em*tau_em);   % Diffusion length of electrons in the base

%BASE SATURATION
CURRENT%%%%%%%%%%%%%%%%%%%%%%%%%%%%%%%%%%%%%%%%%%%

Num1=q*(D_ba/L_ba)*((ni*ni)/Na_ba)*((S_ba*L_ba) +tanh (x_ba/L_ba));
Den1=((S_ba*L_ba)/D_ba)*tanh (x_ba/L_ba)+1;
J0_ba=Num1/Den1;
```

```
 % EMMITER SATURATION CURRENT

Num2=q*(D_em/L_em)*((ni*ni)/Nd_em)*((S_em*L_em) + tanh (x_em/L_em));
Den2= ((S_em*L_em)/D_em)*tanh (x_em/L_em) +1;
J0_em=Num2/Den2;

 % DIFFUSION CURRENT CALCULATION
V=linspace (-1, 1, 1000);
 J_sat=J0_ba+J0_em;

J_dif= (J_sat*(exp (V/0.026)-1))*1000; % Diffusion current density in mA/cm^2
J_dif_positive=abs (J_dif);
Plot (V, J_dif_positive)
```

_____

APPENDIX B

Presentations and publications

Oral presentation, "Dilute nitride n-i-p-i solar cells" EMRS Spring conference, Strasbourg (2012)

Oral presentation, "Dilute nitride and GaAs n-i-p-i solar cells" ICSN International Conference, Dresden, (2012)

Oral presentation, "Comparative study of dark current density in various 1.0 eV sub-junction designs", UKsemiconductors, Sheffield, (2014)

Publications

S. Mazzucato, B. Royall, R. Ketlhwaafetse, N. Balkan, J. Salmi, M. Guina, A. Smith and R. Gwilliam, *"Dilute nitride and GaAs n-i-p-i solar cells",* Nanoscale research letters, **7**:631 (2012)

B. Royall, S. Mazzucato, R. Ketlhwaafetse, N. Balkan, J. Puustinen, M. Guina, and A. J. Smith, "GaAs n-i-p-i solar cells with ion implanted contacts", Physica Status Solidi C, 1-4 (2013)

R. M. Ketlhwaafetse and N. Balkan**, "**Recombination lifetimes in $Ga_{1-x}In_xN_yAs_{1-y}$ p-i-n solar cells", Submitted to JPV IEEE, 2014